

Textural and Compositional Variation of
Tuff Marker Beds at the Mount Isa and
George Fisher Deposits; Implications for
Origin and Mineralisation

Thesis submitted in accordance with the requirements of the University of
Adelaide for an Honours Degree in Geology/Geophysics

Gabrielle Redden
October 2018



THE UNIVERSITY
of ADELAIDE

TEXTURAL AND COMPOSITIONAL VARIATION OF TUFF MARKER BEDS AT THE MOUNT ISA AND GEORGE FISHER DEPOSITS; IMPLICATIONS FOR ORIGIN AND MINERALISATION

TUFF MARKER BEDS AT MICO & GFM

ABSTRACT

World-class resources of Cu, Pb and Zn are deposited at Mount Isa Mines and George Fisher Mine, North West Queensland, hosted within the Urquhart Shale unit (1655 Ma) of the Proterozoic Mount Isa Inlier. Numerous beds of tuffaceous metasediments are also intercalated within the carbonaceous units, and have been relied on for constraining sequence stratigraphy. Tuff Marker Beds (TMBs) are described as cherty beds with cross-fractures at high angle to bedding, and having a highly potassic composition (Croxford, 1964). They provide the only indication of proximal volcanism associated with sedimentation; a line of evidence used to support a syngenetic sedimentary exhalative model of ore formation. The origin of potassic enrichment has previously been interpreted to be related to the composition of the original detrital sediments (including possible ash-fall tephra) and an unconstrained hydrothermal or diagenetic component.

TMB samples for this study, collected from Mount Isa Copper Operations (MICO) and George Fisher Mine (GFM), indicate potassic enrichment is not confined to TMBs. Additionally, characteristic fining-upwards sequences were not observed, which is consistent with the interpretation that some of the potassic enrichment is a hydrothermal alteration product, formed either as part of the diagenesis or from later mineralisation-related fluid events. TMB mineralogical and geochemical compositions are closely related to base metal sulphide mineralisation with textural evidence of several episodes of fluid migration, including potassic enrichment. Results indicate that the K-feldspar rich beds identified at MICO are not genuine air-fall tuffs.

Textural investigations of mineralised TMBs support a post-sedimentation and deformation paragenesis of ore emplacement of the Urquhart Shale. Providing further evidence for an epigenetic Cu and Pb-Zn mode of ore formation at Mount Isa and George Fisher. It is proposed that TMBs record volcanogenic sedimentation and provide a record of potassic and mineralisation-related alteration events, but are unrelated to ore genesis.

KEYWORDS

Tuff maker beds, TMBs, potassic enrichment, hydrothermal, diagenetic, epigenetic

TABLE OF CONTENTS

List of Figures and Tables	3
1. Background Geology.....	6
1.1. Geological Setting of Mount Isa and George Fisher Deposits	6
1.3. Urquhart Shale	8
1.4. Tuff Marker Beds (TMBs)	9
1.5. Ore Genesis in relation to Potassic Enrichment	9
1.6. Sampling.....	11
1.7. Minalyzer CS - Geolytical Core Scanner	12
1.8. Hand Sample and Thin Section Analysis	13
1.9. SEM/MLA.....	13
1.10. LA-ICP-MS	14
1.11. Geochemical analysis using SEM software.....	14
2. Results	15
2.1. Sample MICO A649.....	15
2.1.1. Petrology (Optical and SEM/MLA)	15
2.1.2. Minalyze Data.....	17
2.1.3. Modal Mineralogy	18
2.2. Sample MICO A826.....	19
2.2.1. Petrology (Optical and SEM/MLA)	19
2.2.2. Minalyze Data.....	21
2.2.3. Modal Mineralogy	22
2.3. Sample MICO B175	23
2.3.1. Petrology (Optical and SEM/MLA)	23
2.3.2. Minalyze Data.....	25
2.3.3. Modal Mineralogy	26
2.4. George Fisher Mine Samples	27
2.4.1. Petrology (Optical and SEM/MLA)	27
2.4.2. Minalyze Data.....	29
2.4.3. Modal Mineralogy	31
2.5. U-Pb Geochronology.....	32
2.5.1. Zircons	32
2.5.2. Monazites.....	34
2.6. Geochemical Comparative Analysis	37
3. Discussion	39

3.1. Comparison to Previous Work	39
3.1.1. Origin of Potassium Enrichment.....	39
3.1.2. Zircons	40
3.2. Classification Framework.....	42
3.2.1. Petrology (Optical and SEM/MLA)	42
3.2.2. Minalyze Data.....	43
3.2.3. Monazite Geochronology	44
3.2.4. Geochemistry	45
3.2.5. Implications for Ore Genesis	45
3.2.6. Economic Significance	46
4. Conclusions	47
5. Reccommendations for Further Study.....	48
6. Acknowledgements	49
7. References	50
Appendix A: Instrument Parameters	53
Appendix B: Optical and SEM/MLA Petrology Composite Images	54
Appendix C: Minalyze Data.....	65
Appendix D: Hand Sample Petrology	76
Appendix E: Thin Section Petrology.....	83

LIST OF FIGURES AND TABLES

Figure 1. Location of Mount Isa and George Fisher Mine.....	7
Figure 2. Drill core samples of TMBs.....	10
Figure 3. Mount Isa Mines model depicting location samples.....	11
Figure 4. George Fisher Mine model depicting location samples.....	12
Figure 5. Sample A649-2 optical petrology and SEM/MLA results.....	16
Figure 6. Minalyze data of oxides and zirconium for sample A649.....	17
Figure 7. Sample A826 optical petrology and SEM/MLA results.....	20
Figure 8. Minalyze data of oxides and zirconium of sample A826.....	21
Figure 9. Sample B175-D optical petrology and SEM/MLA results.....	24
Figure 10. Minalyze data of oxides and zirconium of core sample B175.....	25
Figure 11. Sample GFM-13 optical petrology and SEM/MLA results.....	28
Figure 12. Minalyze data of oxides and zirconium of GFM core samples.....	30
Figure 13. SEM images of zircons from GFM samples and MICO samples.....	33
Figure 14. Monazite Geochronology.....	35
Figure 15. Backscattered SEM image of monazites in sample GFM-0.29.....	36
Figure 16. Discrimination plots of geochemical data from MICO and GFM samples..	38
Figure 17. Comparison of rutile textures.....	41
Table 1. Modal Mineralogy of sample A649.....	18
Table 2. Modal Mineralogy of sample A826.....	22
Table 3. Modal Mineralogy of samples B175.....	26
Table 4. Modal Mineralogy of GFM samples.....	31

INTRODUCTION

Mount Isa Mines, a world-class sediment-hosted Cu and Pb-Zn-Ag deposit, and George Fisher Mine, one of the world's largest Pb-Zn-Ag deposits are both hosted within the Urquhart Shale unit of the Proterozoic Mount Isa Inlier in northwest Queensland. The Urquhart Shale is the only ore-bearing member of the Mount Isa Group (Bennett, 1965; Mathias & Clark, 1975), and contains numerous thin beds of tuffaceous metasediments, intercalated with both mineralised and barren pyritic shale (Farquharson & Richards, 1975). These Tuffaceous Marker Beds (TMBs) have been widely used as chronostratigraphic marker horizons (Bell, 1983; Neudert, 1984).

TMBs have been interpreted to have been hydrothermally altered to a potassic rich assemblage (Croxford, 1964). However, the nature and origin of potassic enrichment remains unconstrained. Croxford (1964), was the first to describe these layers as felsic pyroclastics, based on textures interpreted to represent volcanic glass shards. These shard textures were accentuated by petrographically observed rutile crystals along grain boundaries of the dominantly fine-grained K-feldspar groundmass.

There are several possibilities for the source of potassium enrichment, all of which have influenced theories of ore formation at Mount Isa and George Fisher. TMBs provide the only evidence of proximal volcanism associated with sedimentation, an argument that has been used to support a syngenetic, volcanic-exhalative (SEDEX) mode of ore formation (Croxford, 1964; Mathias & Clark, 1975; Stanton, 1962, 1963). Perkins (1997) supported a hydrothermal origin of TMB potassic enrichment as part of an alteration halo associated with the hydrothermal emplacement of epigenetic mineralisation. This theory is supported by other studies of the Mount Isa ore system (Gregory, Wilde, Schaefer, & Keays, 2005; Grondijs & Schouten, 1937; Lilly, 2017;

Perkins, 1984) whom interpret the origin of the deposit as hydrothermal replacement and brecciation in a zoned epigenetic Cu-Pb and Zn system.

However, Croxford (1964) favoured the interpretation that volcanic debris was water-lain, and inherited its potassium rich composition from connate water circulating during a relatively low temperature diagenesis. The observation that potassium was not exclusive to the TMBs and that other layers were also composed of potash-enriched material was used to substantiate the interpretation that connate water was responsible for potassic enrichment throughout the mineralised stratigraphic sequence.

Following Croxford (1964), it became core-logging standard at Mount Isa Mines, to stain suspected TMBs (STMBs) with hydrofluoric acid (HF), with the intensity of the resulting yellow stain indicating the relative proportion of potassium present. Cherty layers that stained strongly, contained obvious cross-fractures at a high angle to bedding and which terminated sharply at the layer boundaries, were logged as TMBs in the mine records. Advances in technology have created the opportunity to re-evaluate the historical petrographic observations of Croxford (1964), the continued relevance of current practices, as well as the opportunity to use new technology to provide new insight into the origin and the nature of the TMBs and their potassic enrichment.

Analysis of TMBs collected from Mount Isa Mines Copper Operation (MICO) and George Fisher mine (GFM) will be presented in this thesis using optical and SEM petrography and Mineral Liberation Analysis (MLA), Minalyze (XRF) data, Laser Ablation ICP-MS dating and geochemical bulk-rock approximation using SEM/MLA software. This thesis attempts to answer the following hypotheses:

- 1) Are 'tuff marker beds' actually tuff marker beds?
- 2) Potassium enrichment is not confined to tuff marker beds.
- 3) The origin of potassium enrichment is dominantly hydrothermal.

1. BACKGROUND GEOLOGY

1.1. Geological Setting of Mount Isa and George Fisher Deposits

The Mount Isa Inlier is considered to be the result of several phases of intracontinental rifting developed through the Paleoproterozoic to Mesoproterozoic (Bell, Perkins, & Swager, 1988). Mount Isa and George Fisher ore bodies are located in the Western Fold Belt (WFB) of the intracontinental basin. The basin experienced several major tectonic events, including the Barramundi Orogeny which terminated sedimentation, deformed and metamorphosed the WFB basement rocks (1900 – 1870 Ma) (Blake, 1987; Ethridge & Wall, 1994; Page & Williams, 1988; Scott et al., 2000).

Sedimentation recommenced in the WFB ca. 1870 – 1625Ma, and led to the deposition of the Mount Isa Group; a succession of carbonaceous siltstones and shales, which host all economic mineralisation. Sedimentation terminated in response to the Isan Orogeny ca. 1600 Ma (Betts et al., 2006) and was deformed in a series of compressional events (D1 –D4). The Paroo Fault; D1 (1610 ± 13 Ma), is the contact between the basement rocks of the Eastern Creek Volcanics, and the overlying mineralised Urquhart Shale (Figure 1, inset). The fault has subsequently been overprinted by D2 (1544±12Ma) and D3 (1510±13Ma) regional folding, which is responsible for the sigmoidal basement contact (Figure 1, inset). D3 is also associated with ‘silica-dolomite’ alteration and brecciation, both closely related with copper mineralisation (Mathias & Clark, 1975). D4 is considered to have produced the Buck Quartz Fault (BQF), a major low-angle structure present within the MICO operations (Bell et al., 1988; Gessner, Jones, Wilde, & Kuhn, 2006; Miller, 2007)

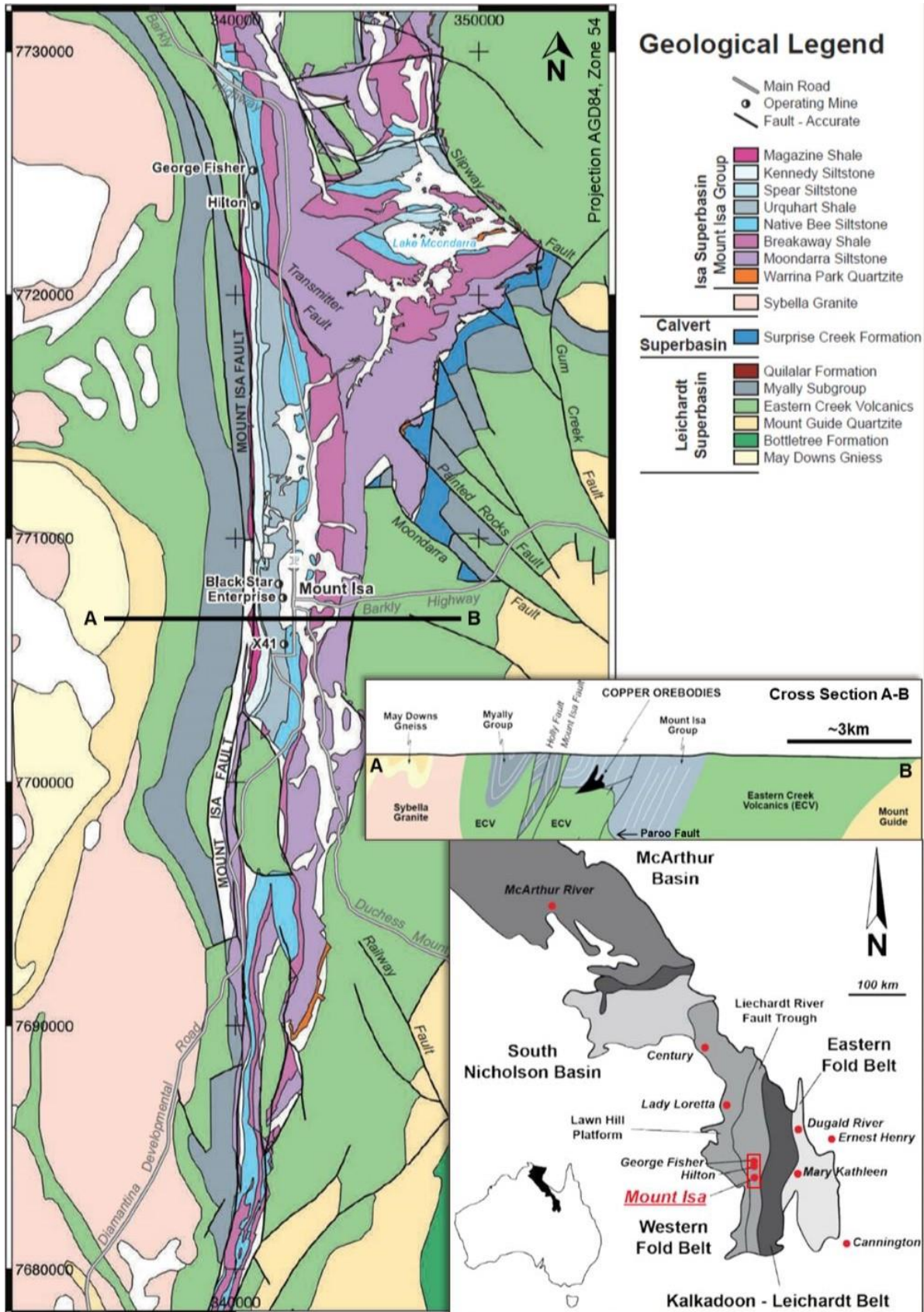


Figure 1. Location of Mount Isa and George Fisher Mine in relation to Australia and the Mount Isa Inlier. Regional geology of the Leichardt River Fault Trough, including the three main basin super sequences; Leichardt Superbasin, Calvert Superbasin and the Isa Superbasin (including the Mount Isa Group). Cross-sectional view of Mount Isa Mines showing the sigmoidal basin faulted contact where Cu orebodies are adjacent. After Betts et al., (2006) and Lilly (2017).

1.2. The Mount Isa Group

The Mount Isa Group is divided into the Lower Mount Isa Subgroup; Moondarra Siltstone and Breakaway Shale, and the Upper Mount Isa Subgroup; Native Bee Siltstone, Urquhart Shale, Spear Siltstone, Kennedy Siltstone and Magazine Shale. The Lower Subgroup consists of dolomitic and siliceous pyritic siltstones and shales, with some minor dolomite and quartzite, while the upper subgroup is more tuffaceous with dolomitic siltstones and shales (Mathias & Clark, 1975).

1.3. Urquhart Shale

All economic Cu and Pb-Zn-Ag mineralisation of the Mount Isa Group occurs within the 850-1050m thick Urquhart Shale unit (Bennett, 1965; Painter, 2003). The unit is dominated by mudstones and thinly-laminated carbonaceous, pyritic siltstones and alternating dolomitic siltstone and mudstone dipping 55° and 75° west (Perkins, 1984). SHRIMP U-Pb dating of 'ash-fall' zircons within TMBs has constrained of deposition of the Urquhart Shale at Mount Isa to be 1652±7 Ma and at George Fisher, 1655±4 Ma (Page, Jackson, & Krassay, 2000; Page & Sweet, 1998).

Early sedimentary studies on the fine grained and carbonaceous Urquhart Shale proposed a deep water setting (Mathias & Clark, 1975). Later, Neudert (1983), suggested the Urquhart Shale to have been formed in the slope to basin facies of a hypersaline and semi-emergent laustrine basin setting based on the presence of nodular carbonates, halite casts and stromatolites. However, most recently, Domagala, Southgate, McConachie, & Pidgeon (2000) proposed the Urquhart Shale to be the result of turbidite and/or tempestite sedimentation related to a deep-water submarine fan.

Silica-dolomite alteration is present as a halo extending away from the Paroo Fault. Copper mineralisation is generally adjacent or directly above the Paroo fault (Figure 1, inset), where

TMBs have been obliterated by brecciation (Bell et al., 1988; McLellan, O'Sullivan, Miller, & Taylor, 2014). At shallower levels, silica-dolomite occurs as projecting lobes and layer-replacement interfingering, but not overprinting, stratabound Pb-Zn orebodies (Perkins, 1984).

1.4. Tuff Marker Beds (TMBs)

Sixty TMBs were identified in the Mount Isa Mines stratigraphy by Croxford (1964) and described as 'grey, hard, brittle and cherty'. TMBs average thickness of 2.5– 6.5cm; however, significant variation from 1mm to 1.4m have been recorded (Perkins, 1997). The groundmass has been identified as microcrystalline with a dominant potassic feldspar mineralogy (Perkins, 1997). Comparatively coarser-grained K-feldspar crystals at the base of the beds is evidence of fining-upwards sequences (Croxford, 1964). Croxford also recognised feldspars had inverted from low-temperature monoclinic orthoclase to intermediate-triclinic microcline. Other notable observations include; rhombus ferroan dolomite was a common matrix accessory, rutile crystals formed along particular grain boundaries of the K-feldspar groundmass, and the composition of vein-fill of the cross-fractures varies in composition from dolomite to quartz, and included sphalerite, galena, chalcopyrite and pyrrhotite in mineralised areas. TMB samples used in this study were collected from MICO and GFM, locations can be seen in Figure 2.

1.5. Ore Genesis in relation to Potassic Enrichment

The interpretations of Croxford (1964) largely reflect the popular syngenetic, sedimentary-exhalative ore genesis theory of the time. Neudert (1983, 1984) largely ruled out exhalative processes because of the depositional environment of the Urquhart Shale was interpreted to be too shallow to reach temperature constraints of boiling. Additionally, Neudert (1984)

identified detrital K-feldspar in the TMBs, indicating the origin of potassium enrichment was from evaporitic brines altering a pre-existing sediment. He advocated for a hydrothermal origin of alteration, where fluids introduced from shallow basin margin faults altered the first few centimetres of sediment during initial deposition to late diagenesis.

Perkins (1997) suggested that while TMBs within the mine workings are relatively consistent, their highly potassic composition is largely confined to a potassic alteration halo (silica-dolomite), and that this characteristic feature is lost within three kilometres of the mine. Perkins (1997) also proposed TMB's represented an early stage of hydrothermal alteration, zoned around the deformed Paroo Fault contact. These observations led to his theory of epigenetic Pb-Zn and Cu formation, occurring co-genetically during the same event. This theory has since been supported by Taylor & Lilly (2016) and is the subject of ongoing research. Textural investigations in this thesis aim to understand the paragenesis of ore formation at MICO and GFM.

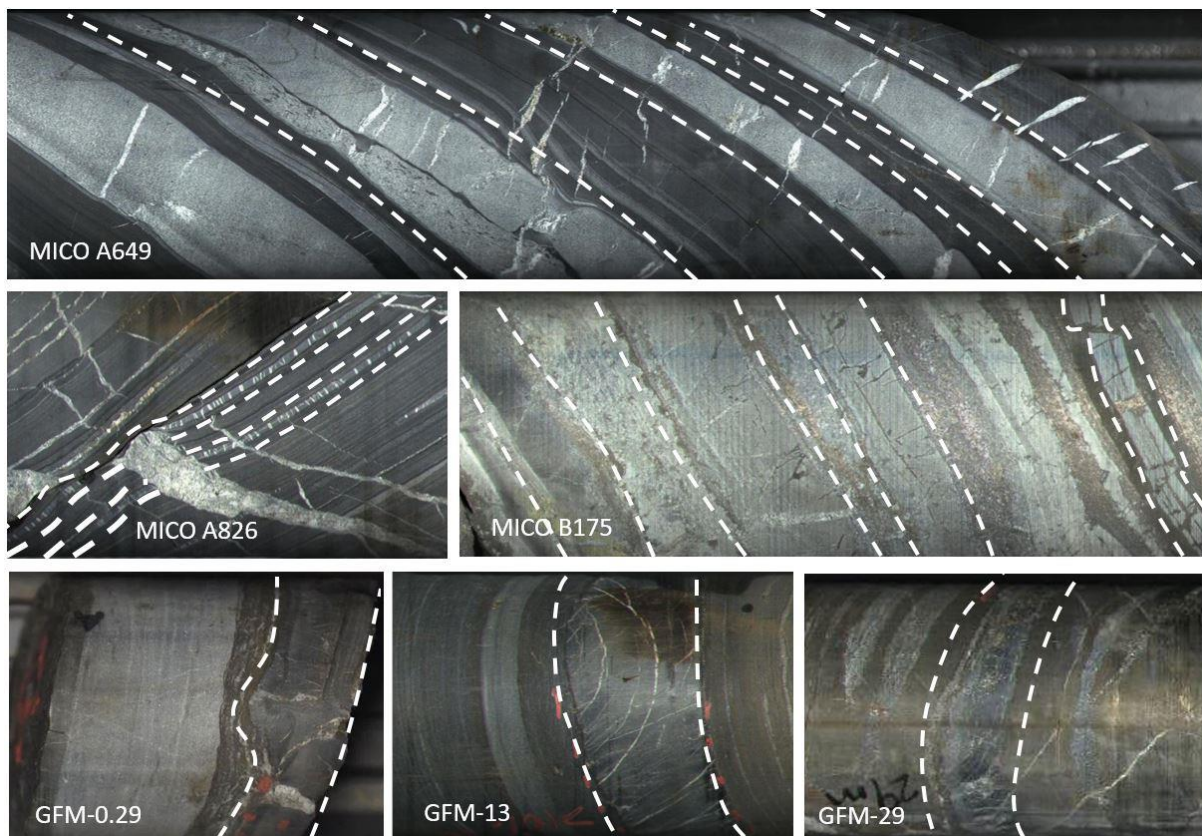


Figure 2. Drill core samples collected from Mount Isa Mines (MICO) and George Fisher Mine (GFM) that were logged as TMBs, showing cherty layers with cross-fracture veins at high angle to bedding which terminate sharply at the boundaries of cherty layers.

METHODS

1.6. Sampling

Sampling at Mount Isa Copper Operations and George Fisher Mine was conducted in January-February 2018 in conjunction with a vacation placement. The relevance of TMBs at MICO has declined since the end of Pb-Zn mining in 2016, as TMBs have been highly disturbed within the brecciated Cu ore system. Samples for this study were collected from surface drilled exploration holes, where STMBs had been identified by textural qualifiers and then HF stained. Nine STMBs were identified in three sections of core samples; A649, A826 and B175 from drill-holes 201211302, and 201208122 and have been analysed in this thesis (Figure 3). Three STMBs were collected from GFM drill-hole 14C_H730_02; GFM-0.29, GFM-13 and GFM-29 (Figure 4). Preliminary analysis on additional samples and can be found in Appendix B, C, D and E.

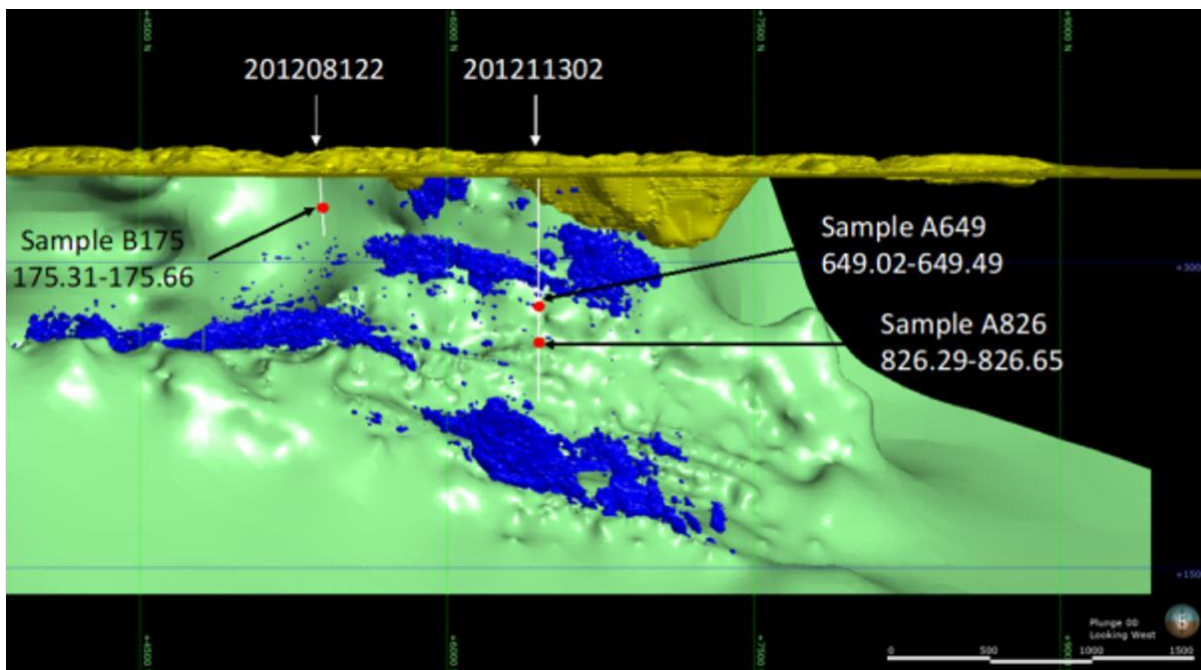


Figure 3. Model of Mount Isa Mines, showing the 3% Copper grade cut-off as blue shells, current surface and extent of the Black Star open pit in yellow and the location of drill-holes which sourced TMB samples for this thesis. Image courtesy of S. O'Brien, Mount Isa Mines.

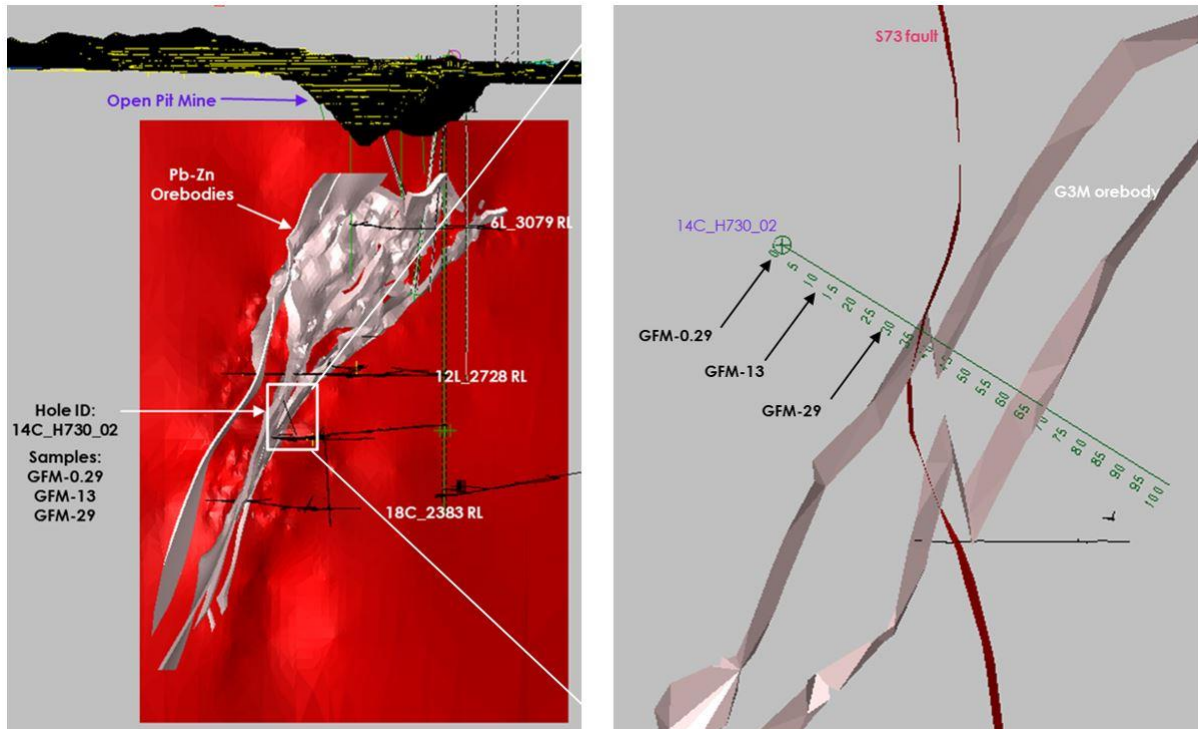


Figure 4. George Fisher Mine model depicting location of drillhole and sample selections with respect to Pb-Zn orebodies (pink surfaces) and faults (red surface, right-hand image). Image courtesy of V. Wai, George Fisher Mines.

1.7. Minalyzer CS - Geolytical Core Scanner

The Minalyzer is a new-to-market commercial drill core scanner that produces geochemical XRF analysis, high resolution photography, structural measurements and specific gravity estimation. Analysis was conducted using an Ag X-ray tube at 30 kV and 24mA, scanned at 1mm/second. Other information regarding signal processing and associated algorithms can be found in Sjoqvist et al. (2015) and Appendix A. The ability of the instrument to continually scan and provide assay-quality XRF data on designated intervals (down to 1cm) provides a step-change from traditional 1m or 2m wet-chemistry composite samples. Minalyzer instruments were used at GFM and the Tonsely Core Library, Adelaide. For this project a continual strip of XRF data along the centre of each drill core sample was selected. This data is used to visually illustrate the elemental variation of TMBs and surrounding units alongside high resolution core photos. The major oxides including K_2O , TiO_2 , SiO_2 and CaO data were the focus of geochemical variation analysis in this thesis because their variation is considered

the most appropriate for comparison for this rock type. Zirconium (Zr) was also included in the analysis to determine whether it can be a reliable proxy for identifying TMBs. This is the first use of Malyzer data in an Australian honours research project.

1.8. Hand Sample and Thin Section Analysis

Initially, visual observations of the STMBs in hand sample (core) were recorded to establish a framework of detailed descriptions and to assess the variation between samples. Close examination of hand samples aided in selecting thin sections that best represent the STMB and immediate geological relationships. Thin sections were made by Ingham Petrographics, Qld. Optical and Reflected light Microscopy was performed using the Olympus BX51 microscope, Olympus TH4-200 light source and Olympus DP21 Camera.

1.9. SEM/MLA

Petrographic analysis of the textures and mineralogy of TMBs was completed using backscattered electron (BSE) detector in a FEI Quanta 600 MLA scanning electron microscope (SEM). Instrument specifications can be found in Appendix A. Electron dispersive x-ray spectrometer (EDS) identified minerals within the sample of the BSE detector, and by mineral liberation analysis (MLA) mapping. The BSE response of copper was used as a standard to define the searchable grey scale range for MLA mapping. Mapping regions of the thin section were set and X-ray spot analysis was taken wherever a mineral occurred, and each mineral was matched to a list of collected x-ray spectra and assigned a colour for the MLA maps. Mineralogical maps helped distinguish mineral relationships at a macro-scale within the very fine groundmass of the samples. MLA was also utilised to identify monazite and zircon grains for geochronology using LA-ICP-MS.

1.10. LA-ICP-MS

U-Pb isotopes in monazites were analysed at Adelaide Microscopy, University of Adelaide, with an ASI resolution 193nm ArF excimer laser ablation system with a S155 large format sample chamber, coupled to an Agilent 7900x ICP-MS. Further instrument specification can be found in Appendix A. The raw data was processed using Iotlite and Isoplot R. Because of the small grain size of both monazites and zircons, the signals were reduced to remove signal from surrounding mineralogy. The datasets were further reduced to obtain best fit for geochronology using Isoplot R.

1.11. Geochemical analysis using SEM software

MLA maps were used to calculate the major element geochemistry of the STMB layers. Representative sections of the full width of sample groundmass with least contamination of veins and hydrothermal mineralogy were selected. Sample areas of shale were also included to assess whether the STMBs varied significantly from the shale lithology. The chemistry of minerals was determined using non-standardised EDS analysis of minerals. The abundance of minerals in the TMB layers was obtained using MLA Dataview software. These two data sets were combined to generate a representative whole rock geochemistry data set for the MICO and GFM samples. The use of EDS for mineral compositions means that the calculated whole rock geochemistry is approximate, which is considered to be fit for purpose given the inherent mineralogical heterogeneity of shale layers. Data was compared between MICO and GFM STMBs with shale units, Croxford's (1964) original data and published geochemistry datasets of modern TMBs; China 1 (Du, Wang, Wang, Deng, & Yang, 2015), China 2 (Zou, Tian, & Tian, 2016), New Zealand (Briggs et al., 2010) and India (Saha & Tripathy, 2012).

2. RESULTS

2.1. Sample MICO A649

2.1.1. PETROLOGY (OPTICAL AND SEM/MLA)

The three STMBs identified in core sample A649 are light grey in colour with white carbonate-filled veins (<3mm) that cross-cut the bed and terminate at the layer boundaries which are defined by sharp contacts with darker sedimentary layers (Figure 5a). Grain size is too fine to visually identify mineralogy in hand sample but was confirmed to be dolomite under microscope and SEM/MLA (Figure 5e). The cross-fractures that terminate at the layer boundaries are composed of calcite, dolomite, and some minor infill of coarse-grained pyrite, also termed Pyrite-2 (Figure 5) (Connell, 2016; Maguire, 2016). Other accessory minerals include K-feldspar and quartz dispersed heterogeneously throughout the layer, intergrown with the dolomite. The layers adjacent to the STMB are composed of very fine-grained K-feldspar, muscovite, quartz and fine-grained pyrite; also termed Pyrite-1, which formed as the result of a pre-ore hydrothermal activity (Maguire, 2016 and Connell, 2016). One subhedral, detrital, zircon grain of ~80µm diameter (Appendix B) was identified within the shale layer adjacent to STMB A649-3, however, no zircons were identified within the STMBs. The dolomite rich layers are interpreted to be selective bedding replacement by dolomite of original carbonaceous shale (silica-dolomite alteration) (Perkins, 1984). Undeformed hydrothermal minerals overprinting the dolomite include; K-feldspar, calcite, quartz, fluorite, biotite, chlorite, albite, apatite and rutile (Figure 5). Undeformed coarse-grained Pyrite-2 and galena, are also present as infill and veins (Figure 5), indicating they are post deposition, and of hydrothermal origin. Detailed petrographic notes of all A649 samples are located in Appendix B, C and D.

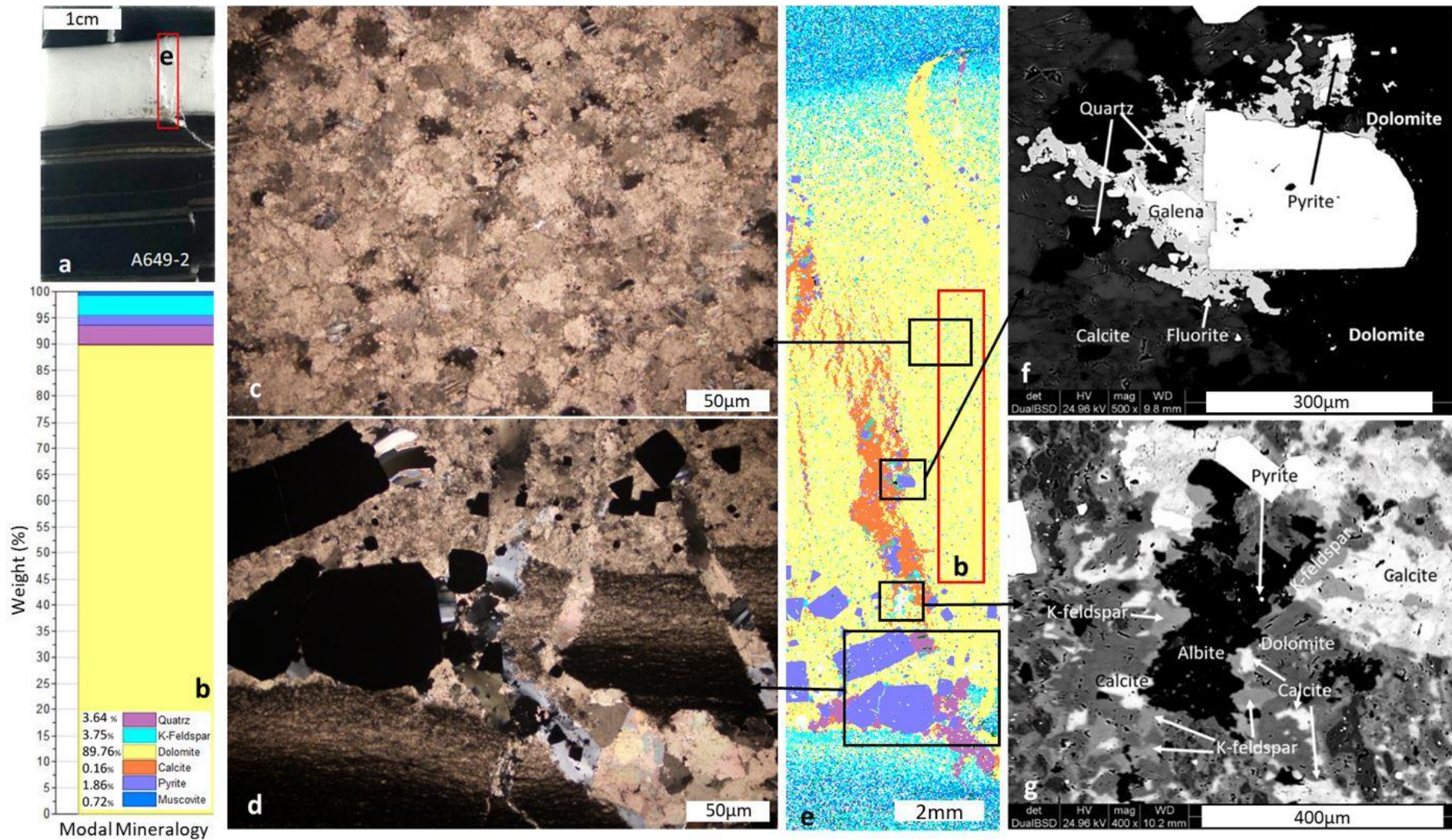


Figure 5. Sample A649-2 optical petrology and SEM/MLA results.

5a) Thin-section A649-2 light coloured layers is a STMB, the red box indicates the area mapped by MLA (Figure 5e). (5b) Modal mineralogy plot obtained from the red box indicated on the MLA map (e), which serves as a semi- quantitative composition of the STMB groundmass. (5c) Dolomite dominated groundmass, within the ‘TMB’ layer with minor dark specks of k-feldspar incorporated (PPL). (5d) The base of the TMB layer is offset/faulted and a vein network is infilled with quartz, calcite and k-feldspar and mineralisation of coarse-grained Pyrite-2 (PPL). (5e) MLA map of area indicated in Figure 5a, it shows the dominantly dolomitic (yellow) groundmass of the STMB with overprinting k-feldspar, quartz and coarse-grained Pyrite-2. The dolomitic composition transitions to fine intergrowths of k-feldspar, muscovite and quartz either side of the layer. Vein minerals include calcite, quartz, fluorite, biotite, albite, K-feldspar, coarse-grained Pyrite-2 and galena. (5f) Dolomite groundmass overprinted by calcite vein cross-cutting and offsetting the dolomite bed. Vein infill includes largely calcite, with quartz, followed by infill of coarse-grained Pyrite-2, then galena and lastly fluorite showing infill textures around aforementioned minerals. (5g) Dolomite groundmass overprinted by vein infill of calcite, with coarser grained K-feldspar (compared to groundmass) with precipitation of coarse-grained Pyrite-2 and later stage infill of albite.

2.1.2. MINALYZE DATA

One centimetre split Minalyze XRF data of core sample A649 shows positive correlation between oxides K_2O , SiO_2 , TiO_2 and Zr, and a negative correlation with CaO . Peak values of K_2O , SiO_2 , TiO_2 and Zr correlate reasonably with the layers identified as STMBs. However, not all peaks are associated or confined to STMBs, and large variation in elements and oxides are present along the length of the core sample. The highest K_2O value of 11.59% occurs within the interval 649.03 – 649.04, and is at the top of the core sample and not associated with any STMB layers. The lowest value 0.58% K_2O is between 649.33 – 649.34 which occurs directly above a STMB layer (A649-2). Raw data found in Appendix C.

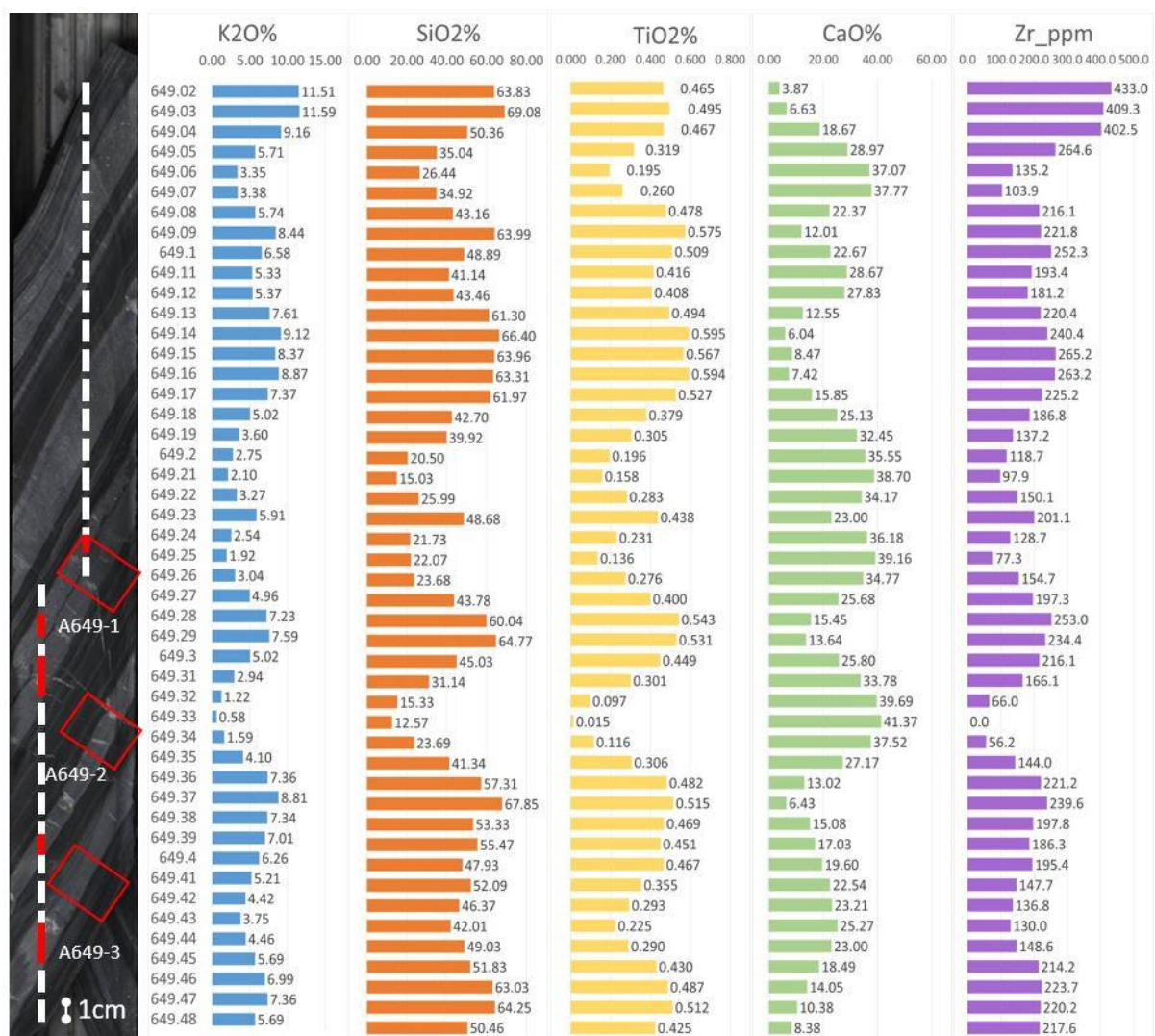


Figure 6. Minalyze data of oxides and zirconium for sample A649. The scanned path of the Minalyzer is indicated by the white dotted line over the core sample, thin-sections are indicated by the red boxes.

2.1.3. MODAL MINERALOGY

The modal mineralogy of STMBs was obtained by areas selected on MLA maps (Figure 5b). These results provide a qualitative to semi-quantitative method of characterising the groundmass mineralogy of the STMBs. All three STMBs from core sample A649, were dominated by dolomite with a characteristic modal mineralogy of carbonaceous (dolomitic) composition (Table 1).

Minerals	Abundance (wt%)
<i>Apatite</i>	0.03
<i>Dolomite</i>	85.11
<i>Galena</i>	0.02
<i>Fluorite</i>	0.14
<i>Calcite</i>	1.97
<i>Quartz</i>	2.45
<i>Biotite</i>	0.08
<i>Pyrite</i>	3.34
<i>K-Feldspar</i>	5.89
<i>Chlorite</i>	0.01
<i>Muscovite</i>	0.95

Table 1. Modal Mineralogy of sample A649, showing dominant Dolomitic composition.

2.2. Sample MICO A826

2.2.1. PETROLOGY (OPTICAL AND SEM/MLA)

The cross-fractures are a distinctive feature of this sample, in both hand sample and thin section (Figure 7). Two 2mm STMB layers are captured within the same thin section, separated by 9mm of external fine-grained dark groundmass and layers of fine grained Pyrite-1. Both STMBs are composed of fine-grained K-feldspar (~10 μ m). Both STMB layers have no visible difference in K-feldspar grain size (e.g. no fining –upwards sequences). Cross-fractures display several stages of fluid ingression, where infill of calcite has been injected with later-stage dolomite and quartz (Figure 7e and Appendix B). These cross-fractures terminate sharply at the lower and upper boundaries, with no indication of infill origin/migration pathway. The adjacent layers are composed of fine-grained Pyrite-1 bands and mixture of K-feldspar, quartz and dolomite. Quartz and dolomite are accessory minerals within the K-feldspar dominated layer. Subhedral (hydrothermal) rutile (<30 μ m) is a common accessory throughout the shale and found intergrown within the fine-grained Pyrite-1 layers and as inclusions within the dolomitic intrusion. Full petrographic analysis of A826 samples are located in Appendix B, C and D.

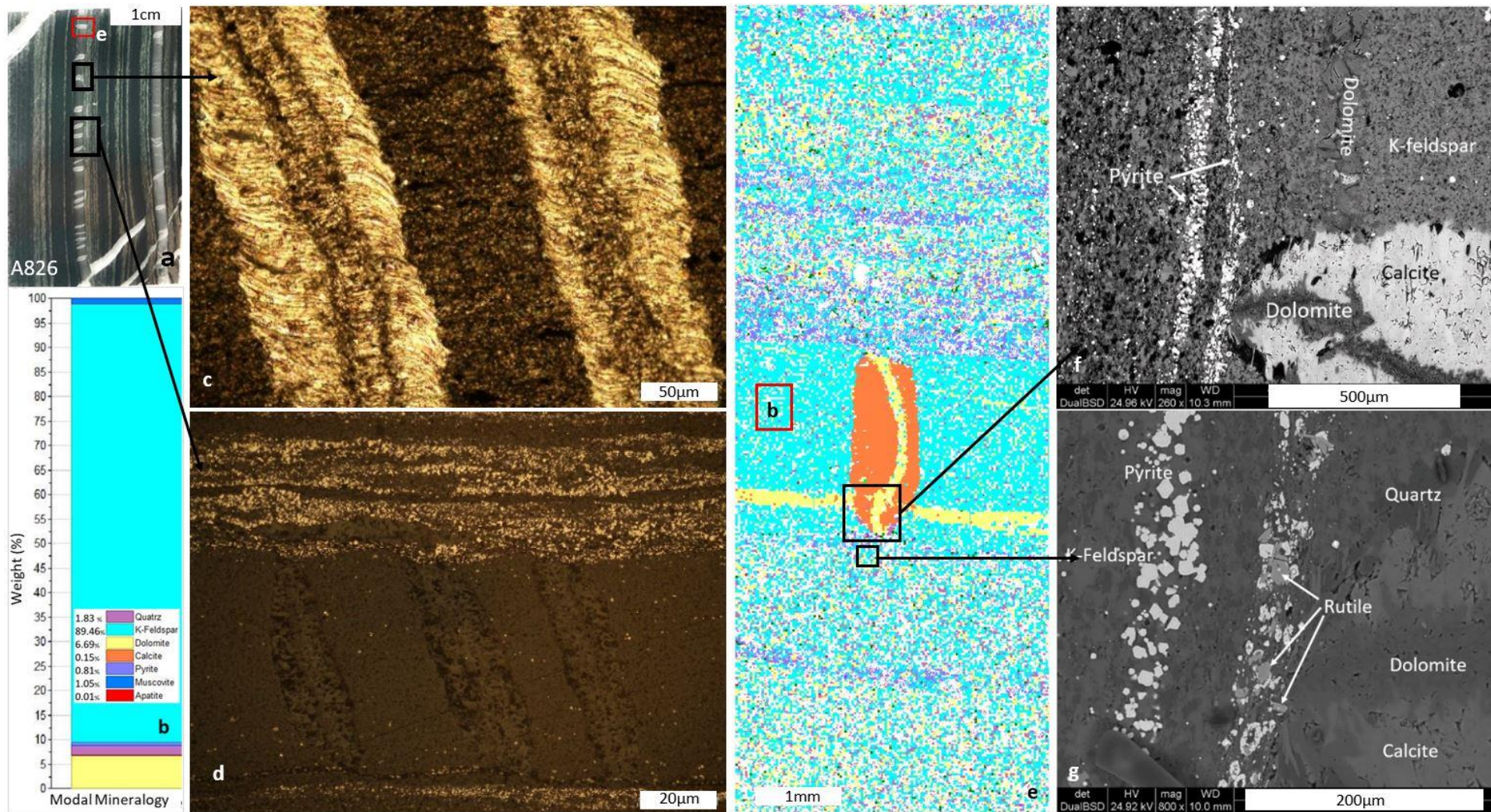


Figure 7. Sample A826 optical petrology and SEM/MLA results.

(7a) Thin section A826 captures two suspected TMBs within 1.5cm. Both have very small veins that appear to be ‘cross-fractures’ that terminate at the boundaries of the TMB. The red box indicates the area mapped by MLA (Figure 7e). (7b) Modal mineralogy plot obtained from the red box indicated on the MLA map (Figure 7e), which indicates groundmass is dominantly K-feldspar rich with accessory dolomite, quartz, muscovite and scatterings of Pyrite-1 and a trace amount of apatite grains. (7c) Vein/cross-fracture infill of calcite, which appears to bulge within the middle of the bed and has a distinctive vein of dolomite cross-cutting through the middle. Calcite grains appear to fan outwards with a folded, deformed pattern (XPL). (7d) The cross-fractures terminate at the lower and upper boundaries of the STMB, which are somewhat marked by Pyrite-1 mineralised bands (reflected light image). (7e) The STMB is k-feldspar enriched (blue), the lower boundary of the TMB appears to terminate with the first appearance of fine-grained Pyrite-1. The horizontal dolomite vein is overprinted by the calcite vein transecting the STMB, which has then itself been cross-cut by later stage dolomite vein which bears minor accessory coarser-grained K-feldspar. This paragenesis indicates several stages of dolomite dominated hydrothermal activity. (7f) The base of the calcite vein with the late stage dolomite stems off a fine-grained Pyrite-1 band, with no clear migration pathway for the resultant calcite and dolomite veins. (7g) Quartz is found to rim the calcite vein at the base, and is found speckled throughout the k-feldspar groundmass. Rutile is also found within the Pyrite-1 bands as small grains.

2.2.2. MINALYZE DATA

Sample A826 shows a general trending increase in oxides K_2O , SiO_2 and TiO_2 and slight decrease in CaO towards the two layers identified as STMBs in thin section sample A826 (Figure 6). This trend is more widespread, opposed to being a response to the presence of the STMBs, as the peaks of K_2O , SiO_2 and TiO_2 are not confined to the STMB layers. The CaO is also increased with respect to the scan tracks along the dolomitic vein in the top half of the core sample. The correlation between K_2O , TiO_2 , SiO_2 and Zr are positive, and negative between CaO . Zirconium has a correlation of 0.6405 to K_2O , and therefore follows a similar increasing trend around the two thin STMB layers. The highest K_2O peak 6.17% occurs

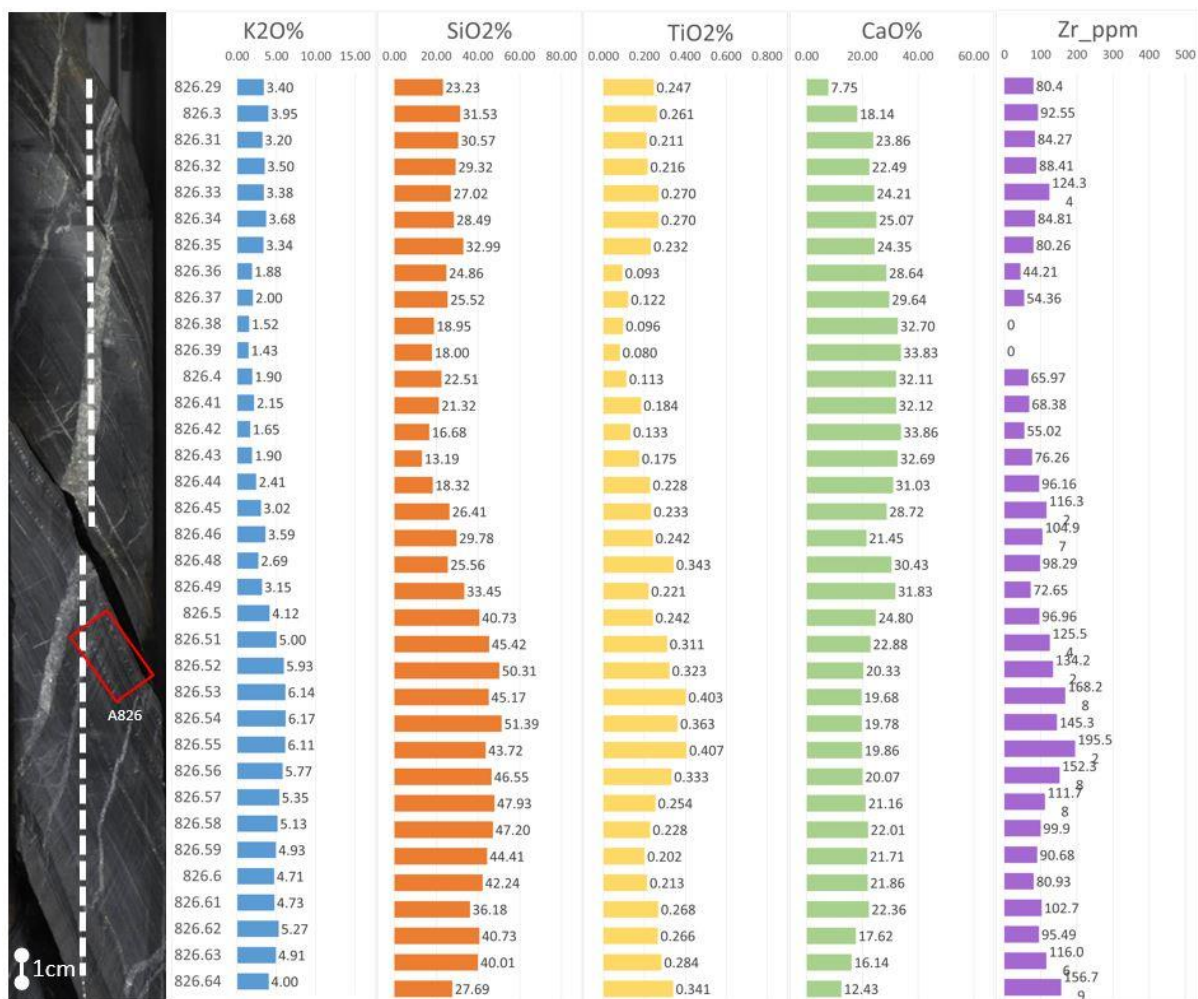


Figure 8. Minalyze data of oxides and zirconium of sample A826. The white dotted line shows the scanned path of the Minalyzer and the STMB thin-section area indicated by the red box.

between 826.54 – 826.55 which is 1cm below the lower STMB layer. The lowest K₂O value 1.43% occurs within the interval 826.39 – 826.40, which has scanned an area including a dolomitic vein. Minalyze data of sample A826 and correlation coefficients found in Appendix B. Raw data found in Appendix C.

2.2.3. MODAL MINERALOGY

Both STMBs in sample A826 are K-feldspar rich as seen from microscope petrology and SEM/MLA (Figure 7e), and have a very similar groundmass composition. However, a dolomitic vein was included in the sample area for the modal mineralogy of the second STMB in sample A826 (Appendix B), and was therefore omitted from the analysis. The characteristic modal mineralogy for A826 samples is strongly K-feldspar enriched (Table 2).

<i>Minerals</i>	<i>Abundance (wt%)</i>
<i>Apatite</i>	0.01
<i>Dolomite</i>	6.69
<i>Calcite</i>	0.15
<i>Quatrz</i>	1.83
<i>Pyrite</i>	0.81
<i>K-Feldspar</i>	89.46
<i>Muscovite</i>	1.05

Table 2. Modal Mineralogy of sample A826, showing K-feldspar enrichment.

2.3. Sample MICO B175

2.3.1. PETROLOGY (OPTICAL AND SEM/MLA)

The four thin sections/STMBs from sample B175, have three different compositional variations. Thin section B175-A (Figure 9) and B175-B both have a groundmass of K-feldspar with varying abundance of layer-controlled or disseminated biotite with quartz and K-feldspar. B175-C and B175-D, are K-feldspar dominant with relatively high quartz included in the groundmass. Chlorite is present as an overprinting alteration texture within a K-feldspar rich zone of B175-C. B175-D STMB was deformed in a brittle manner prior to the introduction of hydrothermal pyrrhotite, galena and coarse grained Pyrite-2, providing evidence that this layer was lithified before hydrothermal ore fluids were introduced (Figure 9). Two distinct K-feldspar textures were observed; coarse-grained fracture infill of potential hydrothermal origin and fine-grained K-feldspar in the STMB groundmass, potentially diagenetic in origin. An interesting textural relationship was observed within the fracture infill, involving galena infilling around fluorite, chlorite, quartz and K-feldspar, indicating that the galena is relatively late stage and undeformed (Figure 9g). Full petrographic analysis of all B175 samples are located in Appendix B, C and D.

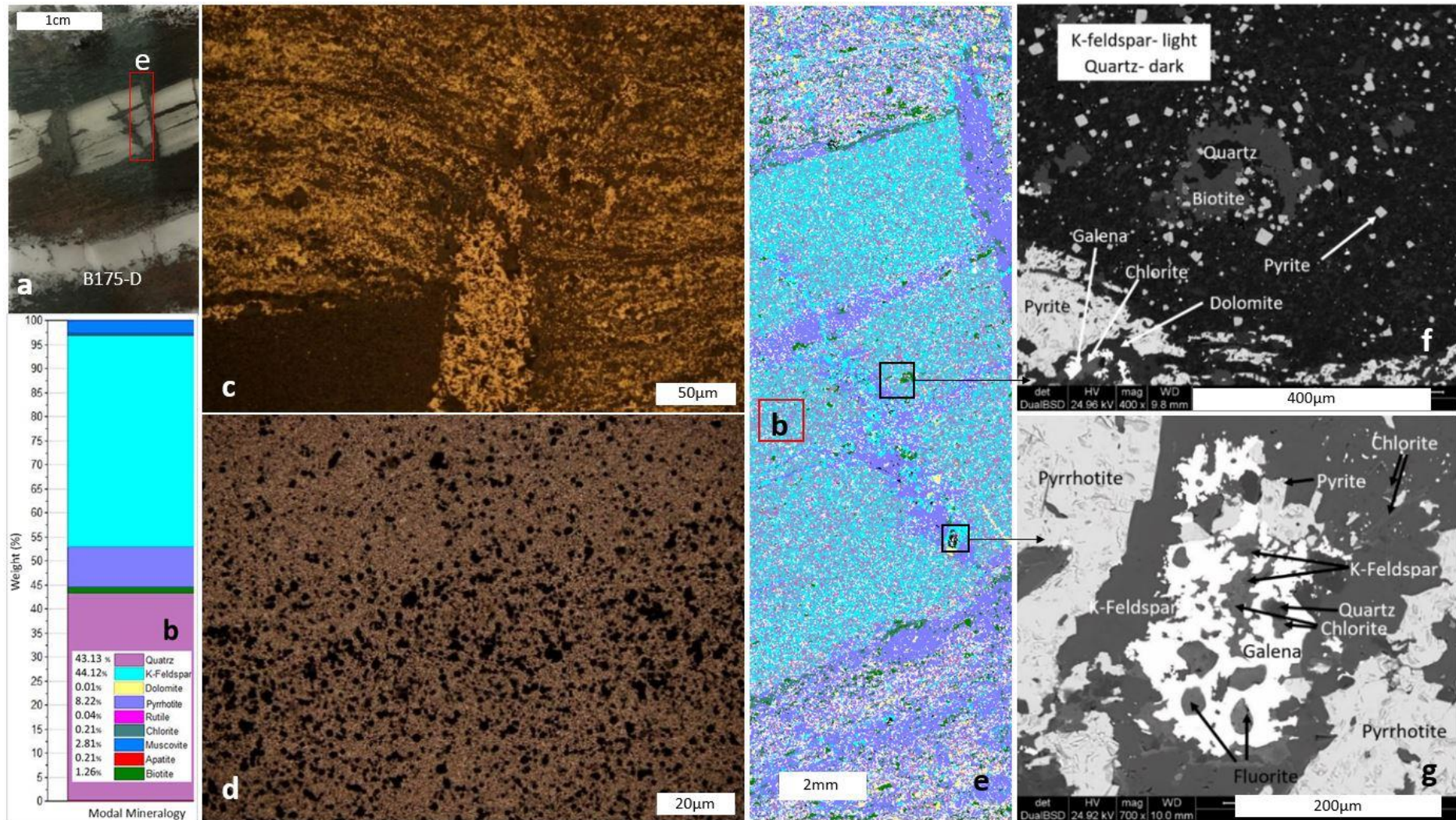


Figure 9. Sample B175-D optical petrology and SEM/MLA results.

(9a) Thin section B175-D Map 1 captures a portion of the faulted bed block of the suspected TMB. Pervasive pyrrhotite mineralisation, infilling faults and fractures of the STMB in addition to the surrounding layers. The red box indicates the area mapped by MLA (Figure 9e). (9b) Modal mineralogy plot obtained from the area indicated by the red box on the MLA map (Figure 9e), shows sample is dominated by both quartz and K-feldspar. (9c) Faulted bed infilled with pyrrhotite which comes to an end as the pyrrhotite flows out of the fault and into the layer above gives the appearance of the direction of fluid flow. (9d) Fine grained groundmass of K-feldspar with isotropic quartz and fine grains of pyrrhotite distributed throughout the STMB. (9e) MLA map of area indicated in figure 9a. The STMB is relatively enriched with K-feldspar and quartz. Post lithification faulting of the STMB has been infilled by pyrrhotite and so too have the horizontal fractures through the bed. Coarser-grained K-feldspar is seen as infill within the faults/veins. (9f) Fine grained groundmass of K-feldspar and quartz, with infill of pyrite-2, and coarse-grained biotite. Late stage galena and chlorite infill are also present. (9g) Pyrrhotite infilling fracture through STMB, and has inclusions of coarse-grained K-feldspar, quartz, chlorite and fluorite. Galena is seen to infill around these minerals.

2.3.2. MINALYZE DATA

Core sample B175 was scanned at 1cm resolution to observe the variation along the core and the four layers identified as STMBs (Figure 10). There is positive correlation between oxides K₂O, SiO₂ and TiO₂, and a negative correlation with CaO. B175-C and B175-D correlate to peaks in K₂O, SiO₂, and TiO₂, and decreased CaO. Increase in Zr concentration also somewhat correlates to these two STMBs, however, the increase is not sharply defined or confined to the STMB layers. The other two STMBs (B175-A and B175-B) do not correlate to any spikes in geochemistry, as the increase in K₂O, SiO₂, and TiO₂ begins between B175-B and B175-C. Zirconium is heterogeneously detected throughout the sample, and is identified with the interval of layer B175-A. Sample B175-B does not contain any Zr,



Figure 10. Minalyze data of oxides and zirconium of core sample B175. The white dotted line shows the scanned path of the Minalyzer and the thin-section area indicated by the red boxes.

however, several intervals at the top of the core sample have a considerable concentration of Zr. The highest K₂O value of 7.42% occurs within the interval 175.61 – 175.62 towards the bottom of the core sample and just within the area of the B175-D STMB. The lowest value 1.48% K₂O is between 175.42 – 175.43 which occurs in the top third of the core sample above thin section B175-A. Raw data found in Appendix C.

2.3.3. MODAL MINERALOGY

There are mineralogical differences between all four B175 samples, large variation in biotite and quartz abundance, whilst K-feldspar concentration remains relatively consistent across all samples (Table 3). The average modal mineralogy of K-feldspar for samples B175-A, B, C and D, is 42.09%. Biotite is higher than quartz in STMB B175-A (38.39% compared to 8.61%), whereas in samples B175-B and B175-C, biotite was lower than quartz. B175-B had 20.68% biotite and 33.47% quartz, and B175-C had 10.95% biotite and 29.56% quartz. B175-D also has biotite lower than quartz, but there is a greater disparity; biotite 1.26% and quartz 43.13%. These results quantify the variation between STMB samples, however, based on the K-feldspar composition, they are characterised as moderately K-feldspar enriched STMBs with variable quartz and biotite composition.

<i>Minerals</i>	<i>B175-A</i>	<i>B175-B</i>	<i>B175-C</i>	<i>B175-D</i>
<i>Apatite</i>	0.41	0.25	0.15	0.21
<i>Dolomite</i>	0.00	1.72	2.12	0.01
<i>Galena</i>	0.07	0.87	0.83	0.00
<i>Fluorite</i>	0.00	0.00	0.00	0.00
<i>Calcite</i>	0.00	0.00	0.00	0.00
<i>Quartz</i>	8.61	33.47	29.56	43.13
<i>Biotite</i>	38.39	20.68	10.95	1.26
<i>Pyrite</i>	0.18	0.12	0.64	8.22
<i>K-Feldspar</i>	40.33	38.79	45.11	44.12
<i>Rutile</i>	0.03	0.02	0.02	0.04
<i>Thorite</i>	0.00	0.00	0.00	0.00
<i>Zircon</i>	0.01	0.00	0.00	0.00
<i>Chlorite</i>	8.14	1.99	6.20	0.21
<i>Muscovite</i>	3.82	2.09	4.41	2.81

Table 3. Modal Mineralogy of samples B175, showing the variation between samples is result of quartz and biotite composition, while K-feldspar remains relatively constant.

2.4. George Fisher Mine Samples

2.4.1. PETROLOGY (OPTICAL AND SEM/MLA)

GFM samples are significantly different to MICO samples. The groundmass of all GFM samples is K-feldspar dominant, too fine-grained to identify individual grains, appearing as a solid band of K-feldspar. The STMBs include minor accessory quartz, rutile, apatite and variable carbonate mineralogy. Dolomite is identified within the groundmass, often as subhedral – euhedral rhombus crystals (Figure 11c). MLA maps display a striking contrast between the STMB groundmass and the surrounding lithologies, which is also reflected in the Minalyze data (Figure 12). Calcite and dolomite are dominant vein infill minerals, with minor pyrrhotite. All three STMBs have defined layer boundaries, most commonly contrasted by mineralisation of pyrrhotite or fine-grained pyrite. The groundmass of all three STMBs is relatively homogenous, with no obvious fining upwards sequences.

109 euhedral zircons have been identified in sample GFM-0.29, 71 in GFM-13 and 109 in GFM-29. Textural relationships with zircons show apatite as infill growing around zircon grains, however, rutile in one example does appear to have grown contemporaneously with the zircon grain (Figure 11g). Soft sediment deformation was observed in GFM-0.29 (Figure 15) where a deformed STMB has the appearance of a soft-sediment slump (Figure 15). Stylolite structures were also observed, and have been infilled with fine-grained Pyrite-1 (Figure 15). The weakness of the deformed bedding has been later exploited by a vein of silica-dolomite, with included anhedral hydrothermal monazite. All of these features were overprinted by later sulphide mineralisation (Figure 15). Full petrographic analysis of all GFM samples are located in Appendix B, C and D.

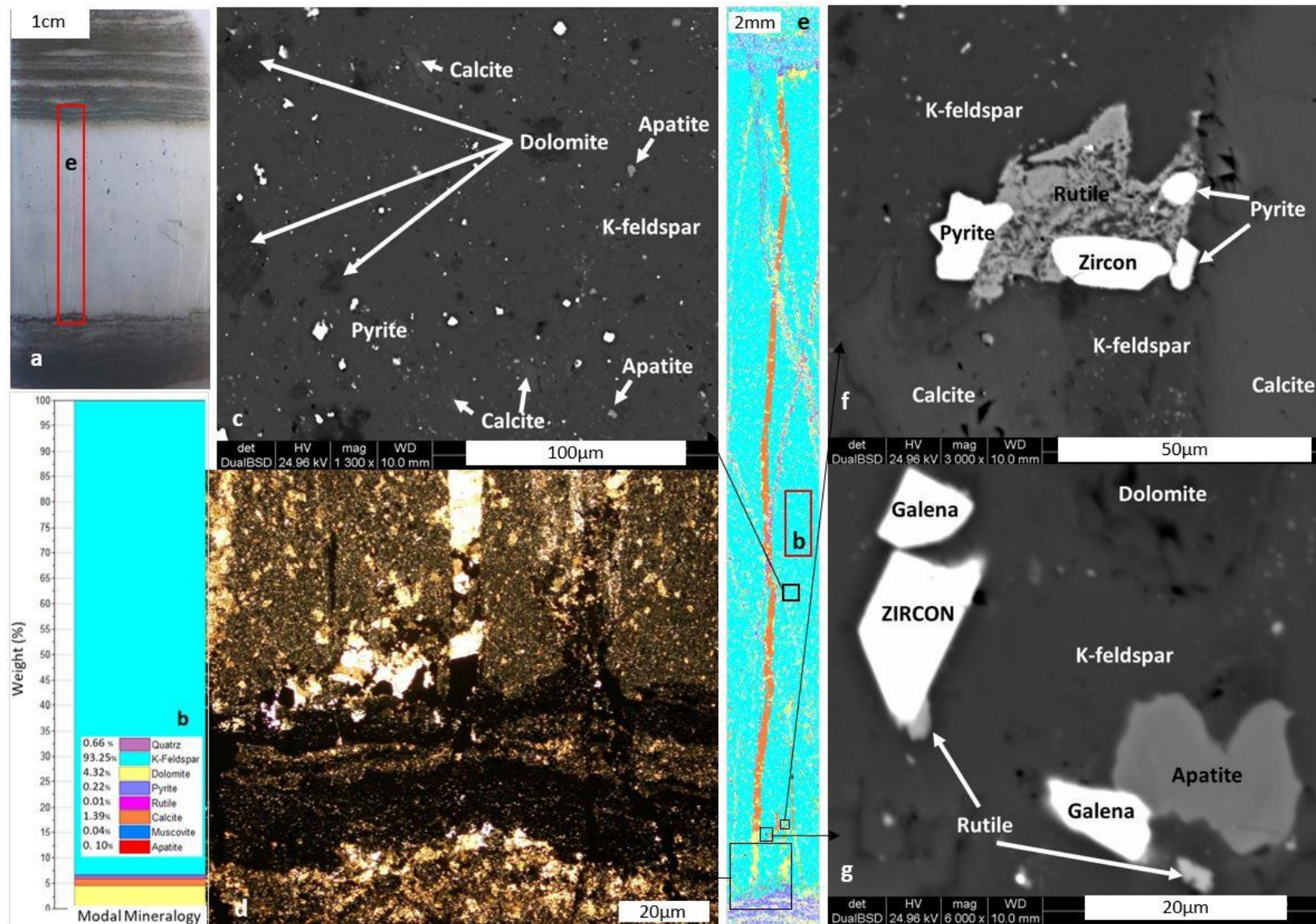


Figure 11. Sample GFM-13 optical petrology and SEM/MLA results. (11a) Thin section GFM-13 showing area mapped by MLA in red box (figure 11e). GFM-13 is a 2.5cm wide STMB with fine cross-fractures transecting the bed and terminating abruptly at the layer boundaries. The groundmass is light grey and contrasted either side by fine-grained Pyrite-1 layers. (11b) Modal mineralogy of groundmass in the area indicated on figure e. K-feldspar is dominant mineralogy with only minor accessory mineralogy which has potentially been introduced with the precipitating vein fluids. (11c) Very fine groundmass of K-feldspar, cannot distinguish grain boundaries. Subhedral rhombus dolomite grains within the k-feldspar groundmass. (11d) Base of the STMB marked by fine-grained Pyrite-1 interlayered with dolomite. Dolomite and calcite vein infill with several coarse-grained Pyrite-2 (XRF). (11e) MLA map of area indicated by figure 11a. Thin calcite vein transecting whole layer, groundmass is largely K-feldspar, with hydrothermally introduced mineralogy to the veins and scattered throughout the layer. (11f) several subhedral zircons were identified within the MLA map and several more throughout the entire STMB. K-feldspar is too fine to determine grain boundaries, and has rutile infilling around coarse-grained Pyrite-2 with a subhedral zircon. (11g) Euhedral zircon within K-feldspar groundmass, with hydrothermal rutile infill. Apatite infill adjacent to galena, indicates both rutile and apatite are late stage infill following galena mineralisation.

2.4.2. MINALYZE DATA

Core samples GFM-0.29, GFM-23 and GFM-29 were also scanned using the Minalyzer (Figure 12), and produced significantly different analysis in comparison to MICO samples. Correlation between oxides K_2O , SiO_2 , TiO_2 and Zr is positive, and between CaO is negative. The correlations between oxides vary significantly between the samples and show greater variation than between the MICO samples. Despite this, K_2O , SiO_2 and TiO_2 all peak in association to the STMBs (Figure 12). Potassic enrichment is stronger than the MICO samples, and maximum values for GFM-0.29, GFM-13 and GFM-29 are 8.94, 9.58 and 10.31 respectively, zirconium also peaks in correlation to the STMBs, reflecting values of 429, 341 and 366ppm. The zirconium values recorded for the STMBs are significantly higher than any produced from MICO samples. Raw data found in Appendix C.

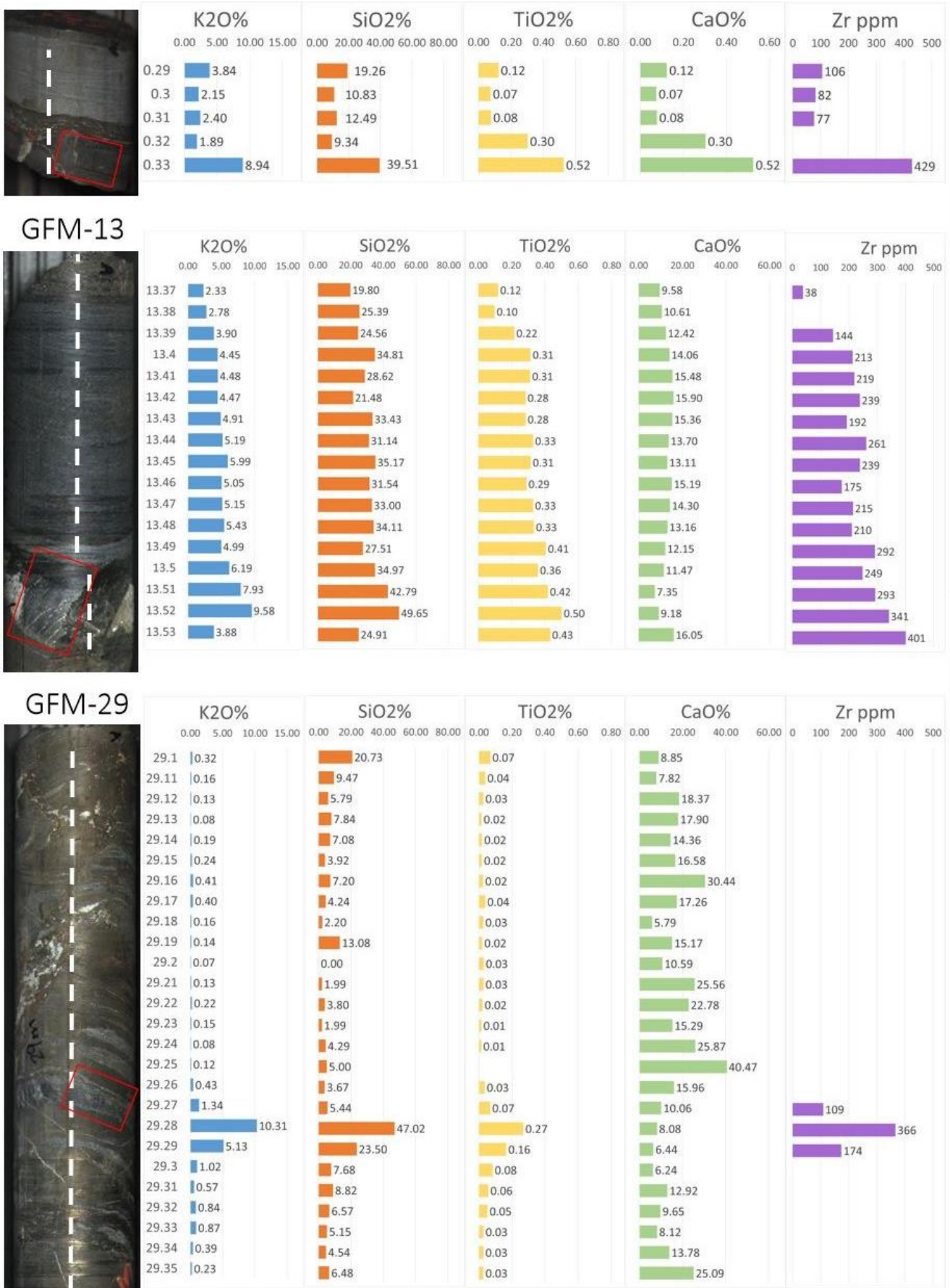


Figure 12. Minalyze data of oxides and zirconium of GFM core samples. The white dotted line shows the scanned path of the Minalyzer and the STMB thin-section area indicated by the red boxes.

2.4.3. MODAL MINERALOGY

MLA maps of all three GFM samples display a K-feldspar dominant groundmass, in comparison to all MICO samples (Table 4). Modal mineralogical abundance in weight % quantifies the disparity between the K-feldspar enrichment of the GFM samples and MICO samples. Average K-feldspar abundance of GFM samples is 95.76% compared to B175 sample average of 42.09%, A649 samples 5.89% and A826 89.46%. It is clear these STMBs are highly K-feldspar enriched, with only minor accessory minerals included or overprinting the groundmass. These samples are characterised as strongly potassic-enriched.

<i>Minerals</i>	<i>GFM-0.29</i>	<i>GFM-13</i>	<i>GFM-29</i>	<i>Average (wt%)</i>
<i>Apatite</i>	0.01	0.10	0.03	0.05
<i>Dolomite</i>	0.00	4.32	3.32	2.55
<i>Galena</i>	0.02	0.00	0.23	0.09
<i>Fluorite</i>	0.10	1.39	0.09	0.53
<i>Calcite</i>	0.10	0.66	0.16	0.31
<i>Quartz</i>	0.10	0.00	0.03	0.04
<i>Biotite</i>	0.44	0.22	1.08	0.58
<i>Pyrite</i>	0.00	0.01	0.02	0.01
<i>K-Feldspar</i>	99.02	93.25	95.02	95.76
<i>Rutile</i>	0.05	0.00	0.00	0.02
<i>Thorite</i>	0.15	0.04	0.00	0.06
<i>Zircon</i>	0.01	0.00	0.02	0.01
<i>Chlorite</i>	0.01	0.10	0.03	0.05
<i>Muscovite</i>	0.00	4.32	3.32	2.55

Table 4. Modal Mineralogy of GFM samples, showing K-feldspar is significantly enriched within the STMB groundmass.

2.5. U-Pb Geochronology

2.5.1. ZIRCONS

All zircons identified in MICO samples were subhedral and $<20\mu\text{m}$ and therefore unable to be ablated. Thirty spots out of the collective 245 GFM samples were $>20\mu\text{m}$, which were ablated using a beam size of $19\mu\text{m}$. These samples contained mostly euhedral to subhedral zircons, indicating the potential for volcanic ash-fall origin (Figure 13). The small size of the GFM zircons, meant the laser only captured a small signal of the zircon before passing through the grain and contaminating the signal. Because of these samples being a part of a lead ore system, U-Pb is not exclusive to zircons and therefore only the initial part of the signal was valid. Iolite processing of the zircon data revealed of the 30 spots, only 28 produced a signal. After reducing the signal to the initial response, using Isoplot R, the data had no significance and would not produce an age constraint, despite efforts to reduce the dataset.

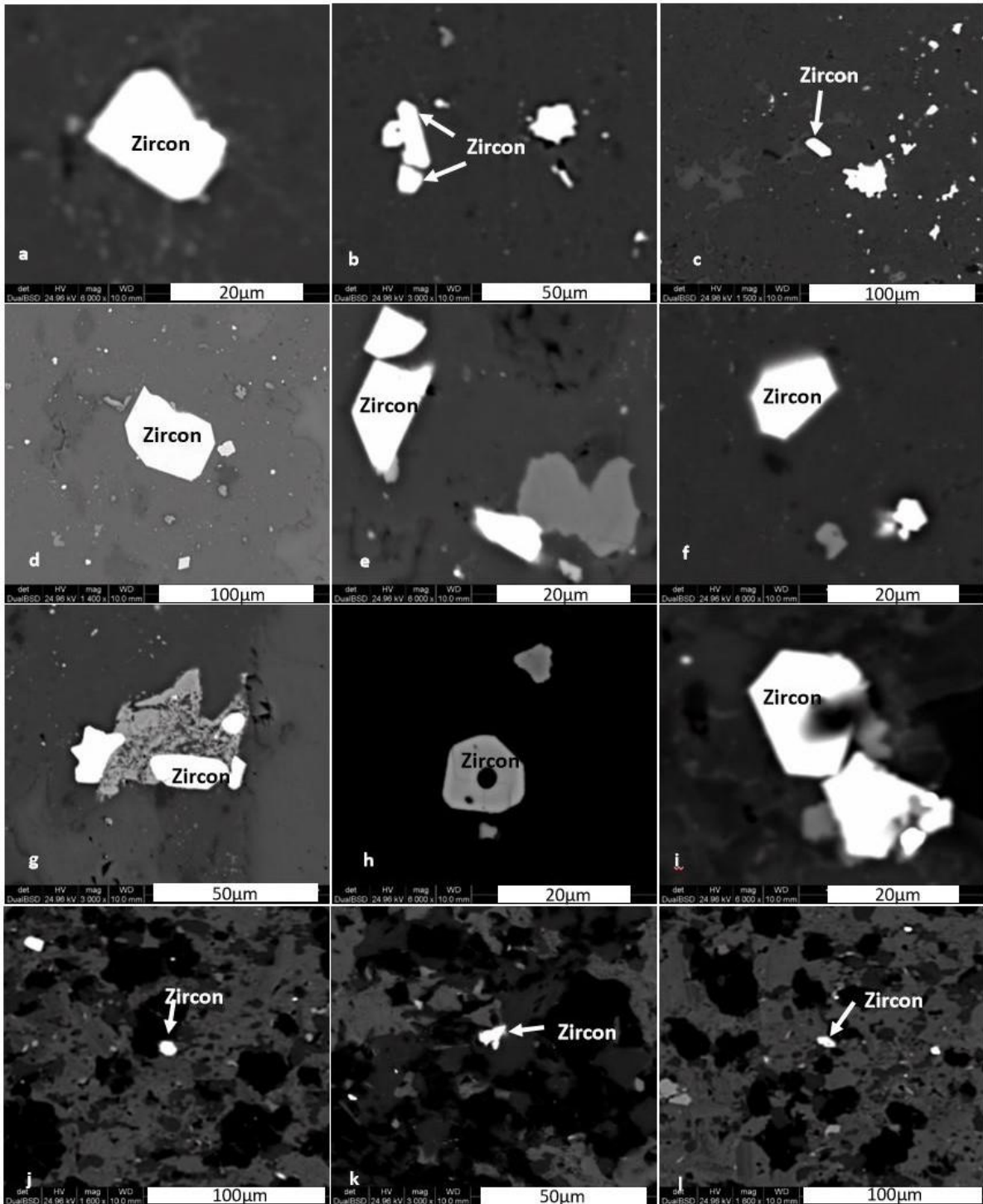


Figure 13. SEM images of zircons from GFM samples and MICO samples B175-A and B175-B, obtained from the STMB layers. GFM zircons (a-i) are mostly euhedral with some rounded-subhedral grains found throughout the layers. The rounded zircons are interpreted to be of detrital origin, and the euhedral zircons indicative of igneous/ash fall origin. MICO zircons (j-l) identified in the groundmass are mainly rounded, with no obvious euhedral grain boundaries preserved, indicating a detrital source.

2.5.2. MONAZITES

Monazites were observed heterogeneously dispersed throughout groundmass in all STMB samples associated with silica-dolomite veins in zones of deformation and brecciation as pictured in Figure 15. Both MICO and GFM samples contained anhedral, fine-grained monazite, over 90% of which were $<13\mu\text{m}$. Only 12 spots of the 21 that were ablated recorded a signal. The irregularity of the monazite grain boundaries increased the difficulty of spot analysis, whilst also indicating a potential hydrothermal origin. Upon reducing the signal to the initial recorded response, a discordant age was produced. The original age including all 12 analyses yielded a weighted average $^{207}\text{U}/^{206}\text{Pb}$ age of $1514\pm 51.1\text{Ma}$ (Figure 14a). Excluding data points 1, 3, 8 and 9, due to outlier analyses, the data set was reduced to 8 spots which produced a discordant weighted average $^{207}\text{U}/^{206}\text{Pb}$ age of $1571.8\pm 78.6\text{Ma}$ (Figure 14b). The uncertainty increased significantly when the 4 data points were excluded ($51.1\text{Ma} \pm 78.6\text{Ma}$), due to the lacking number of analyses involved.

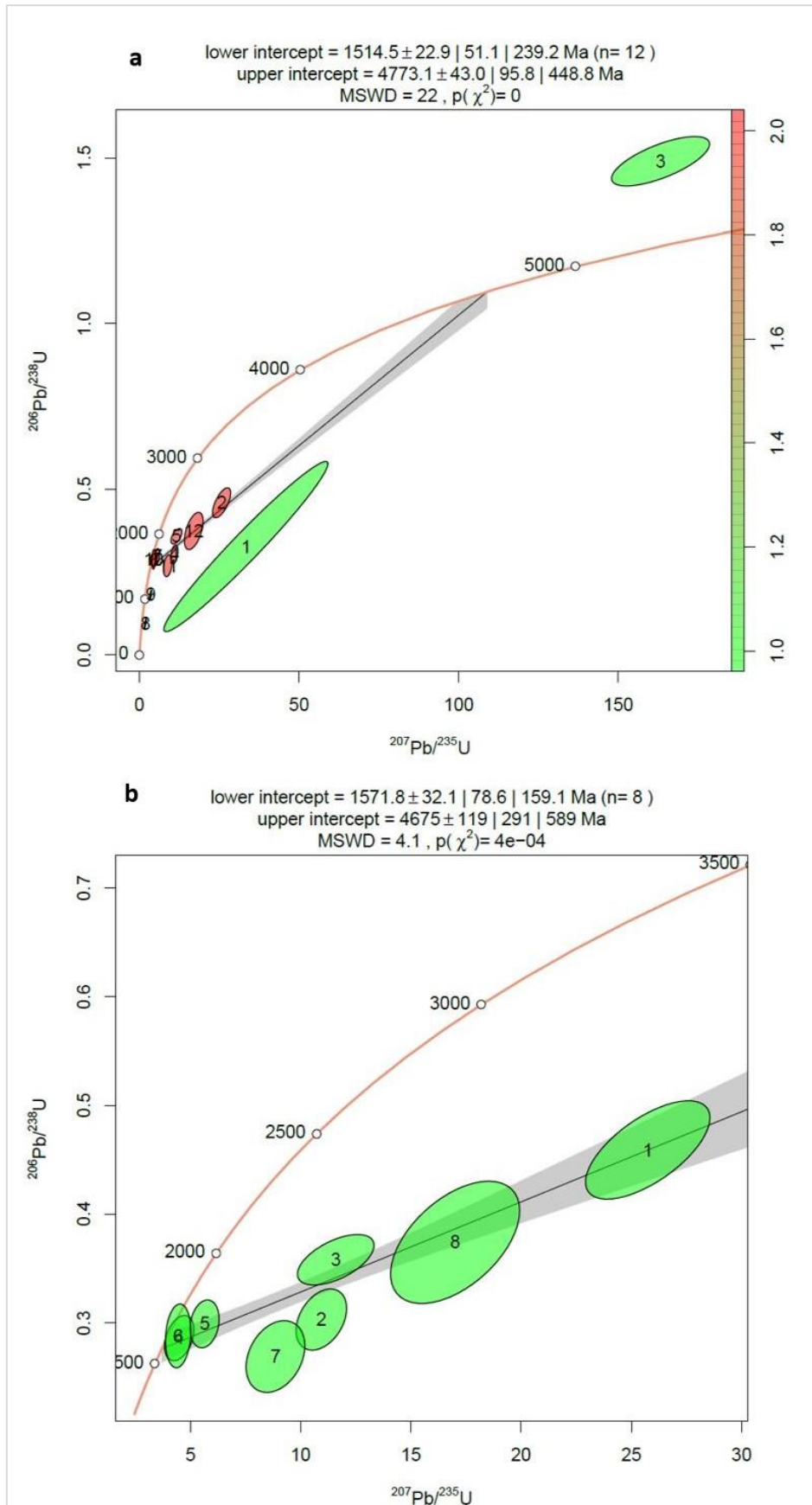


Figure 14. Monazite Geochronology. (13a) all 12 monazite samples included in analysis, producing an age of 1514 ± 51.1 Ma. (13b) geochronology of 8 monazite samples to obtain best fit age average, 4 data points from figure 13a were excluded from analysis, yielding a weighted average $207\text{U}/206\text{Pb}$ age of 1571.8 ± 78.6 Ma.

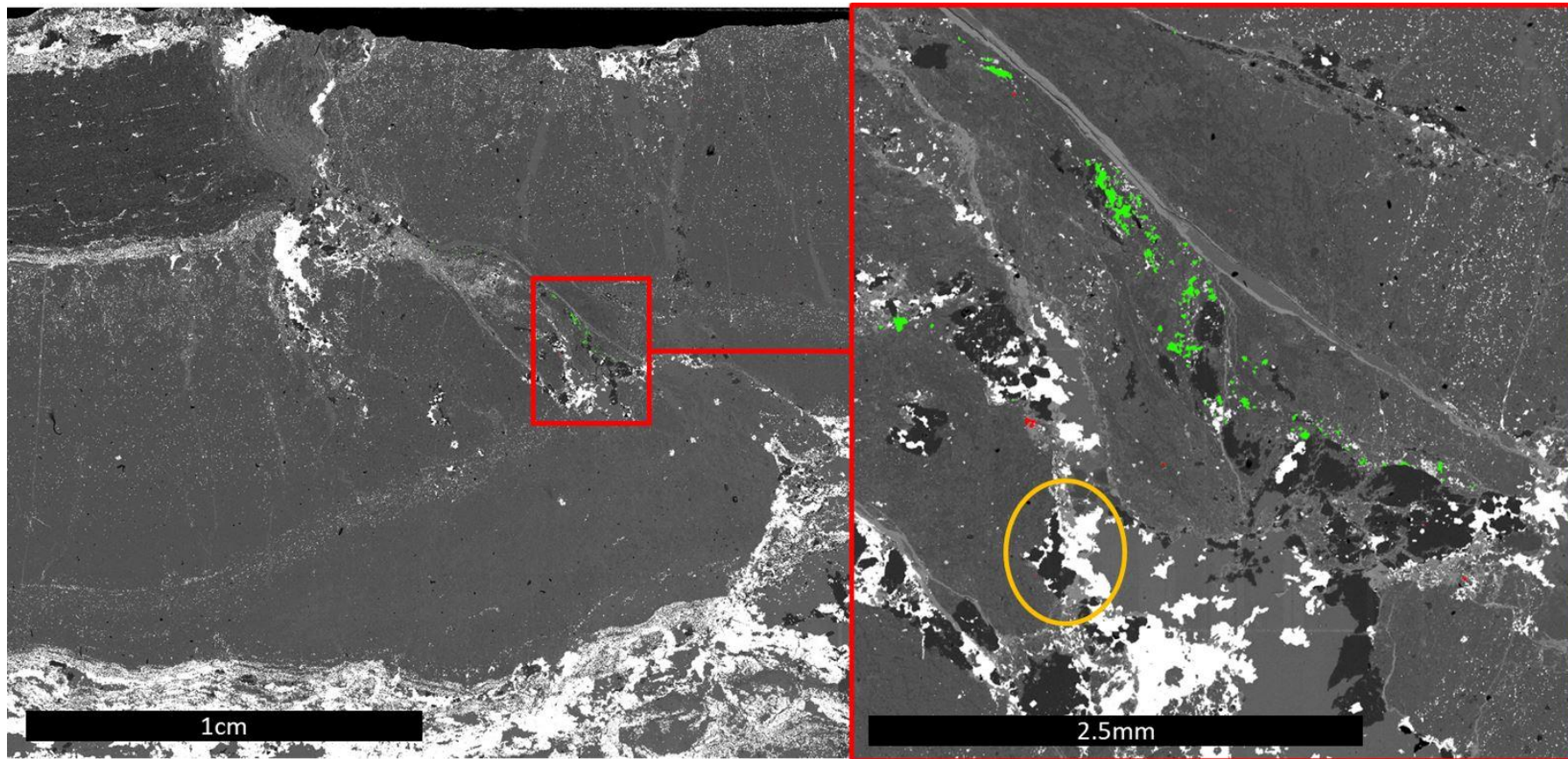


Figure 15. Backscattered SEM image, with MLA mineral map incorporated to highlight location of monazite samples (green) and zircons (red) in sample GFM-0.29. The layer has experienced soft sediment compressional deformation (the bulge/deformed bed), resulting in the formation of a reverse-fault and stylolite structures prior to fine-grained Pyrite-1 formation. No Pyrite-1 grains have experienced deformation. Post-deformation quartz (nearly black in backscattered light) has formed veins and infilled the reverse fault zone (indicated by red box) and has a close spatial association with anhedral monazite grains. Sulphide mineralisation (bright coloured in backscattered light) appear to brecciate and infill around quartz and monazite grain (example indicated by yellow circle).

2.6. GEOCHEMICAL COMPARATIVE ANALYSIS

The EDS analysis of minerals and abundance of minerals were combined to generate a representative whole-rock geochemistry dataset for the analysed samples. While this method is noted as only being approximate, it is considered fit-for-purpose for this project to display variation of major elements between heterogeneous samples from this study. Croxford (1965) and modern TMB studies included in this geochemical analysis each used different sampling and analytical methodologies.

The plot of Al versus Ti weight percent (Figure 16) separates samples into three groups; A649 (low Al, low Ti), GFM-0.29, GFM-29 and B175-D (low-moderate Al, and low Ti), and A826 and B175-A, B, C (moderate Al, low Ti). Shale samples show large variation from moderate – high Al, and low Ti. Croxford's data is most similar to the moderate Al and low Ti group. However, there is no significant relationship between the samples and Croxford's data, likewise with the known tuffs. India data plot in a group above two of the GFM data points, whereas, China 1, China 2 and New Zealand datasets have significantly higher Ti weight percent compared to the aforementioned analyses. The plot Si versus Na+K weight percent (Figure 16) further highlights the variability in samples and the lacking correlation with modern tuff samples of China 1, China 2, India and New Zealand. Croxford's (1964) data does show similarities with sample A826, as it did in the Al versus Ti plot. However, several shale samples also plot within the same area of high Na+K and high Si wt%. MICO samples B175-A-D and GFM-13 plot in proximity to Croxford (1964), however, GFM-0.29 and GFM-29 plot in moderate Si and Na+K space, whereas A649 differs significantly from all other samples, with low Si and low Na+K bulk composition.

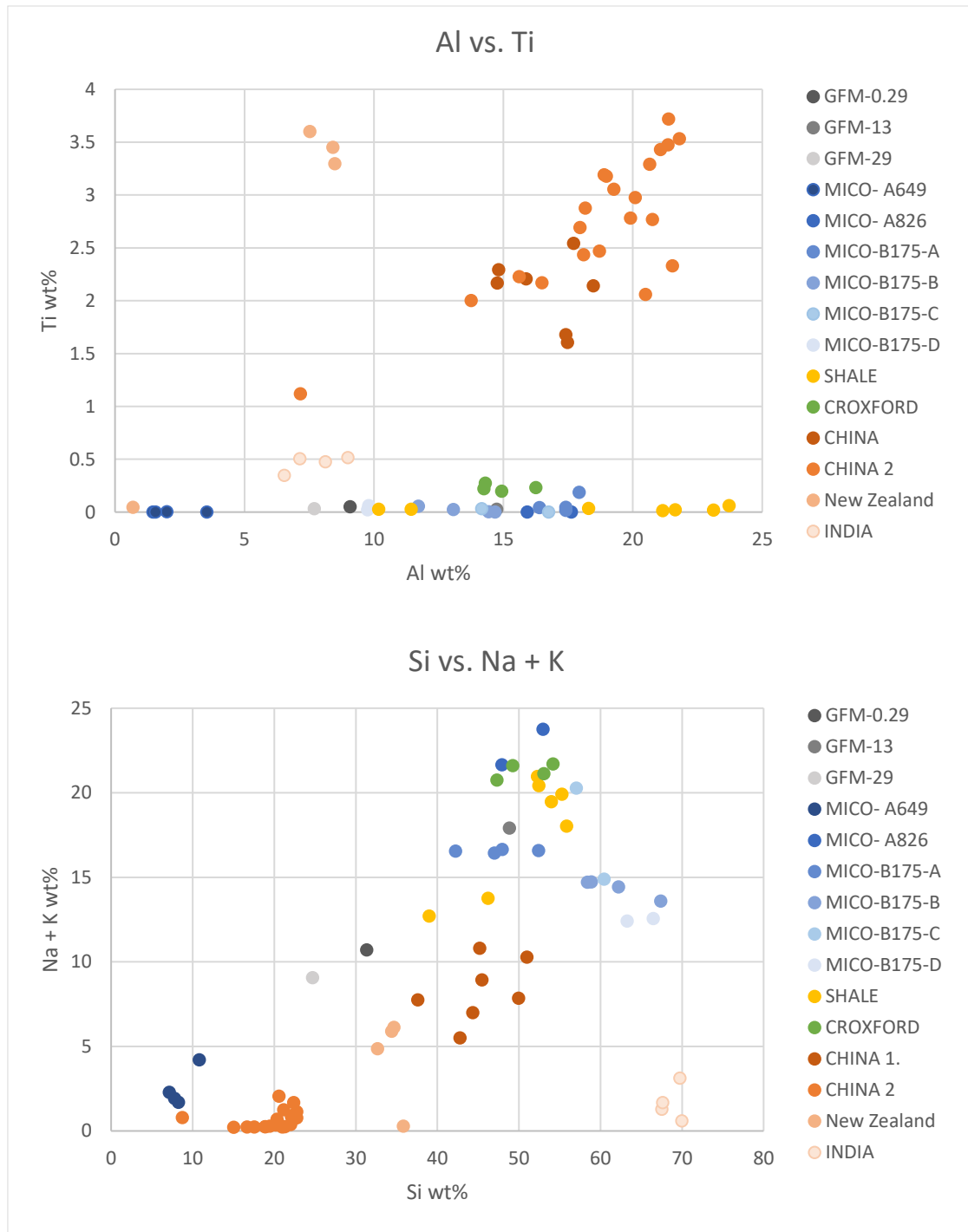


Figure 16. Discrimination plots of geochemical data from MICO and GFM samples in comparison to Croxford (1964) and known tuffs from around the world. (15a) Al versus Ti weight percent. (15b) Si versus Na+K weight percent.

3. DISCUSSION

3.1. Comparison to Previous Work

While this study has not been able to fully replicate the observations made by Croxford (1964), all samples conform to his simplistic description of being grey in colour, hard, brittle and cherty with abundant cross-fractures. Geochemically, the understanding that TMBs are the most significantly potassium enriched layers in the Urquhart Shale is found to be inaccurate and on-site hydrofluoric acid (HF) staining test is therefore not a definitive test for TMBs. Consequently, non-TMBs were logged as TMBs by the author and MICO geologists and hence their inclusion in this study; highlighting the difficulty in identifying TMBs from hand sample alone.

Notable correlations between Croxford (1964) and analysed samples include; cross-fractures at high angle to bedding which terminated sharply at the boundaries and contain variable mineral and textural composition. Thickness of beds remained uniform over large distances, except where interpreted sedimentary scouring and the formation of stylolites occur (sample GFM-0.29) (Figure 15 and Appendix B); and subhedral-euhedral rhombus dolomite grains were identified within the very-fine K-feldspar groundmass of GFM-13 (Figure 11c) and GFM-29 (Appendix B). Whilst the spectra of these grains were not recorded; elemental composition of dolomite was variable among samples and could have been ferroan dolomite, as observed by Croxford (1964).

3.1.1. ORIGIN OF POTASSIUM ENRICHMENT

Croxford (1964) suggested feldspars originated as low temperature monoclinic orthoclase which inverted to triclinic microcline in the 'potash rich' beds. However, K-feldspar groundmass was too fine to see individual grains, and no microcline was

recognised despite using the highest magnification available on Olympus BX51 microscope and FEI Quanta 600 MLA/SEM. If the feldspars have experienced structural re-ordering, the degree of triclinicity will provide insight into the thermal/isotopic history (Arriens, Brooks, Boffinger, & Compston, 1966; Farquharson & Richards, 1975). While further high resolution petrography may concur with Croxford's (1964) observations, discerning whether these compositions are the result of interaction with connate water, diagenetic or hydrothermal processes, remains unconstrained.

3.1.2. ZIRCONS

Zircons from TMBs define the age of the Urquhart Shale (1652 ± 7 Ma at Mount Isa and 1655 ± 4 Ma at George Fisher), (Page et al., 2000; Page & Williams, 1988). Scanning electron photomicrographs, Page (1981) (Figure 17a and 17b), observed an elongate cast of rutile or spinel blade on one of the zircon crystals, suggesting it had crystallised from the primary magma adjacent to the zircon. This was used to substantiate Croxford (1964) and Croxford & Jephcott, (1972) observation that rutile crystals in the matrix outlined and accentuated (what were interpreted to be) volcanic shards, which gave the appearance of a vitroclastic texture (Figure 17d). In the GFM samples, examples of euhedral rutile in contact with zircon have been observed (Figure 17c). However, further work is required to determine whether the rutile is hydrothermal infill or of igneous origin. The presence of euhedral rutile crystals in addition to zircons suggest they were originally deposited as volcanic debris. However, in the context of the surrounding lithologies and the ubiquitous presence of anhedral hydrothermal alteration and infill minerals, including rutile, the example from this study has not been interpreted to impart a vitroclastic texture. The descriptions of Croxford (1964),

Croxford and Jephcott (1972) and Page (1981) cannot be collaborated. Further work on the origin of rutile, and why it should be interpreted as devitrified volcanic glass may need to be undertaken. Evidence from this study indicates an origin as a hydrothermal product as both alteration and infill.

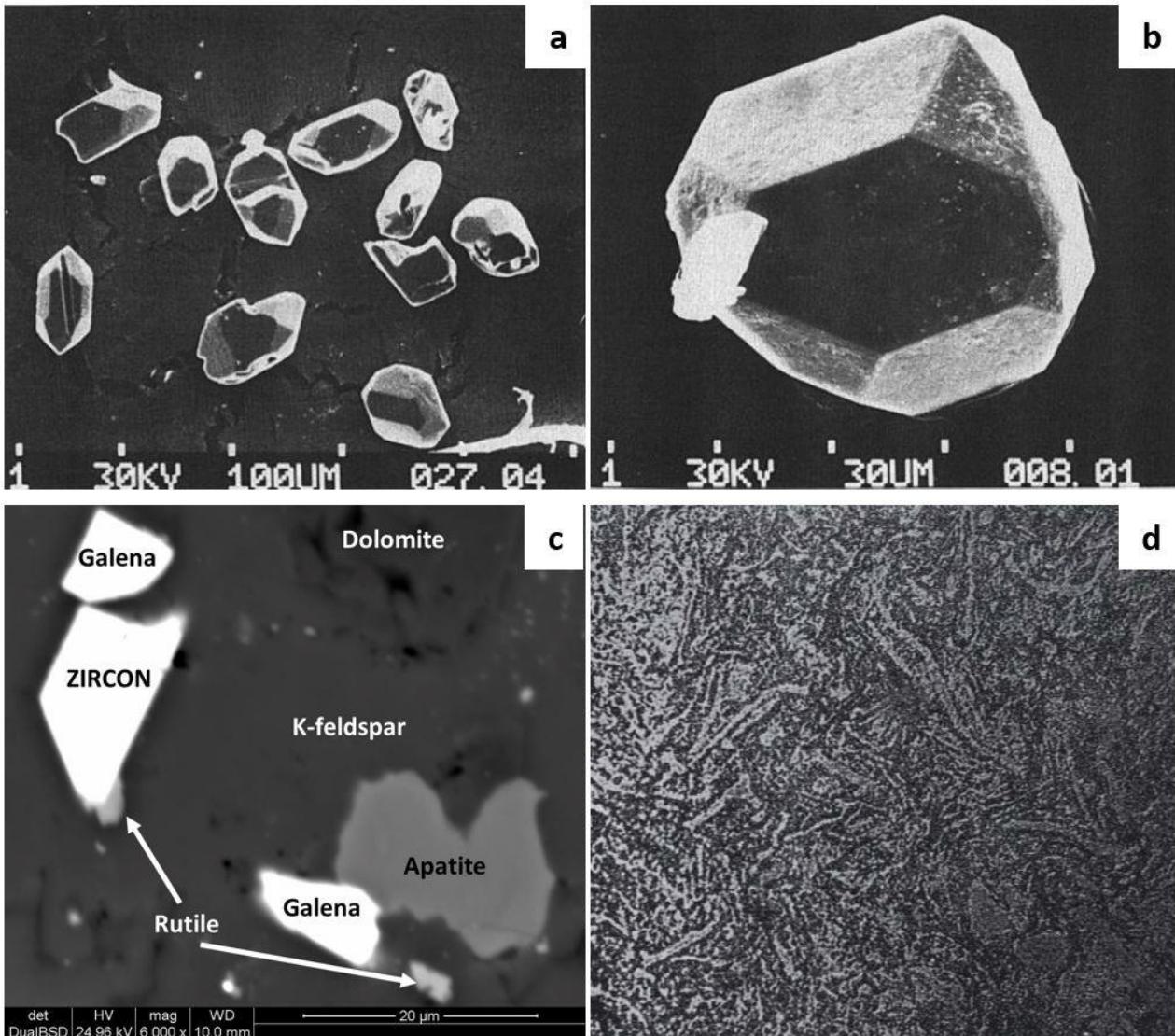


Figure 17. Comparison of Croxford (1964) rutile imparting a vitroclastic texture and examples from Page (1981) and sample GFM-13. (17a) Scanning electron photomicrograph of a population of zircon grains from the Urquhart Shale tuff marker bed, showing all euhedral grains and notably an elongate cast of a rutile blade present on one of the zircon crystals in the far left (circled) (Page 1981). (17b) Perfectly euhedral zircon with cast of rutile from tuff maker bed in the H.Y.C Pyritic Shale Member of the McArthur Group (Page, 1981). (17c) Euhedral zircon from sample GFM-13, showing euhedral rutile growing on or as infill around the zircon, further imaging required to determine. (17d) Tuff Marker Bed from Drill hole S78, No 1 at 110ft, at Mount Isa Mine, showing the vitroclastic texture. Shard outlines are accentuated by rutile and some sericite in the dark matrix. Plane-polarised light (Croxford, 1964).

The presence of euhedral zircons has been the key observation in identifying TMBs in previous studies (Croxford, 1964; Croxford and Jephcott, 1972; Farqharson, 1975; Page, 1981). Based on this criterion, samples that do not contain euhedral zircons have not been validated as TMBs in this thesis. Therefore, all GFM samples have been classified as TMBs, and all MICO samples have not. The factors contributing to this classification, and the framework of determining criteria has been established and is discussed below.

3.2. Classification Framework

3.2.1. PETROLOGY (OPTICAL AND SEM/MLA)

Initial optical petrology recognised three categories of variation in groundmass composition; carbonaceous (dolomitic), moderately potassium enriched and strongly potassium enriched. The carbonaceous group was comprised of samples A649-1, 2 and 3; dolomitised layers with cross-fractures terminating at the boundaries. The moderately potassium enriched group included samples with more compositional variation, including samples B175-A, B C and D. Sample B-175-D (Figure 9) exhibited post lithification deformation, with late stage, post- D2 deformation timing for mineralisation of pyrrhotite. Neither of these TMB groups displayed fining-upwards textures and cross-fractures were limited in number. Additionally, the absence of euhedral zircons indicated both the carbonaceous and moderately potassium enriched samples are not ash-fall derived TMBs.

Sample A826 is included in the strongly potassic enriched group, however, petrology identified key differences from the GFM samples. The groundmass in A826 was very fine-grained K-feldspar (~10µm) with distinctive cross-fractures indicating later fluid

ingression. The GFM samples however, are K-feldspar dominated, very fine grained with hard to identify grain boundaries (giving the appearance of a solid layer of K-feldspar), resulting in a stark contrast with the adjacent layers in the MLA maps (e.g. Figure 11e). The cross-fractures are not as distinct in GFM samples and the homogeneity of the groundmass accentuated the inclusions of euhedral zircons (<20 μ m). No zircons were identified in A826 using MLA maps, while a collective 245 were identified from MLA maps of the GFM samples. The presence of euhedral zircons is consistent with the interpretation they are crystalline debris within the tuffs, which were volcanically expelled (Page, 1978; Page & Williams, 1988; Perkins, 1996).

3.2.2. MINALYZE DATA

Tuff Marker Beds at Mount Isa have previously been described as potassic-rich volcanic rocks (Croxford, 1964), therefore Minalyze data should observe a distinct increase in potassium across the suspected TMB layers. However, the distribution of potassium and the variation in composition of layers above and below the STMBs was greater than expected. The peaks in K₂O do not strongly correlate to MICO STMBs and most likely a response to the variable potassic composition of the Urquhart Shale. GFM samples display a substantial increase correlated to the STMB, however, the highest K₂O values for shale were 11.59% and 10.31%, therefore, high K₂O does not equate to a TMB. The widespread distribution of K-feldspar rich layers indicates potassium enrichment within the Urquhart Shale is not confined to TMBs. Because the K-feldspar enrichment is intercalated and spatially associated with base-metal mineralisation, it is very likely that the layers have been affected by hydrothermal fluid migration. Therefore it can be interpreted that some of these unusually K-feldspar rich beds are not genuine air-fall tuffs (Davidson, 1998; Page et al., 2000) and may represent hydrothermal alteration to

the measured compositions. Consequently, K₂O is not a stand-alone pathfinder for TMBs when interpreting Minalyze data. However, K₂O abundance in GFM TMBs correlates to peaks in zirconium. The potential exists to compose an algorithm for Minalyze processing software to automatically identify TMBs based on the combined abundance of K₂O and Zr. From the limited data analysed, values above 8wt% K₂O and 250ppm Zr are suggested to be a reasonable starting point for discriminating TMBs.

3.2.3. MONAZITE GEOCHRONOLOGY

The weighted average ²⁰⁷U/²⁰⁶Pb age of monazite from GFM samples is 1571.8±78.6Ma and is within error of all major events related to the Mount Isa Group sediments, including the formation of the Urquhart Shale at GFM (1655±4 Ma), D₁ (1610±13Ma), D₂ (1544±12Ma), D₃ (1510±13Ma) (Bain, Heinrich, & Henderson, 1992; Bell, 1983; Bell et al., 1988; Page & Bell, 1986). The large error limits the ability to speculate as to which event these monazites are related, however, paragenetic timing established from sample GFM-0.29 (Figure 15) indicates the monazites post-date; deposition of the Urquhart Shale, soft sediment deformation, brittle deformation and fine-grained Pyrite-1 formation. This paragenesis indicates the yielded monazite date of 1571.8±78.6Ma is not associated with the formation (and subsequent soft-sediment deformation) of the Urquhart Shale. The anhedral nature of all monazites observed and their close association with anhedral quartz infill within zones of deformation (Figure 15) provide evidence that the genesis of monazites can be related to the silica-dolomite alteration event. Silica-dolomite alteration represents the beginning of the extended ore-stage (Taylor & Lilly, 2016) and has been associated with early stage D₃ (1510±13Ma) (Bain et al., 1992; Bell, 1983; Bell et al., 1988; Page & Bell, 1986). Sphalerite can also be observed to brecciate and infill around the quartz and monazite, demonstrating that the

analysed monazites pre-date mineralisation. These observations indicate that the monazite dates generated by this study (despite the large errors) may represent an age of the initiation of the main hydrothermal event responsible for mineralisation at George Fisher and Mount Isa.

3.2.4. GEOCHEMISTRY

In comparison the known tuff samples (which illustrate modern geochemical variation in volcanic rocks), Croxford's (1964) geochemical data of Mount Isa TMBs plot within proximity to MICO samples A826, B175-A, B and C, GFM-13 and shale samples.

Croxford (1964) claimed that TMBs may reflect the parent magma based on the assumption that little post-depositional chemical alteration has taken place. However, the data display that the geochemistry of Croxford's (1964) tuffs are not too dissimilar of non-tuffs, and therefore whole-rock geochemistry signatures for these TMB samples may not be characteristic of the source rocks and possibly providing further evidence of post-depositional alteration. The extensive and pervasive hydrothermal alteration system preserved at Mount Isa and George Fisher clearly demonstrate that TMBs have been hydrothermally altered at some point and that their composition will spatially vary between samples.

3.2.5. IMPLICATIONS FOR ORE GENESIS

The paragenesis of samples GFM-0.29 (Figure 15) and MICO B175-D (Figure 9), imply economic mineralisation is post-sedimentation and major deformation of the Urquhart Shale. The petrography of all MICO and GFM samples observes undeformed sulphides as a combination of vein- and breccia-hosted infill and alteration. The observations in this thesis concur with epigenetic ore formation, as proposed by

Grondijs and Schouten (1937), Blanchard and Hall (1937), Perkins (1997) and Taylor and Lilly (2016).

3.2.6. ECONOMIC SIGNIFICANCE

TMBs are relied on as chronostratigraphic marker horizons within the mine workings of the stratabound Pb-Zn orebodies at GFM. However, the lateral variation of these TMB horizons within mine workings has meant that even zircon-bearing TMBs used regularly as stratigraphic markers may be defined in the stratigraphic log as ‘not located consistently’, ‘difficult to locate’ and ‘not always present’.

The absence of fining upwards sequences and the homogeneity of the K-feldspar dominant composition of GFM TMBs, is also inconsistent with an ash-fall origin. However, it is consistent with the interpretation that zircon-bearing GFM TMBs have also been affected by hydrothermal processes. Therefore, GFM TMBs most likely record cyclicity of sedimentation and episodic volcanism in the palaeo-basin. However no other evidence of syn-sedimentary hydrothermal activity has been recorded. The observed overprinting replacive and vein infill textures of the economic sulphide minerals provide evidence that GFM TMBs are unrelated to the formation of the Mount Isa and George Fisher ore system. No further research on Mount Isa or George Fisher TMBs with regard to their relationship to the causative hydrothermal ore system is proposed.

4. CONCLUSIONS

- Despite visual similarities, TMBs sampled for this project from Mount Isa Mines Copper Operation (MICO) did not have dominantly fine-grained K-feldspar groundmass, fining-upwards sequences or euhedral zircons, and are not TMBs.

(Hypothesis 1)

- TMBs sampled for this project from George Fisher Mine (GFM) have a fine-grained K-feldspar groundmass, euhedral zircons and are interpreted as 'true' TMBs of air-fall tephra origin. **(Hypothesis 1)**
- GFM 'true' TMBs have subsequently been affected by hydrothermal processes based on the interpretation of their compositional homogeneity and lack of fining-upwards sequences. **(Hypothesis 1)**
- Euhedral zircons in the GFM TMB samples indicate proximal volcanism has occurred during the formation of the Urquhart Shale.
- Potassium enrichment is not confined to TMBs. **(Hypothesis 2)**
- Because of their fine-grained textures and subsequent hydrothermal alteration, TMBs are a challenging lithology to investigate, and difficult to recognise from mineralogy, texture and geochemical composition alone.
- Potassic enrichment is more extensive within the Urquhart Shale than expected and therefore, hydrofluoric acid staining alone is not a reliable indicator for TMBs.
- While a high concentration of K_2O and Zr has the potential to be representative of a TMB, the current use of (Minalyze) XRF data is not a stand-alone tool for identifying TMBs.
- The potential exists to compose an algorithm for Minalyze processing software to automatically detect suspected TMBs based on the abundance of K_2O and Zr.

- The origin of potassium enrichment is related to the composition of the original detrital sediments (including possible ash-fall tephra) as well as a currently unconstrained hydrothermal component. **(Hypothesis 3)**
- The paragenesis observed throughout analysed samples supports epigenetic Pb-Zn-Ag and Cu formation, with economic mineralisation taking place co-genetically during a prolonged hydrothermal event.
- It is proposed that the strongly potassic composition of GFM TMBs is the result of a combination of primary sediment composition and hydrothermal alteration related to mineralisation.
- It is proposed that TMBs are not temporally related to a syn-genetic ore system.

5. RECOMMENDATIONS FOR FURTHER STUDY

This thesis recommends the discontinuation of toxic HF staining on site, and suggests a multifaceted approach involving Minalyze data and detailed petrology to identify TMBs. The inclusion of a greater sample size of ‘true’ TMBs will enable further work using Minalyze data to create a discriminatory algorithm. It is suggested that confirmation of ‘true’ TMBs will require SEM/MLA as conducted in this thesis.

Additional samples would also reduce the large error associated with the monazite date to further constrain the timing of the silica-dolomite event, including the use of data and samples from previous Honours projects (e.g. Lintvelt, 2017). Additionally, there is very limited research on discriminating diagenetic from hydrothermal K-feldspar (Davidson, 1998). Further work on this topic may assist in the identification of a K-feldspar ‘halo’ to mineralisation of the Mount Isa and George Fisher ore system.

6. ACKNOWLEDGEMENTS

I would like to acknowledge the generosity of the many people who have assisted and supported me this year. Firstly, I would like to thank my supervisor, Dr Richard Lilly, for his direction and support this year. I am extremely grateful to Mount Isa Copper Operations (MICO) for the opportunity to complete a summer vacation program, and am humbled by the offer of a Graduate position in 2019. A special thanks to Dan Taylor and all the MICO geologists and coreshed team for their support and encouragement throughout my vacation program and throughout the year. I would like to thank Nick Spanswick and the George Fisher Mine geologists for their assistance with my sampling and the use of the Minalyzer. To the Minalyze team, in particular, Angus Tod and Mark Manly for their patience and innovation. To the staff at Adelaide Microscopy; Dave Kelsey and Sarah Gilbert, for their knowledge and expert advice throughout the year. To Brad Cave for his direction and assistance with processing data. To my partner for the reassurance and unconditional support. To my fellow honours students whom have provided comic relief and emotional support throughout the year, I couldn't have done it without you all.

Additionally, the Glencore scholarship program for financial assistance which has allowed me to dedicate my time and energy to my thesis this year. I am eager to join the MICO team in 2019.

7. REFERENCES

- ARRIENS, P. A., Brooks, C., Boffinger, V. M., & Compston, W. (1966). The discordance of mineral ages in granitic rocks resulting from the redistribution of rubidium and strontium. *Journal of Geophysics Research*, 71, 4981-4994.
- BAIN, J. H. C., Heinrich, C. A., & Henderson, G. A. M. (1992). Stratigraphy, structure and metasomatism of the Haslingden Group, east Moondara area, Mount Isa: a deformed and mineralised Proterozoic multistage rift-sag sequence. *Australian Geological Survey Organisation Bulletin*, 243, 125-136.
- BELL, T. H. (1983). Thrusting and duplex formation at Mount Isa, Queensland, Australia. *Nature*, 304(493-497).
- BELL, T. H., Perkins, W. G., & Swager, C. P. (1988). Structural controls on the development and localisation of syntectonic copper mineralisation at Mount Isa, Queensland. *Economic Geology*, 83. doi:10.2113/gsecongeo.83.1.69
- BENNETT, E. M. (1965). Lead-zinc-silver and copper deposits of Mount Isa (Vol. 1): *Commonw. Min. Meall. Congr.*
- BLAKE, D. H. (1987). *Geology of the Mount Isa Inlier and environs, Queensland and Northern Territory: Australian Govt. Pub. Service.*
- BLANCHARD, R., & Hall, G. (1937). Mount Isa (Queensland) ore deposition. *Economic Geology*, 32, 1042-1057.
- BRIGGS, R. M., Rosenberg, M. D., deLange, P. J., Itaya, T., King, P. R., & Price, R. C. (2010). Geology and geochemistry of Gannet (Karewa) Island, Tasman Sea: A rift-related nephelinitic tuff ring. *New Zealand Journal of Geology and Geophysics*, 40(3), 263-273. doi:10.1080/00288306.1997.9514759
- CONNELL, S. J. (2016). Fine-grained pyrite within the Mount Isa (Enterprise) copper system, NW Queensland; geological relationships, modelled distribution and links to reactive ground. *The University of Adelaide, Honour Thesis.*
- CROXFORD, N. J. W. (1964). Origin and Significance of Volcanic Potash Rich Rocks from Mount Isa. *Transactions of the Institution of Mining and Metallurgy*, 74, 33-43.
- CROXFORD, N. J. W., & Jephcott, S. (1972). *The McArthur lead-zinc silver deposit, Northern Territory, Australia.*
- DAVIDSON, G. J. (1998). Alkali alteration styles and mechanisms, and their implications for a 'brine factory' source of base metals in the rift-related McArthur Group, Australia. *Australian Journal of Earth Sciences*, 45, 33-50. doi:10.1080/08120099808728365
- DOMAGALA, J., Southgate, P. N., McConachie, B. A., & Pidgeon, B. A. (2000). Evolution of the Paleoproterozoic Prize, Gun and lower Loretta Supersequences of the Surprise Creek Formation and Mount Isa Group. *Australian Journal of Earth Sciences*, 47(3), 485-507. doi:10.1046/j.1440-0952.2000.00796.x
- DU, Q., Wang, Z., Wang, J., Deng, Q., & Yang, F. (2015). Geochronology and geochemistry of tuff beds from the Shicaohe Formation of Shennongjia Group and tectonic evolution in the northern Yangtze Block, South China. *International Journal of Earth Sciences*, 105(2), 521-535. doi:10.1007/s00531-015-1182-2
- ETHRIDGE, M., & Wall, V. (1994). Tectonic and structural evolution of the Australian Proterozoic. *Geological Society of Australia Abstracts*, 37, 102-103.
- FARQUHARSON, R. B., & Richards, J. R. (1975). Isotopic Remobilisation in the Mount Isa Tuff Beds. *Chemical Geology*, 16(2), 73-88. doi:10.1016/0009-2541(75)90001-7
- GESSNER, K., Jones, P. A., Wilde, A. R., & Kuhn, M. (2006). Significance of strain localization and fracturing in relation to hydrothermal mineralization at Mount Isa,

- Australia. *Journal of Geochemical Exploration*, 89(1-3), 129-132.
doi:10.1016/j.gexplo.2005.11.048
- GREGORY, M. J., Wilde, A. R., Schaefer, B. F., & Keays, R. R. (2005). Potassic alteration and veining and the age of copper emplacement at Mount Isa, Australia. Berlin, Heidelberg: Springer.
- GRONDIJS, H. F., & Schouten, C. (1937). A Study of the Mount Isa Ores. *Economic Geology*, 32, 407-450. doi:10.2113/gsecongeo.32.4.407
- LILLY, R. (2017). Mount Isa Cu-Pb-Zn deposit including George Fisher deposit.
- LINTVELT, C. L. (2017). Mineralogical and Geochemical Investigation of Silver and Cobalt Trace Metals in the Mount Isa Copper Deposit. The University of Adelaide, Honours Thesis.
- MAGUIRE, B. (2016). Characterisation and timing of faults with respect to copper mineralisation and talc alteration in the Northern 3500 orebody, Mount Isa, Northwest Queensland. The University of Adelaide, Honours Thesis.
- MATHIAS, B. V., & Clark, G. J. (1975). Mount Isa copper and silver-lead-zinc orebodies—Isa and Hilton mines. *Economic Geology of Australia and Papua New Guinea*, 1, 351-372.
- MCLELLEN, J., O'Sullivan, R., Miller, B., & Taylor, D. (2014). Geomechanical modelling of the Mount Isa copper deposit—predicting mineralisation. . Paper presented at the Proceedings Ninth International Mining Geology Conference 2014.
- MILLER, J. (2007). Structural controls on the Mount Isa copper deposit, Queensland. Predictive Mineral Discovery Cooperative Research Centre.
- NEUDERT, M. K. (1983). A depositional model for the Upper Mt. Isa Group and implications for ore formation. Canberra, Australian National University.
- NEUDERT, M. K. (1984). Are the Mount Isa Lead-Zinc Ores Really Syngenetic? *Geological Society of Australia Abstracts*(12).
- PAGE, R. W. (1978). Response of U-Pb zircon and Rb-Sr total-rock and mineral systems to low grade metamorphism in Proterozoic igneous rocks, Mount Isa, Australia. *Journal of the Geological Society Australia*, 25(3), 141-164.
doi:10.1080/00167617808729025
- PAGE, R. W. (1981). Depositional Ages of the Stratiform Base Metal Deposits at Mount Isa and McArthur River, Australia, Based on U-Pb Zircon Dating of Concordant Tuff Horizons. *Economic Geology*, 76, 648-658.
- PAGE, R. W., & Bell, T. H. (1986). Isotopic and structural responses of granite to successive deformation and metamorphism. *The Journal of Geology*, 365-379.
- PAGE, R. W., Jackson, M. J., & Krassay, A. A. (2000). Constraining sequence stratigraphy in north Australian basins: SHRIMP U–Pb zircon geochronology between Mt Isa and McArthur River. *Australian Journal of Earth Sciences*, 47, 431-459.
doi:10.1046/j.1440-0952.2000.00797.x
- PAGE, R. W., & Sweet, I. P. (1998). Geochronology of basin phases in the western Mt Isa Inlier, and correlation with the McArthur Basin. *Australian Journal of Earth Sciences*, 45(2), 219-232. doi:10.1080/08120099808728383
- PAGE, R. W., & Williams, I. S. (1988). Age of the Barramundi Orogeny in northern Australia by means of ion microprobe and conventional U-Pb zircon studies. *Precambrian Research*, 40(1), 21-36. doi:10.1016/0301-9268(88)90059-9
- PAINTER, M. G. (2003). The geochemical and mineralogical haloes around the Mount Isa base metal orebodies.
- PERKINS, W. G. (1984). Mount Isa Silica Dolomite and Copper Orebodies: The Result of a Syntectonic Hydrothermal Alteration System. *Economic Geology*, 79(4), 601-637.
doi:10.2113/gsecongeo.79.4.601

- PERKINS, W. G. (1996). A study of the nature, timing, and processes in the Mount Isa lead-zinc orebodies; their relationship to adjacent copper ore-bodies and the lead-zinc systems at McArthur River, Hilton, and Mount Novit., James Cook University of North Queensland,
- PERKINS, W. G. (1997). Mount Isa lead-zinc orebodies: Replacement lodes in a zoned syndeformational copper-lead-zinc system? *Ore Geology Reviews*, 12(2), 61-110. doi:10.1016/S0169-1368(97)00004-8
- SAHA, D., & Tripathy, V. (2012). Tuff beds in Kurnool subbasin, southern India and implications for felsic volcanism in Proterozoic intracratonic basins. *Geoscience Frontiers*, 3(4), 429-444. doi:10.1016/j.gsf.2012.01.002
- SCOTT, D. L., Rawlings, D. J., Page, R. W., Tarlowski, C. Z., Idnurm, M., Jackson, M. J., & Southgate, P. N. (2000). Basement framework and geodynamic evolution of the Palaeoproterozoic superbasins of north-central Australia: An integrated review of geochemical, geochronological and geophysical data. *Australian Journal of Earth Sciences*, 47, 341-380.
- STANTON, R. L. (1962). Elemental constitution of the Black Star orebodies, Mount Isa, Queensland and its interpretation (Vol. 72): *Inst. Mining Metallurgy Trans.*
- STANTON, R. L. (1963). Constitutional features of the Mount Isa sulphide ores and their interpretation (Vol. 205): *Proc. Australas. Instn. Min. Metall.*
- TAYLOR, R., & Lilly, R. (2016). Is Mount Isa a zoned carbonate replacement system? Internal Company Report. Mount Isa Mines.
- ZOU, J., Tian, H., & Tian, L. (2016). Geochemistry and Mineralogy of Tuff in Zhongliangshan Mine, Chongqing, Southwestern China. *Minerals*, 6(47). doi:10.3390/min6020047

APPENDIX A: INSTRUMENT PARAMETERS

Minalyze

Please find the link to the Minalyze website for further information regarding the new innovative technology.

<https://minalyze.com/v>

SEM








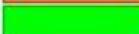
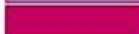











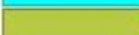
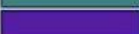
<i>Parameter</i>	<i>Specification</i>
<i>Acc</i>	25Kv
<i>Beam current</i>	40Na
<i>Spot size</i>	6.5
<i>Working distance</i>	10mm.

LA-ICP-MS

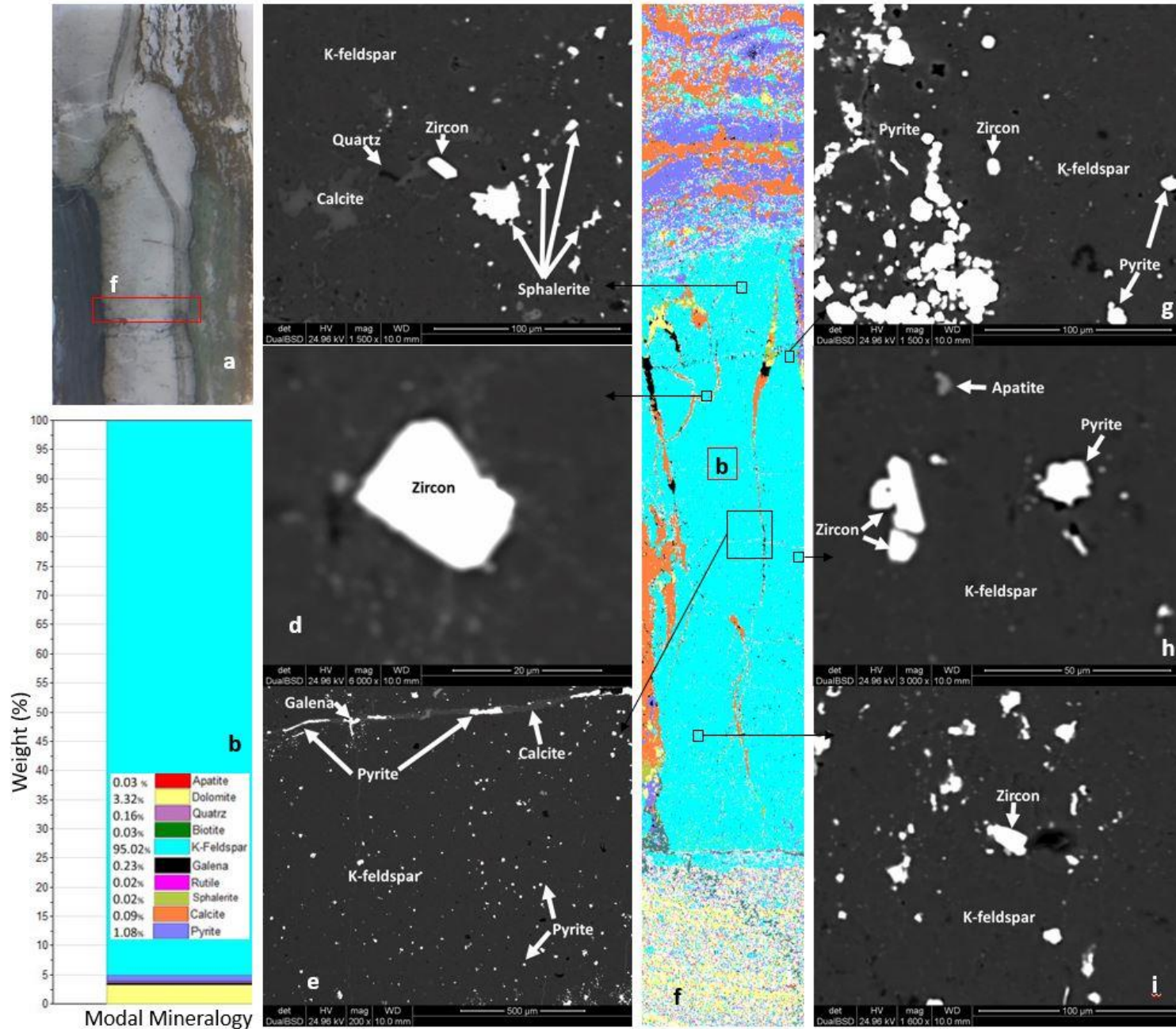
	<i>Monazites</i>	<i>Zircons</i>
<i>Brand and Model</i>	Aglient 7700x ICP-MS	Aglient 7700x ICP-MS
<i>Spot Size</i>	13 μm	19μm
<i>Laser Energy</i>	38mJ	38mJ
<i>Repetition Rate</i>	5Hz	5Hz
<i>Laser Fluence</i>	~2J/cm ²	~2J/cm ²
<i>Atmosphere</i>	He	He
<i>Atmosphere Flow rate</i>	0.35L/min	0.35L/min
<i>Carrier Gas</i>	Ar	Ar
<i>Carrier Gas Flow rate</i>	1.06L/min	1.06L/min
<i>Laser warm up</i>	30s	30s
<i>(Background)</i>		
<i>Data acquisition protocol</i>	Time-resolved analysis	Time-resolved analysis
<i>Background collection</i>	30s	30s
<i>Ablation time</i>	30s	30s
Standardisation and Data Reduction		
<i>Primary Standard</i>	MAdel	GJ1
<i>Secondary Standards</i>	Ambat, 222	91500, Plesovice
<i>Elements Included in Analysis</i>	29Si, 31P, 39K, 139La, 140Ce, 202Hg, 204Pb, 206Pb, 207Pb, 208Pb, 232Th, 238U.	90Zr, 202Hg, 204Pb, 206Pb, 207Pb, 208Pb, 232Th, 238U.

APPENDIX B: OPTICAL AND SEM/MLA PETROLOGY COMPOSITE IMAGES

MLA MAP LEGEND

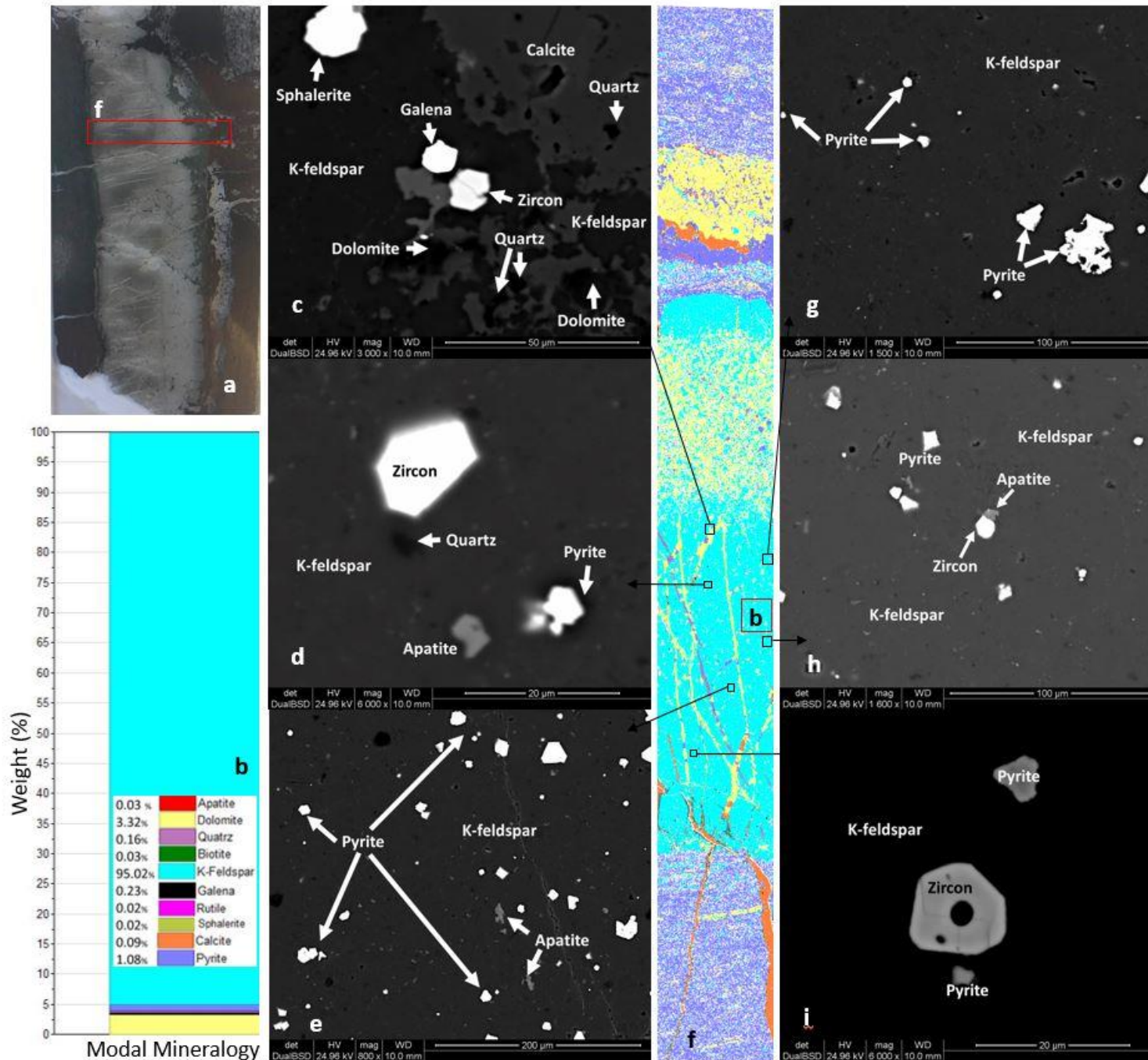
 Unknown	 Low_Counts	 No_XRay]
 Fluorite	 Calcite	 Quatz	
 Rutile	 Thorite	 Zircon	
 Albite	 Chalcopryite	 Arsenopyrite	
 Apatite	 Dolomite	 Galena	
 Biotite	 Pyrite	 K-Feldspar	
 Chlorite	 Muscovite	 Sphalerite	
 Ankerite			

Sample GFM-0.29



(a) Thin section GFM-0.29 showing a deformed light coloured layer with a preferentially altered/precipitated layer of fine-grained Pyrite-2 within, highlighting the appearance of soft sediment-deformation. The surrounding layers are heavily pyrrhoite mineralised. (b) Modal mineralogy obtained from area indicated by red box on figure f. The STM groundmass is clearly K-feldspar dominant, with only very minor accessories of pyrite, dolomite, calcite and galena, which are believed to be over-printing the fine-mat of K-feldspar crystals. (c) The fine k-feldspar matrix is too hard to see individual crystal shapes, however, calcite and quartz appear as infill textures. Euhedral zircon is identified, indicating igneous origin. Calcite is observed as infill surrounding the zircon grain. Pyrite-2 and sphalerite overprint the K-feldspar groundmass. (d) Close up image of euhedral zircon (~20µm). (e) Very fine-grained K-feldspar matrix, with heterogeneous distribution of Pyrite-2 within the STMB. A calcite vein runs through the layer, infilled also by galena, sphalerite, Pyrite-2 and fluorite. (f) MLA map represents striking contrast of the STMB K-feldspar groundmass with the surrounding lithology. (g) Fine-grained Pyrite-1 layer within the STMB is heterogeneous replacement of existing layer-appearing to have been introduced post-deposition and soft and brittle deformation (infilling stylolite structures as well). (h) Three euhedral zircons in close spatial proximity within the fine K-feldspar groundmass. Pyrite-2 and apatite appear as infill texture. (i) Euhedral zircon imbedded in the K-feldspar groundmass and surrounded by fine-grained Pyrite-2.

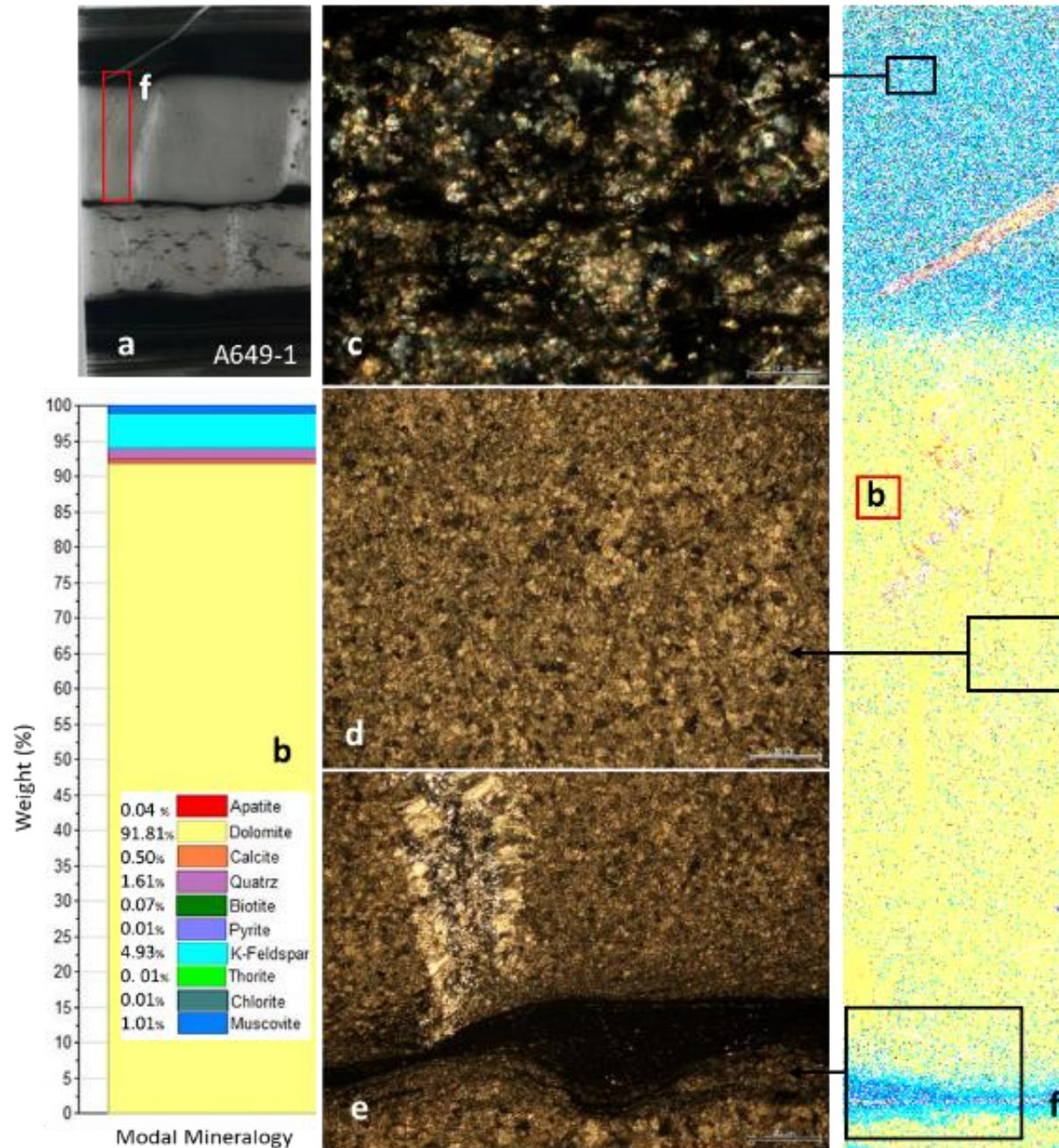
Sample GFM-29



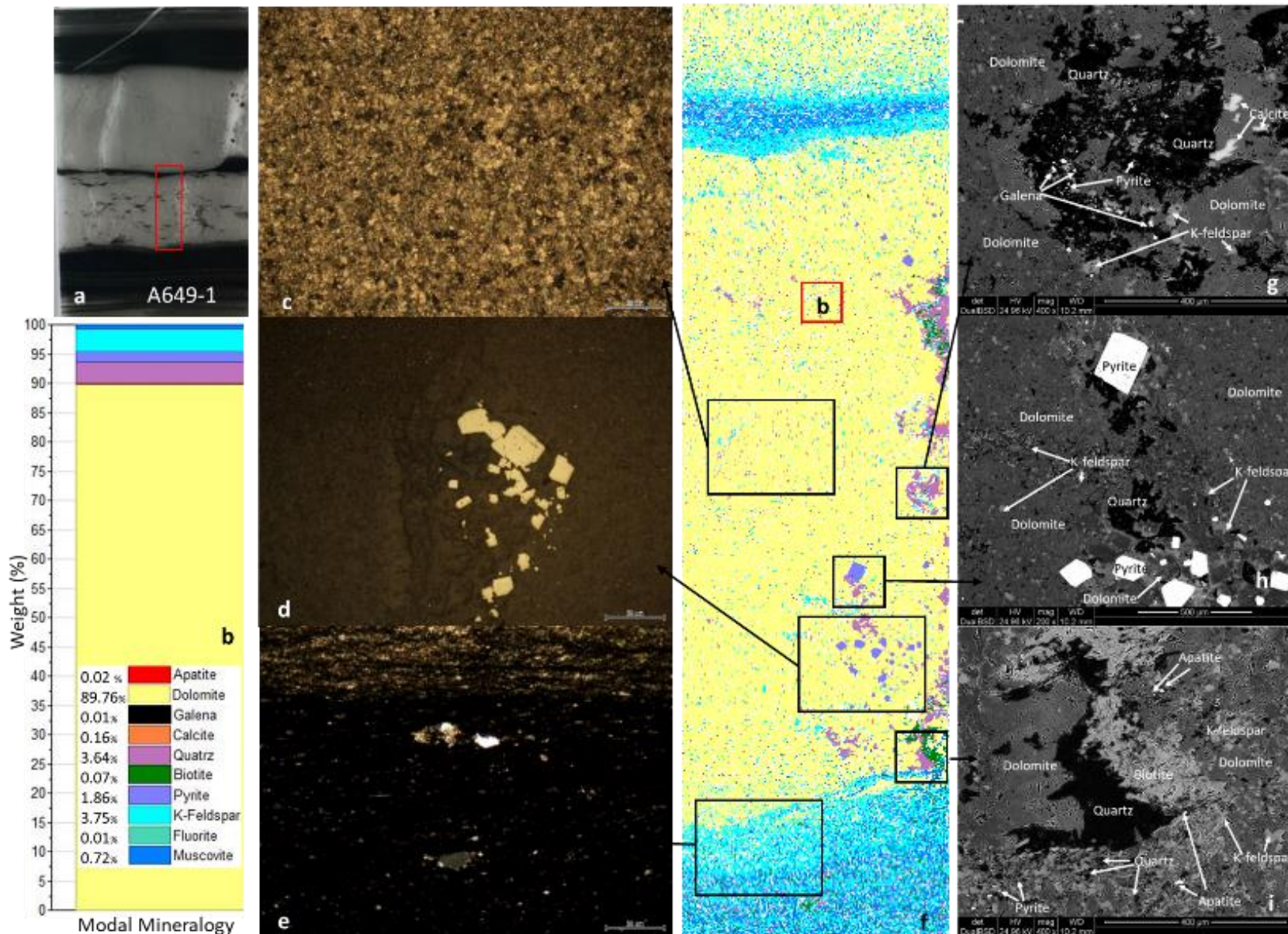
(a) Thin section GFM-29 appears to have compositional grading from light to dark mineralogy. This is due to the disseminated dolomite overprinting the STMB. Cross-fractures are hard to distinguish, as network veins are extensive through the layer. (b) modal mineralogy is dominantly K-feldspar rich with minor accessory dolomite, pyrite and galena (sample area indicted by red box on figure f). (c) Euhedral-subhedral zircon outside dolomitic vein with some infill of dolomite and quartz surrounding the grain. Calcite and dolomite vein infill is starkly contrasted by K-feldspar groundmass. Galena and sphalerite are also present as subhedral grains. (d) Euhedral zircon contrasted by the K-feldspar groundmass, along with Pyrite-2. (e) Anhedral apatite grains appearing as infill texture amongst the fine-grained K-feldspar matrix, and Pyrite-2 euhedral grains. (f) The STMB is starkly more fine-grained and K-feldspar dominant than surrounding layers, and the dolomitic disseminated layer appears to originate from vein fluids, therefore overprinting or later altering the K-feldspar groundmass. (g) More fine grains of Pyrite-2 over printing K-feldspar groundmass. (h) Subhedral zircon with apatite appearing to infill around the grain. There is one straight edge of the zircon preserved, indicating if it was of ash-fall derivation, it has had some detrital influences. (i) Sub-rounded zircon starkly contrasted by K-feldspar groundmass.

A649-1 (Map 1)

Gabrielle Redden
TMBs at MICO & GFM

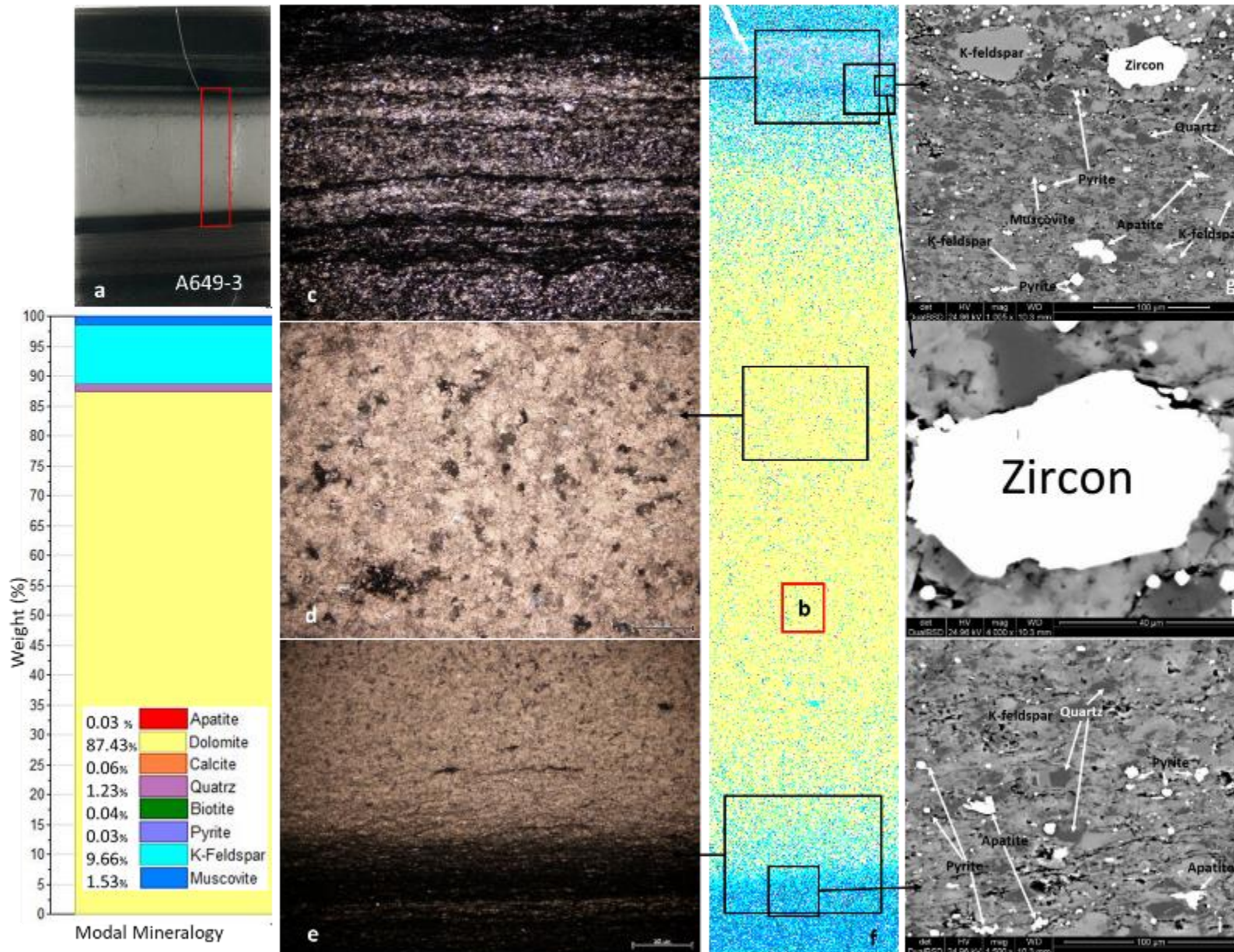


A649-1 Map 2



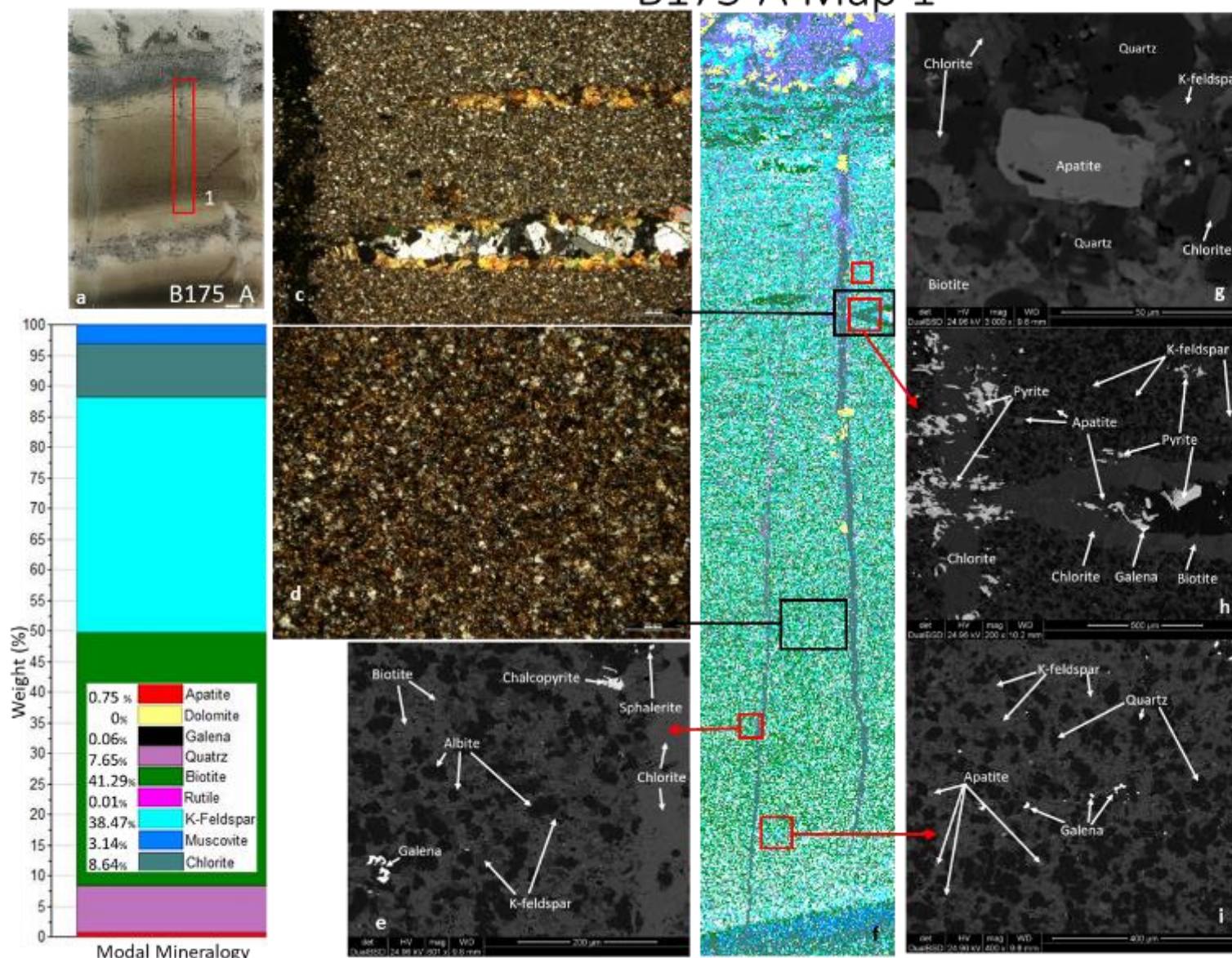
(a) Thin section A649-1 capturing two suspected TMBs (light coloured layers) and the red box indicating the area mapped by MLA (Figure f). (b) Modal mineralogy obtained from area indicated in red box on figure f. Dominantly carbonaceous groundmass of the STMB. (c) Very fine groundmass of dolomite, with fine flecks of quartz and K-feldspar. (d) Reflected light image showing coarse grained pyrite within the fine grained groundmass and quartz associated vein. (e) The fine grained dolomite groundmass gradually transitions to K Feldspar dominated very fine grained layers with small inclusions of quartz and pyrite. (f) MLA map of the suspected TMB indicated in Figure 1. The yellow layer is indicated as dolomite, with little-no variation in grain size from the base of the layer to the top. Flecks of quartz and k feldspar are dotted throughout the layer in no particular orientation or spatial distribution. To the right of the map a network of disseminated veins, hosting mainly quartz with some biotite, k-feldspar, calcite and mineralisation of coarse grained pyrite. No zircons were identified within this layer, suggesting it is not a TMB, OR, too distal for zircons to have been deposited. The layer is bound by coarse grained k-feldspar bands with muscovite and quartz. (g) The dolomite groundmass with k-feldspar inclusions is overprinted by vein infill of quartz, calcite, and mineralisation of pyrite and galena. Mineralisation appears to overprint quartz infill, indicating later precipitation. (h) Dolomite groundmass, overprinted by coarse grained k-feldspar from vein network, including quartz, coarser grained dolomite and pyrite. (i) Quartz and biotite give the appearance of twinning, but are closely associated within the vein infill. The vein appears to stem from the k feldspar rich layer below, where apatite forms within the k-feldspar and quartz rich matrix, along with small grains of pyrite

A649-3



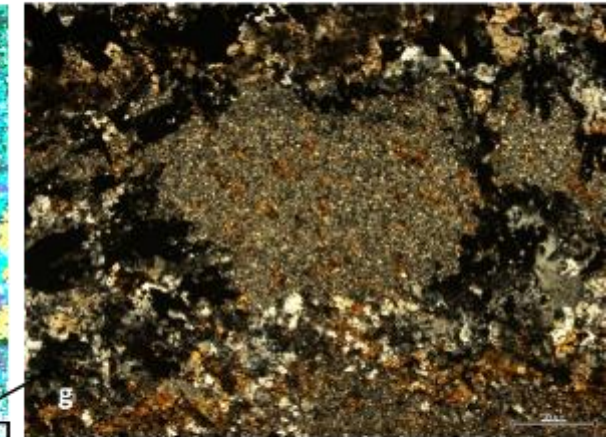
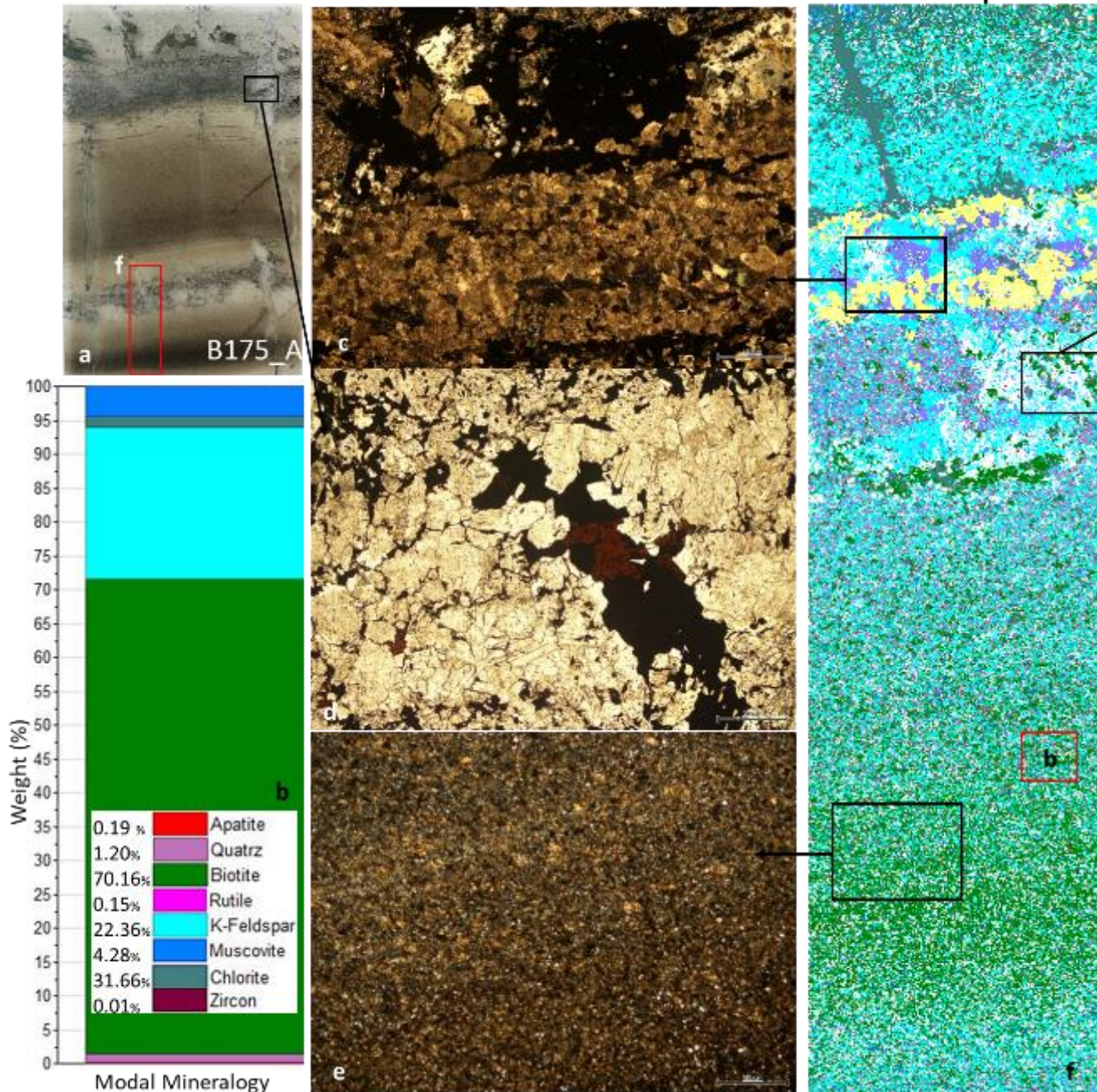
(a) Thin section A649.3 has one main suspected TMB with fine vein or cross fracture cross-cutting entire bed and terminating at the boundaries. Light coloured groundmass with boundaries defined by finely bedded dark layers. (b) Modal mineralogy of groundmass A649.3 is dominantly carbonaceous (dolomitic) with integration of K-feldspar and quartz. (c) Interbedded light and dark groundmass with some pyrite (opaque) mineralisation. XPL image. (d) Light coloured groundmass inside suspected TMB, found to be dolomite with specks of quartz and k feldspar. (e) The contact between the suspected TMB and the finely bedded dark layers shows a gradual increase in k-feldspar grains. (f) Composition of the suspected TMB is mainly dolomitic (yellow) with speckles of K-feldspar (light blue) included in the fine and inter-grown groundmass. At both the upper and lower boundaries k-feldspar abundance increases towards heavily k feldspar, muscovite (dark blue) and/or sericite finely bedded layers. These layers are then interrupted by some fine grained pyrite layers (purple). In this case, the K-feldspar peaks identified by Minalyzer data refer to the highly potassic layers either side of this dolomitic bed. (g) In the k-feldspar rich finely bedded layer there are inclusions of pyrite throughout, and heavier bands of fine grained pyrite too. K-feldspar is found as small intergrowths that make up the fine groundmass and as euhedral subhedral grain inclusions. Sub-Anhedral apatites exist within this fine grained matrix of k-feldspar, quartz and muscovite. Zircon is rare, however, pictured is a euhedral-subhedral grain. (h) Close up image of zircon outside of suspected TMB. The euhedral-subhedral grain is approx. 5 microns wide, possible to obtain date using laser ablation. (i) Transition zone from dolomite layer to fine grained k feldspar, quartz and muscovite layer. Inclusions of pyrite and apatite is common.

B175-A Map 1



(a) Thin section B175-A, showing Map 1 in red. Map 1 captures the top suspected tmb, which appears to show compositional grading from the base of the tmb to the top, where the bed is cut-off by heavy mineralisation. Green coloured composition suggests biotite dominated. Several veins cross-cutting this bed, however only one appears to terminate at the tmb boundaries, giving the appearance of a 'cross-fracture'. (b) Modal mineralogy shows K-feldspar is moderately enriched with significant biotite groundmass composition. (c) Horizontal vein with K-feldspar showing simple twinning, rimmed with biotite and with inclusions of pyrite. Vertical chlorite vein with pyrrhotite mineralisation on rims, cross-cutting the fine grained groundmass. (d) Fine grained groundmass of biotite with quartz and k-feldspar. (e) Chlorite vein cross-cutting fine grained groundmass of biotite, k-feldspar, albite (and quartz) and scatterings of sphalerite, chalcopyrite and galena within the groundmass/outside of the vein. (f) The compositional grading seen in this section is observed to be the increase and decrease in biotite abundance from top-bottom. K. feldspar is present throughout entire bed, but is more pervasive at the top of the layer, where biotite is not. (g) Anhedral Biotite with overprinting euhedral-subhedral quartz, k-feldspar, chlorite and apatite grains. (h) Chlorite and biotite rimmed horizontal vein extending off the dominantly chlorite infilled vertical cross-cutting vein. The horizontal vein is infilled with k-feldspar, galena, pyrite/or pyrrhotite and apatite. Pyrrhotite/or pyrite overprints the chlorite vertical vein. (i) Fine grained groundmass of k-feldspar, quartz and/or albite, and with biotite too anhedral to identify individual grains. Galena is found dotted throughout groundmass.

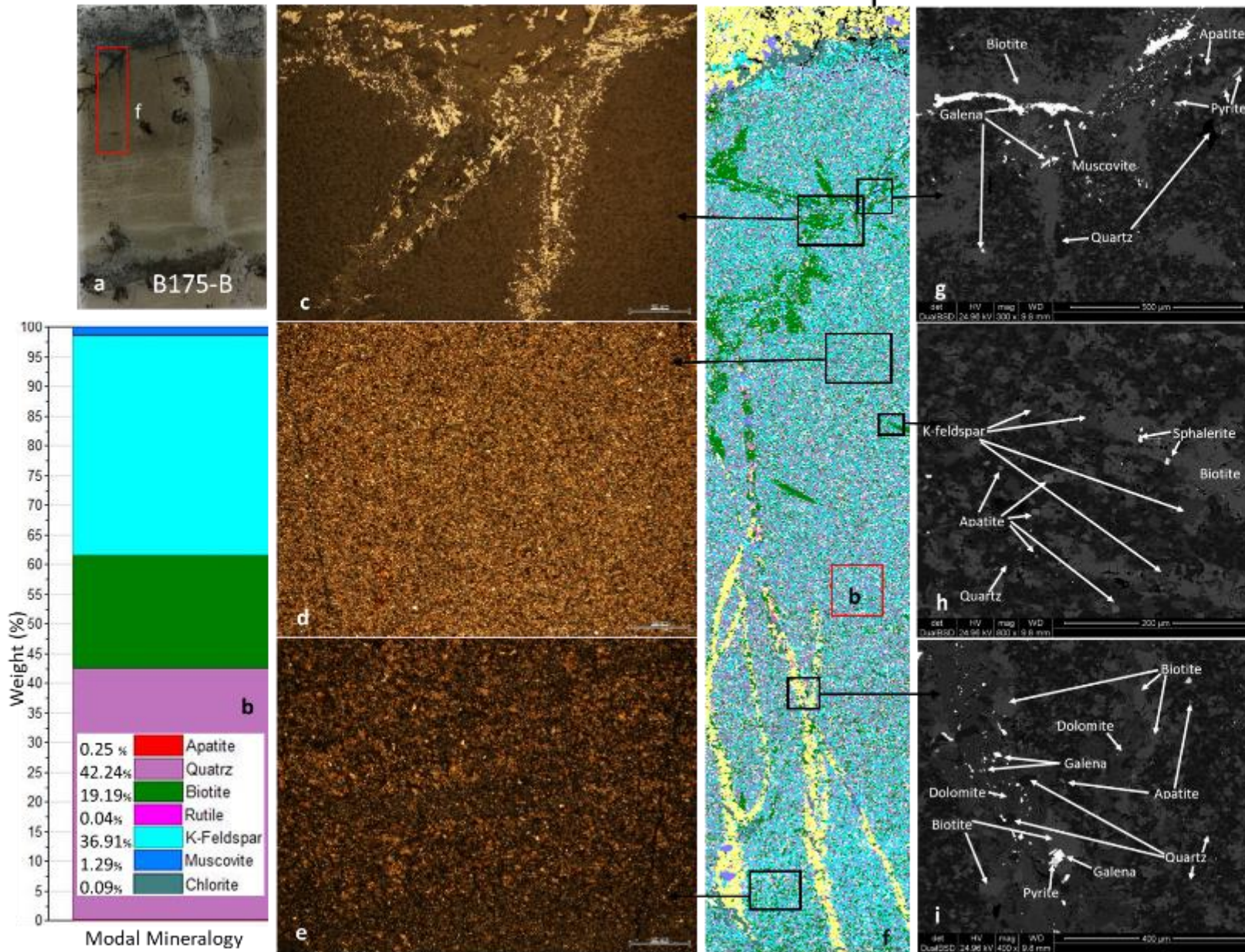
B175-A Map 2



(a) Thin section B175-A Map 2 captures the second suspected tmb in this thin section, however, cuts off the base. A lateral vein with heavy/coarse k-feldspar grains separates the two tmb's. Similar groundmass grading of biotite is observed here and Map 1. (b) Modal mineralogy shows layer is also biotite dominant with significant K feldspar composition. (c) The band separating the two tmb's appears to be a vein with coarse grained k-feldspar, with pyrrhotite mineralisation throughout. (d) Rutile within/overprinting pyrrhotite. High relief, brown/reddish in ppl, and isotropic in xpl, grey in reflected light. Formed within wider cross-cutting vein of calcite and a layer enriched in pyrrhotite mineralisation. (e) Fine grained groundmass of very fine biotite with k feldspar and quartz included in the matrix. Biotite abundance increases from the base and decreases towards the top/boundary with the vein (f) Distinctive biotite (green) grading, increasing in abundance from the base of the sample, and decreasing towards the contact with the upper mineralised and k-feldspar and dolomite vein. Chlorite appears along the upper edge of the dolomite, forming the vein that cross-cuts the upper tmb. There is a thick biotite patch that forms part of the upper boundary of the tmb. Large difference in k feldspar grain size from the fine grained groundmass to the coarse grained horizontal band/vein. Potentially two different processes of formation. A small zircon can be identified within the area of (c), which will be investigated further into this thesis. (g). A patch of fine grained groundmass in the middle that has not been overprinted and is preserved within the mineralised and k feldspar rich band. Dark is pyrrhotite and surrounding minerals include quartz and biotite.

B175-B Map 1

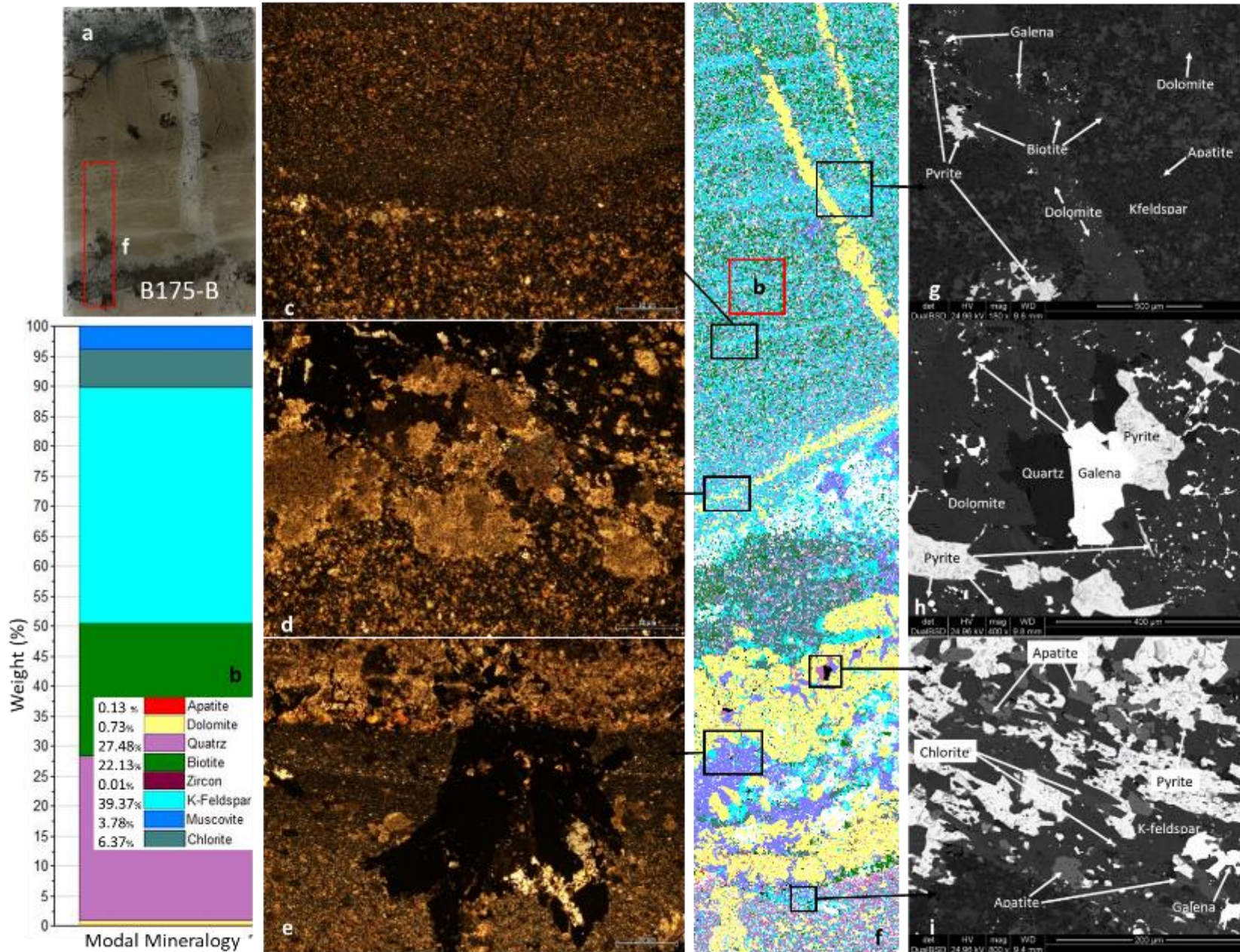
Gabrielle Redden
TMBs at MICO & GFM



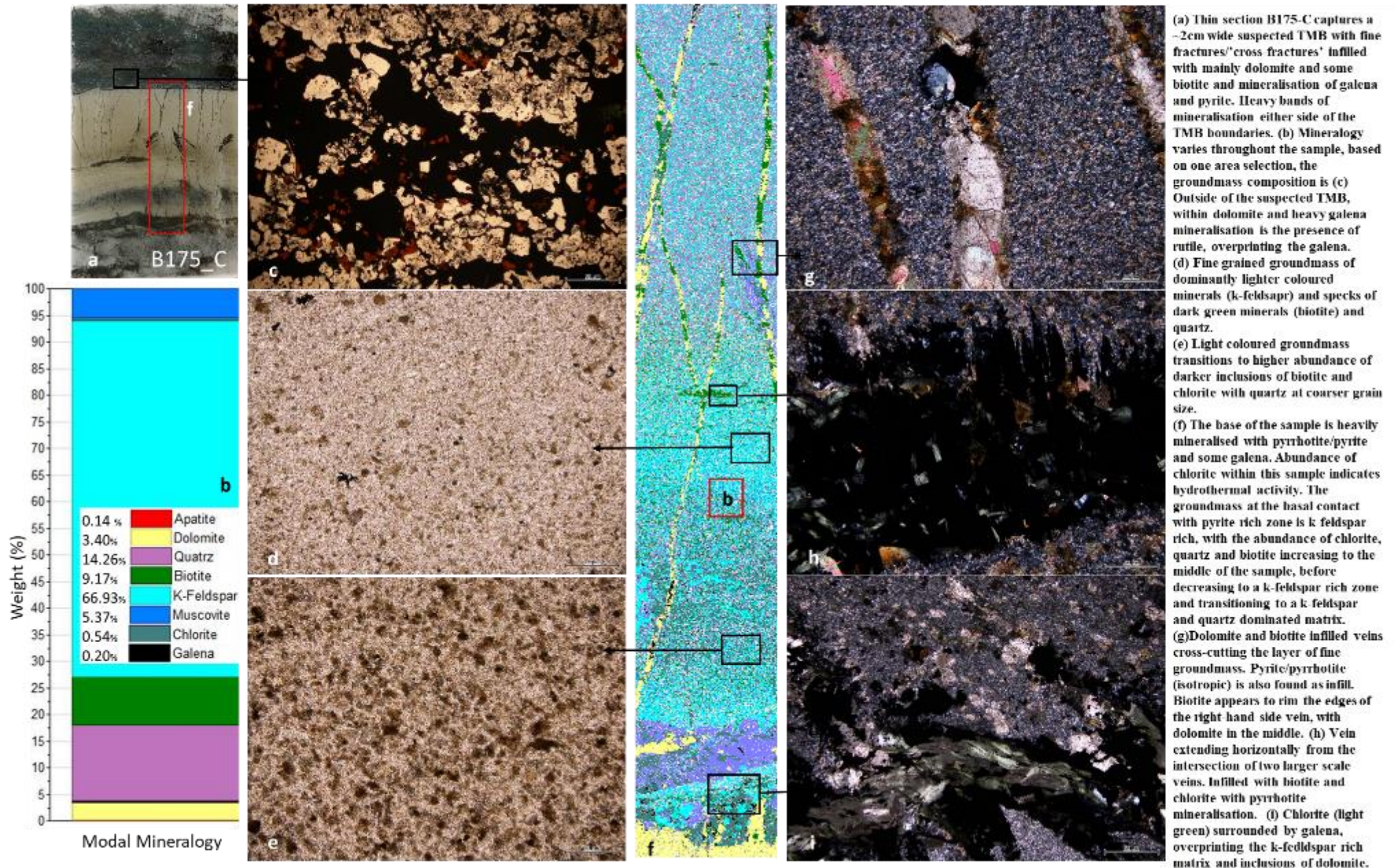
(a) Thin section B175-B Map 1 captures the top half of a ~2.5cm thick suspected TMB. The appearance of compositional grading is a point of interest. The entire bed is cross-cut by a 2mm wide vein that offsets the layer boundaries. Heavy mineralisation occurs along and within veins at the layer boundaries. (b) Modal mineralogy indicates dominantly quartz and K-feldspar with a lesser degree of biotite composition. (c) Vein stemming off the upper mineralised zone of the thin section, dominated by galena and some pyrrhotite with biotite infill. (Reflected light image). (d) Very fine grained groundmass of composition too fine to see under microscope, but containing biotite, k-feldspar and quartz. (XPL). (e) The groundmass lower down in the sample, appears to contain more dark minerals in XPL which is k-feldspar. (f) The groundmass at the base of the map is more k-feldspar dominated with biotite bands interchanging. The sample progresses to k-feldspar and quartz dominated, with biotite dispersed throughout. Dolomite veins at the base of the sample transition to biotite dominated veins with comparatively more galena mineralisation. Biotite sub veins also occur within the top half of the sample, overprinting the fine groundmass. (g) Biotite vein with galena infill and some pyrite/pyrrhotite mineralisation. Overprinting the k-feldspar, quartz and biotite groundmass. Muscovite is also associated with vein infill and some apatite grains have been identified. (h) Fine grained groundmass of biotite, quartz and k-feldspar overprinted by later stage biotite vein infill. Sphalerite found as vein infill and apatite found within groundmass. (i) Fine biotite and quartz matrix overprinted by dolomite and biotite infilled vein. Biotite within vein are coarser and have more defined grain shape. Galena and pyrite disseminated throughout vein.

B175-B Map 2

Gabrielle Redden
TMBs at MICO & GFM



B175-C



APPENDIX C: MINALYZE DATA

Minalyze Data correlation coefficients between Oxides and Zirconium

	K₂O vs. SiO₂	K₂O vs. TiO₂	K₂O vs. CaO	K₂O vs. Zr	SiO₂ vs. TiO₂	SiO₂ vs. CaO	SiO₂ vs. Zr	TiO₂ vs. CaO	TiO₂ vs. Zr	CaO vs. Zr
A649	0.8399	0.7928	-0.8639	0.8328	0.8381	0.9086	0.5491	0.7828	0.597	0.5997
A826	0.8794	0.4062	-0.5128	0.6405	0.4062	0.3222	0.4095	0.3955	0.8472	0.366
B175	0.585	0.7179	-0.7461	0.5969	0.318	0.2517	0.2962	0.5795	0.8335	0.3747
GFM-0.29	0.9972	0.6497	-0.6703	0.9663	0.6089	0.6356	0.9592	0.9854	0.5622	0.5565
GFM-13	0.8514	0.6216	-0.1469	0.3916	0.4453	0.1595	0.2151	0.00	0.9064	0.0279
GFM-29	0.0812	0.9303	-0.1051	0.9558	0.0706	0.0052	0.0564	0.2074	0.8797	0.0889

Gabrielle Redden
TMBs at MICO & GFM

	Sample	From	To	Al2O3%	SiO2%	S ppm	K2O%	CaO%	TiO2%	V ppm	Cr ppm	MnO%	Fe2O3%	Ni ppm	Cu ppm	Zn ppm	Ga ppm	As ppm	Rb ppm	Sr ppm	Y ppm	Zr ppm	Nb ppm	Ba ppm	Pb ppm	
MICO A649	2012113002	649.02	649.03	BDL	63.83	49402	11.51	3.87	0.4647	94.78	ND	0.0827	7.4783	0	0	0	0	184.21	168.48	0	0	432.97	BDL	918.81	0	
	2012113002	649.03	649.04	14.13	69.08	32397	11.59	6.63	0.4952	39	ND	0.1533	6.5953	29.39	25.22	11.2	13.45	157.66	190.17	0	31.59	409.34	BDL	1992.34	0	
	2012113002	649.04	649.05	BDL	50.36	4735	9.16	18.67	0.4672	65.85	ND	0.4661	6.8195	40.41	36.33	0	21.62	0	221.95	34.05	0	402.52	BDL	1832.57	0	
	2012113002	649.05	649.06	BDL	35.04	1815	5.71	28.97	0.3188	0	ND	0.8597	10.0585	37.42	33.05	0	17.22	0	164.07	39.43	0	264.57	BDL	883.47	0	
	2012113002	649.06	649.07	7.40	26.44	BDL	3.35	37.07	0.1945	0	BDL	1.1123	12.0541	34.77	33.91	0	0	0	109.96	65.75	0	135.15	BDL	390.11	80.25	
	2012113002	649.07	649.08	6.69	34.92	14159	3.38	37.77	0.2601	41.56	ND	0.8906	12.2189	31.44	0	82.42	0	128.86	113.93	55.24	0	103.9	BDL	599.7	1254.53	
	2012113002	649.08	649.09	BDL	43.16	28615	5.74	22.37	0.478	67.45	BDL	0.5933	12.1308	36.91	33.19	0	17.16	211.07	177.07	26.06	0	216.09	BDL	804.57	78.83	
	2012113002	649.09	649.1	15.68	63.99	33277	8.44	12.01	0.5751	63.94	BDL	0.2572	8.7981	32.12	49.43	0	22.37	206.09	217.66	0	0	221.83	BDL	1575.46	0	
	2012113002	649.1	649.11	11.09	48.89	16341	6.58	22.67	0.5091	43.48	BDL	0.5052	9.7721	34.68	52.57	16.1	26.9	175.04	198.33	34.91	0	252.28	BDL	1220.69	78.27	
	2012113002	649.11	649.12	9.45	41.14	7240	5.33	28.67	0.4159	0	BDL	0.7364	9.8768	32.12	0	0	0	75.94	176.42	40.91	0	193.38	BDL	865.59	0	
	2012113002	649.12	649.13	11.02	43.46	17775	5.37	27.83	0.4079	52.27	BDL	0.6406	10.4331	35.11	0	0	0	176.97	179.32	38.22	0	181.23	BDL	832.78	172.98	
	2012113002	649.13	649.14	9.70	61.30	47638	7.61	12.55	0.4944	64.89	BDL	0.296	10.2175	34.17	31.06	17.62	18.16	229.41	185.98	25.8	0	220.36	BDL	1207.52	204.32	
	2012113002	649.14	649.15	12.14	66.40	40506	9.12	6.04	0.5947	81.52	ND	0.1735	8.444	30.24	49.86	18.35	23.51	279.13	218.62	20.84	0	240.39	BDL	1502.92	80.68	
	2012113002	649.15	649.16	3.79	63.96	31825	8.37	8.47	0.5672	81.04	BDL	0.2354	8.0277	33.15	50.15	74.37	25.01	952.57	224.53	29.1	44.33	265.23	BDL	1429.07	366.66	
	2012113002	649.16	649.17	BDL	63.31	20621	8.87	7.42	0.5941	91.75	ND	0.2121	7.1536	34.94	48.86	12.72	19.17	187.26	221.2	0	0	263.23	BDL	1575.68	155.54	
	2012113002	649.17	649.18	12.42	61.97	10193	7.37	15.85	0.5272	66.17	BDL	0.362	6.9269	36.14	50.43	21.34	21.24	146.56	205.31	25.8	0	225.17	BDL	1117.1	138.81	
	2012113002	649.18	649.19	10.01	42.70	8409	5.02	25.13	0.3793	45.39	ND	0.6833	9.2468	39.38	43.88	0	17.79	130.8	163.22	35.09	0	186.84	BDL	898.51	164.19	
	2012113002	649.19	649.2	8.12	39.92	25755	3.60	32.45	0.305	46.51	BDL	0.8198	11.2178	31.69	0	49.88	0	68.7	113.07	51.07	0	137.16	BDL	582.36	601.89	
	2012113002	649.2	649.21	BDL	20.50	8399	2.75	35.55	0.1958	0	BDL	1.2805	14.2797	41.35	34.48	59.45	0	95.72	87.94	52.81	0	118.73	BDL	530.13	283.15	
	2012113002	649.21	649.22	BDL	15.03	1431	2.10	38.70	0.1584	0	BDL	1.4534	14.7175	36.05	0	37.61	0	0	66.15	54.37	0	97.89	BDL	383.63	357.02	
	2012113002	649.22	649.23	BDL	25.99	9852	3.27	34.17	0.2825	0	BDL	1.1075	13.6552	34.26	0	32.37	0	112.13	117.69	42.12	0	150.11	BDL	799.75	366.8	
	2012113002	649.23	649.24	10.00	48.68	22258	5.91	23.00	0.438	51.79	ND	0.5714	10.6128	29.3	45.59	13.4	17.35	178.9	172.02	26.66	0	201.13	BDL	1187.11	171.85	
	2012113002	649.24	649.25	BDL	21.73	BDL	2.54	36.18	0.2309	0	BDL	1.3292	14.042	39.81	0	0	0	0	82.79	74.43	0	0	128.74	BDL	0	0
	2012113002	649.25	649.26	5.02	22.07	6307	1.92	39.16	0.1355	0	BDL	1.3459	14.3797	41.26	0	23.81	0	108.75	38.01	66.44	0	77.33	BDL	0	200.49	
	2012113002	649.26	649.27	BDL	23.68	7099	3.04	34.77	0.2755	0	BDL	1.2018	14.4482	34.17	37.33	BDL	0	148.49	117.26	57.15	47.7	154.65	BDL	738.4	0	
	2012113002	649.27	649.28	BDL	43.78	18187	4.96	25.68	0.4001	36.28	BDL	0.6973	11.3556	33.92	0	33.72	0	153.32	149.69	36.3	0	197.26	BDL	940.1	347.66	
	2012113002	649.28	649.29	6.77	60.04	24585	7.23	15.45	0.5432	84.71	ND	0.3841	8.9034	33.66	0	32.54	21.68	194.83	212.61	28.49	0	252.95	BDL	1223.76	159.37	
	2012113002	649.29	649.3	12.17	64.77	21912	7.59	13.64	0.5308	88.23	BDL	0.3128	7.9465	34.17	51.29	15.03	25.33	172.3	204.34	17.11	0	234.38	BDL	1213.55	0	
	2012113002	649.3	649.31	8.59	45.03	7285	5.02	25.80	0.4487	49.71	BDL	0.6649	9.2896	32.29	44.73	0	19.92	107.47	191.67	41.6	0	216.09	BDL	560.3	0	
	2012113002	649.31	649.32	7.35	31.14	2803	2.94	33.78	0.3012	0	BDL	1.0244	11.7859	32.21	39.75	0	16.4	76.74	129.61	59.67	0	166.14	BDL	579.95	0	
	2012113002	649.32	649.33	BDL	15.33	BDL	1.22	39.69	0.0973	0	BDL	1.4815	15.4244	38.1	39.6	0	0	105.22	57.02	53.76	0	65.97	BDL	0	0	
	2012113002	649.33	649.34	4.89	12.57	BDL	0.58	41.37	0.0145	0	BDL	1.6278	16.3536	30.5	0	0	0	0	0	64.01	0	0	BDL	0	112.3	
	2012113002	649.34	649.35	6.55	23.69	17388	1.59	37.52	0.1164	0	BDL	1.23	16.5352	32.72	0	0	0	214.94	27.6	42.04	0	56.23	BDL	0	0	
	2012113002	649.35	649.36	BDL	41.34	53877	4.10	27.17	0.3061	0	BDL	0.7179	17.7304	35.37	0	0	0	361.66	87.84	36.83	0	143.97	BDL	836.84	91.17	
	2012113002	649.36	649.37	BDL	57.31	68949	7.36	13.02	0.482	73.05	ND	0.2983	14.5487	32.63	37.18	18.35	11.38	369.7	155.38	21.71	0	221.16	BDL	1198.3	110.17	
	2012113002	649.37	649.38	10.88	67.85	52406	8.81	6.43	0.5153	82.32	BDL	0.1787	10.4534	33.06	42.03	13.91	18.98	299.08	162.68	20.5	0	239.59	BDL	1453.76	76.42	
	2012113002	649.38	649.39	BDL	53.33	34129	7.34	15.08	0.4686	83.92	BDL	0.4269	9.91	38.7	31.91	103.87	17.79	205.44	194.46	29.7	0	197.79	BDL	1211.58	292.37	
	2012113002	649.39	649.4	12.35	55.47	16851	7.01	17.03	0.4508	81.36	BDL	0.4755	8.2731	31.35	26.36	65.65	11.12	168.76	171.16	23.97	0	186.3	BDL	914.31	100.24	
	2012113002	649.4	649.41	BDL	47.93	11751	6.26	19.60	0.4669	74.64	BDL	0.5929	8.8711	32.12	36.47	0	18.54	156.54	191.89	35.09	0	195.39	BDL	1279.72	0	
	2012113002	649.41	649.42	10.11	52.09	17330	5.21	22.54	0.3545	69.37	ND	0.6964	9.0491	38.44	35.05	26.35	0	127.58	140.34	30.92	0	147.71	BDL	808.3	84.79	
	2012113002	649.42	649.43	7.16	46.37	13240	4.42	23.21	0.2933	45.23	ND	0.8087	9.3566	36.31	37.33	0	0	116.48	132.08	40.99	0	136.76	BDL	611.11	0	
	2012113002	649.43	649.44	BDL	42.01	19829	3.75	25.27	0.2245	0	BDL	0.9602	10.8272	31.52	0	14.13	0	125.65	113.82	49.07	0	129.95	BDL	499.84	0	
	2012113002	649.44	649.45	7.43	49.03	12006	4.46	23.00	0.2898	44.44	BDL	0.824	9.1326	34.68	38.32	23.59	0	106.66	110.6	39.26	0	148.64	BDL	559.43	0	
	2012113002	649.45	649.46	BDL	51.83	9327	5.69	18.49	0.43	70.65	BDL	0.6552	7.9989	37.16	36.76	22.75	0	101.68	148.61	32.74	0	214.22	BDL	936.91	0	
	2012113002	649.46	649.47	9.86	63.03	10216	6.99	14.05	0.4874	61.06	BDL	0.4506	6.437	30.93	58.84	47.07	13.58	105.38	178.57	27.18	0	223.7	BDL	1142.45	0	
	2012113002	649.47	649.48	8.20	64.25	10775	7.36	10.38	0.512	85.99	ND	0.3317	5.6259	31.44	52.57	34.62	15.84	83.82	178.78	0	0	220.23	BDL	1356.21	0	
	2012113002	649.48	649.49	7.84	50.46	11361	5.69	8.38	0.4245	58.02	BDL	0.2698	4.6175	24.35	27.5	13.91	9.49	80.44	135.62	18.07	0	217.56	BDL	1048.62	0	

Gabrielle Redden
TMBs at MICO & GFM

MICO A826	2012113002	826.29	826.3	BDL	23.23	114550	3.40	7.75	0.2465	BDL	BDL	0.1676	22.1773	30.07	180.79	271.76	BDL	662.02	76.45	BDL	ND	80.4	BDL	483.49	693.77
	2012113002	826.3	826.31	BDL	31.53	85841	3.95	18.14	0.2611	BDL	BDL	0.3751	21.149	32.63	195.03	224.36	BDL	587.53	105.77	34.48	BDL	92.55	BDL	963.47	576.22
	2012113002	826.31	826.32	6.65	30.57	56775	3.20	23.86	0.2114	BDL	BDL	0.476	18.4818	34.09	141.04	154.21	BDL	509.35	80.32	29.88	BDL	84.27	BDL	757.72	389.63
	2012113002	826.32	826.33	BDL	29.32	61340	3.50	22.49	0.2163	36.12	BDL	0.4932	19.8522	47.67	167.25	167.66	BDL	654.78	95.14	34.48	BDL	88.41	BDL	905.31	326.39
	2012113002	826.33	826.34	BDL	27.02	54602	3.38	24.21	0.2699	BDL	BDL	0.4806	19.4545	41.95	133.06	153.14	BDL	831.75	105.55	45.08	BDL	124.34	BDL	1012.74	454.29
	2012113002	826.34	826.35	BDL	28.49	51496	3.68	25.07	0.2695	33.41	BDL	0.5394	18.4979	32.38	148.45	142.83	BDL	281.86	102.01	48.98	BDL	84.81	BDL	1391.1	352.48
	2012113002	826.35	826.36	6.25	32.99	44186	3.34	24.35	0.2321	BDL	ND	0.5709	16.3083	34.51	150.87	147.17	BDL	170.21	90.73	44.12	BDL	80.26	BDL	1235.28	242.74
	2012113002	826.36	826.37	ND	24.86	12258	1.88	28.64	0.0928	BDL	BDL	0.7841	14.1002	34.68	124.37	127.97	BDL	BDL	51.65	59.75	BDL	44.21	ND	554.71	229.7
	2012113002	826.37	826.38	BDL	25.52	11811	2.00	29.64	0.1217	BDL	BDL	0.7317	13.48	42.8	227.37	163.5	BDL	101.84	46.82	53.94	BDL	54.36	ND	784.27	384.1
	2012113002	826.38	826.39	BDL	18.95	4825	1.52	32.70	0.0961	BDL	BDL	0.7675	13.7187	40.58	178.79	106.29	BDL	77.38	31.68	53.94	BDL	BDL	BDL	691.44	257.06
	2012113002	826.39	826.4	4.08	18.00	3798	1.43	33.83	0.0804	BDL	ND	0.8061	13.5604	22.98	59.55	90.08	BDL	BDL	42.2	45.51	BDL	BDL	BDL	488.43	181.91
	2012113002	826.4	826.41	4.76	22.51	2999	1.90	32.11	0.1126	BDL	BDL	0.7068	12.0993	30.75	49.86	56.69	BDL	97.01	52.29	42.38	42.33	65.97	BDL	698.68	99.25
	2012113002	826.41	826.42	BDL	21.32	7616	2.15	32.12	0.1837	ND	BDL	0.7105	12.536	37.5	75.93	90.08	ND	BDL	67.54	57.67	BDL	68.38	ND	537.26	488.6
	2012113002	826.42	826.43	4.27	16.68	5664	1.65	33.86	0.1327	BDL	BDL	0.7283	13.2062	32.38	66.53	77.81	BDL	119.21	35.43	49.68	BDL	55.02	ND	578.41	117.26
	2012113002	826.43	826.44	ND	13.19	7974	1.90	32.69	0.1752	BDL	ND	0.7501	14.1194	41.86	85.62	102.86	BDL	147.21	44.99	50.11	BDL	76.26	BDL	644.8	154.12
	2012113002	826.44	826.45	ND	18.32	14430	2.41	31.03	0.2282	BDL	BDL	0.6582	13.7155	35.71	143.75	141.76	BDL	132.4	66.9	53.15	BDL	96.16	ND	956.67	587.99
	2012113002	826.45	826.46	3.38	26.41	17858	3.02	28.72	0.2333	BDL	BDL	0.5732	12.4727	37.33	95.17	105.51	BDL	132.73	70.76	49.68	BDL	116.32	BDL	1098.22	205.45
	2012113002	826.46	826.47	6.84	29.78	37042	3.59	21.45	0.2421	26.05	ND	0.407	12.2246	28.11	235.92	148.97	BDL	198.53	81.93	28.31	ND	104.97	BDL	1103.05	447.76
	2012113002	826.48	826.49	BDL	25.56	55792	2.69	30.43	0.3431	49.23	BDL	0.502	22.6994	38.02	112.83	130.84	BDL	398.18	84.29	38.82	BDL	98.29	BDL	826.41	457.12
	2012113002	826.49	826.5	6.68	33.45	47297	3.15	31.83	0.2209	BDL	BDL	0.5102	17.3246	41.01	78.64	71.28	BDL	270.44	66.25	45.34	BDL	72.65	BDL	1032.93	556.94
	2012113002	826.5	826.51	7.31	40.73	54828	4.12	24.80	0.2415	32.77	ND	0.4211	16.372	40.66	92.46	BDL	BDL	397.37	78.49	30.14	BDL	96.96	BDL	1685.85	285.28
	2012113002	826.51	826.52	8.67	45.42	41316	5.00	22.88	0.3114	49.23	ND	0.419	13.656	32.29	55.28	20.21	BDL	217.35	86.87	24.93	BDL	125.54	BDL	1570.74	246.28
	2012113002	826.52	826.53	8.85	50.31	42732	5.93	20.33	0.3225	BDL	ND	0.3926	12.0297	28.96	56.84	24.1	BDL	196.6	85.04	39.08	BDL	134.22	BDL	1990.58	241.46
	2012113002	826.53	826.54	BDL	45.17	30755	6.14	19.68	0.4029	73.85	ND	0.4231	11.9942	33.92	55.13	44.36	BDL	199.01	111.89	39.43	BDL	168.28	BDL	2035.8	183.61
	2012113002	826.54	826.55	10.89	51.39	28701	6.17	19.78	0.363	47.63	ND	0.3955	10.6215	29.9	67.39	18.24	BDL	155.09	98.14	33.7	BDL	145.3	BDL	1755.64	117.12
	2012113002	826.55	826.56	BDL	43.72	30097	6.11	19.86	0.4066	66.81	ND	0.4437	11.7378	32.63	55.13	13.12	BDL	218.8	107.27	32.83	BDL	195.52	BDL	2114.8	91.59
	2012113002	826.56	826.57	BDL	46.55	36452	5.77	20.07	0.333	BDL	ND	0.4673	12.5785	29.64	74.08	31.53	BDL	211.24	103.41	29.18	ND	152.38	BDL	1849.25	110.31
	2012113002	826.57	826.58	7.47	47.93	37112	5.35	21.16	0.2536	BDL	ND	0.5154	12.619	31.1	40.32	16.72	BDL	236.65	79.25	44.99	BDL	111.78	BDL	1547.59	BDL
	2012113002	826.58	826.59	6.81	47.20	38502	5.13	22.01	0.2279	30.69	ND	0.5333	13.289	32.98	69.24	18.18	BDL	243.89	61.85	32.05	ND	99.9	BDL	1282.91	133.99
	2012113002	826.59	826.6	7.82	44.41	58564	4.93	21.71	0.2015	BDL	ND	0.5183	15.8798	30.84	60.4	18.02	BDL	435.18	60.78	30.31	BDL	90.68	BDL	1395.17	240.61
	2012113002	826.6	826.61	6.98	42.24	67007	4.71	21.86	0.2133	BDL	ND	0.5214	17.6676	30.33	82.2	23.14	BDL	471.06	64.21	30.92	BDL	80.93	BDL	1265.57	316.61
	2012113002	826.61	826.62	BDL	36.18	77559	4.73	22.36	0.2682	38.36	BDL	0.5136	21.0636	28.53	107.56	40.14	BDL	651.89	99.97	33.96	BDL	102.7	BDL	1411.41	453.58
	2012113002	826.62	826.63	6.76	40.73	117238	5.27	17.62	0.2662	BDL	BDL	0.3894	23.5917	31.69	90.04	39.3	BDL	757.26	96.53	32.22	BDL	95.49	BDL	1204.78	443.23
	2012113002	826.63	826.64	8.50	40.01	115455	4.91	16.14	0.2841	BDL	BDL	0.3336	22.434	24.86	81.2	30.46	BDL	667.49	80.86	20.58	BDL	116.06	BDL	1129.72	352.06
	2012113002	826.64	826.65	BDL	27.69	91240	4.00	12.43	0.3409	ND	BDL	0.2574	21.2964	31.78	BDL	42.9	BDL	664.92	80.1	BDL	BDL	156.79	BDL	710.09	BDL

Gabrielle Redden
TMBs at MICO & GFM

MICO B175	201208122	175.31	175.32	3.92	14.96	359716	2.54	5.40	0.12	0	71	0.13	57.50	25	157	982	15	2204	0	0	0	0	0	0	0	745
	201208122	175.32	175.33	7.59	17.02	315394	2.07	12.68	0.17	0	74	0.29	52.24	27	165	1714	19	2247	0	0	0	0	0	0	0	753
	201208122	175.33	175.34	5.66	31.72	101035	2.63	23.97	0.20	0	0	0.62	25.07	30	156	846	0	576	42	29	0	89	0	0	440	
	201208122	175.34	175.35	4.33	36.12	35658	2.46	26.01	0.11	38	0	0.72	18.24	35	183	157	0	170	47	35	0	0	0	0	0	
	201208122	175.35	175.36	0.00	32.47	20108	2.31	26.20	0.12	0	0	0.80	16.57	33	108	48	0	68	42	50	0	44	0	0	0	
	201208122	175.36	175.37	0.00	32.61	14578	2.16	27.08	0.11	0	0	0.83	14.88	38	141	32	0	0	50	50	43	55	0	0	0	
	201208122	175.37	175.38	5.74	39.37	7114	2.32	26.46	0.10	0	0	0.77	12.60	28	0	0	0	0	52	39	0	47	0	0	0	
	201208122	175.38	175.39	6.06	39.28	12744	2.24	26.74	0.10	0	0	0.77	12.77	34	41	0	0	0	31	33	42	48	0	0	0	
	201208122	175.39	175.4	6.07	34.81	11563	1.95	29.30	0.08	0	0	0.83	13.15	35	58	121	0	0	38	40	0	53	0	0	0	
	201208122	175.4	175.41	5.20	31.39	22433	1.83	29.85	0.08	0	0	0.87	14.11	36	36	81	0	0	25	37	0	39	0	0	0	
	201208122	175.41	175.42	0.00	28.63	19472	1.75	30.88	0.08	0	0	0.94	14.57	43	59	123	0	0	36	50	53	0	0	0	0	
	201208122	175.42	175.43	0.00	26.87	8680	1.48	33.44	0.07	0	0	0.96	15.04	40	70	260	0	125	27	49	0	0	0	0	0	
	201208122	175.43	175.44	0.00	25.16	19519	1.56	31.05	0.08	0	0	0.96	15.43	42	65	633	19	81	26	50	0	0	0	0	101	
	201208122	175.44	175.45	0.00	22.36	22519	1.75	29.12	0.09	0	0	0.97	15.71	42	89	105	0	0	41	57	0	0	0	0	0	
	201208122	175.45	175.46	0.00	27.70	8822	1.78	29.76	0.09	0	0	0.96	14.74	39	66	27	0	0	43	56	0	44	0	0	0	
	201208122	175.46	175.47	0.00	27.21	6434	1.73	29.79	0.08	0	0	0.95	14.98	37	57	122	0	0	38	57	0	61	0	0	0	
	201208122	175.47	175.48	5.42	29.45	16115	1.74	31.24	0.08	0	0	0.88	15.43	31	104	331	0	0	25	47	0	0	0	0	112	
	201208122	175.48	175.49	0.00	23.95	24926	1.72	31.43	0.10	0	0	0.93	19.19	38	1752	182	0	141	30	40	0	56	0	0	0	
	201208122	175.49	175.5	0.00	20.94	12011	1.71	32.50	0.09	0	0	1.04	18.82	42	102	559	0	77	36	51	0	0	0	0	0	
	201208122	175.5	175.51	0.00	20.98	17667	1.79	30.73	0.09	0	0	0.98	20.25	37	206	621	0	80	46	52	0	0	0	0	525	
	201208122	175.51	175.52	6.54	29.80	49052	3.09	25.55	0.18	0	0	0.68	20.19	35	195	1868	14	167	60	33	0	68	0	0	679	
	201208122	175.52	175.53	0.00	38.18	78224	5.65	15.60	0.28	29	0	0.38	20.08	32	169	1585	20	374	101	0	0	126	0	0	740	
	201208122	175.53	175.54	0.00	36.42	163867	6.09	9.92	0.25	0	0	0.25	29.59	27	189	54	0	959	81	21	0	113	0	0	525	
	201208122	175.54	175.55	0.00	26.46	258490	4.64	8.48	0.25	0	0	0.21	44.11	24	215	124	0	1795	41	0	0	89	0	0	795	
	201208122	175.55	175.56	0.00	31.30	175114	5.51	12.42	0.33	0	49	0.32	31.89	35	113	81	0	1062	86	25	0	153	0	0	570	
	201208122	175.56	175.57	0.00	28.60	170345	5.30	12.59	0.23	0	0	0.31	33.52	26	170	217	0	1193	76	0	0	98	0	0	755	
	201208122	175.57	175.58	3.52	32.44	171921	5.74	9.01	0.30	0	53	0.20	30.63	34	165	252	14	1035	118	30	0	147	0	0	797	
	201208122	175.58	175.59	0.00	49.49	31159	6.27	9.79	0.38	55	0	0.25	9.89	33	125	56	14	101	159	0	0	149	0	249	171	
	201208122	175.59	175.6	9.85	55.88	104892	6.11	5.53	0.22	52	0	0.16	13.21	31	45	42	0	381	83	0	0	71	0	629	171	
	201208122	175.6	175.61	0.00	61.68	112599	7.13	7.16	0.29	50	0	0.22	16.10	36	94	53	15	466	107	0	0	107	0	730	197	
	201208122	175.61	175.62	10.09	70.71	76408	7.42	7.37	0.33	72	0	0.22	11.05	38	71	44	15	278	108	15	0	124	0	757	105	
	201208122	175.62	175.63	9.41	68.15	67962	7.16	8.96	0.34	73	0	0.27	10.82	34	48	60	15	247	105	0	0	139	0	694	104	
	201208122	175.63	175.64	0.00	51.09	72051	5.60	14.51	0.30	59	0	0.48	15.14	30	35	38	11	264	96	24	0	123	0	513	125	
	201208122	175.64	175.65	6.52	35.21	81140	3.06	24.93	0.23	34	0	0.84	23.55	41	747	494	16	438	56	25	0	74	0	0	139	
	201208122	175.65	175.66	7.59	28.08	77933	3.01	21.39	0.41	72	0	0.67	21.89	29	130	33	0	270	72	24	0	188	0	0	76	

Gabrielle Redden
TMBs at MICO & GFM

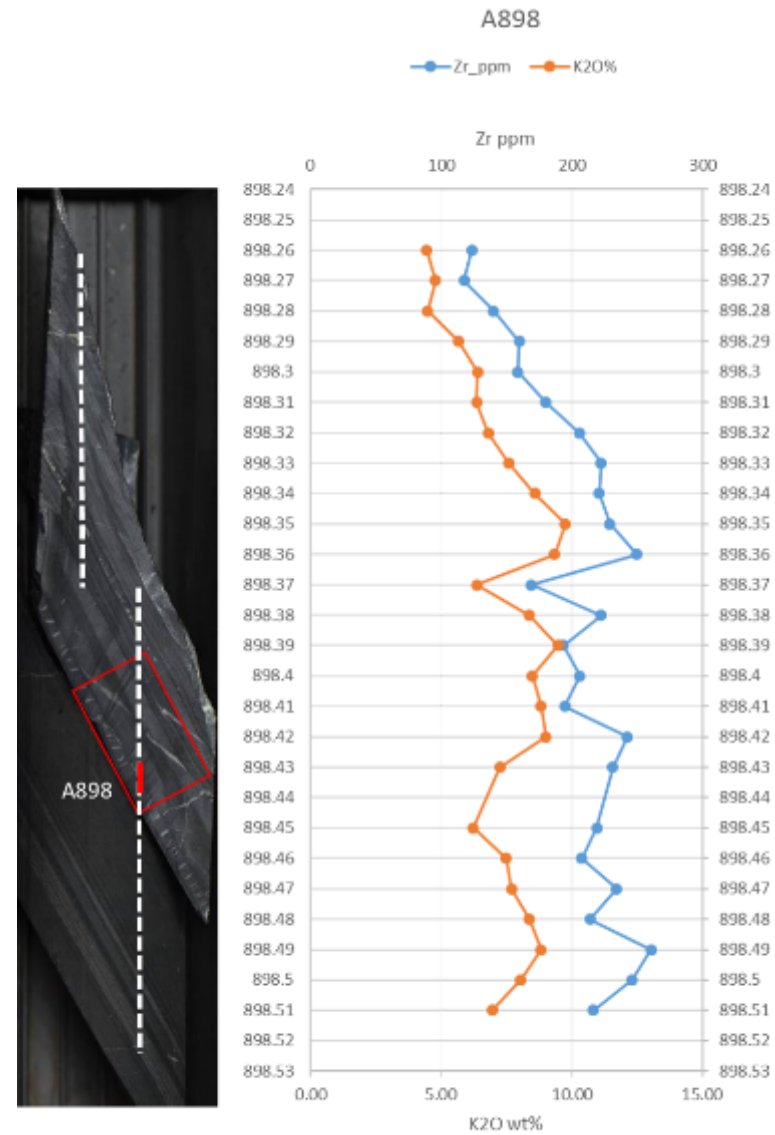
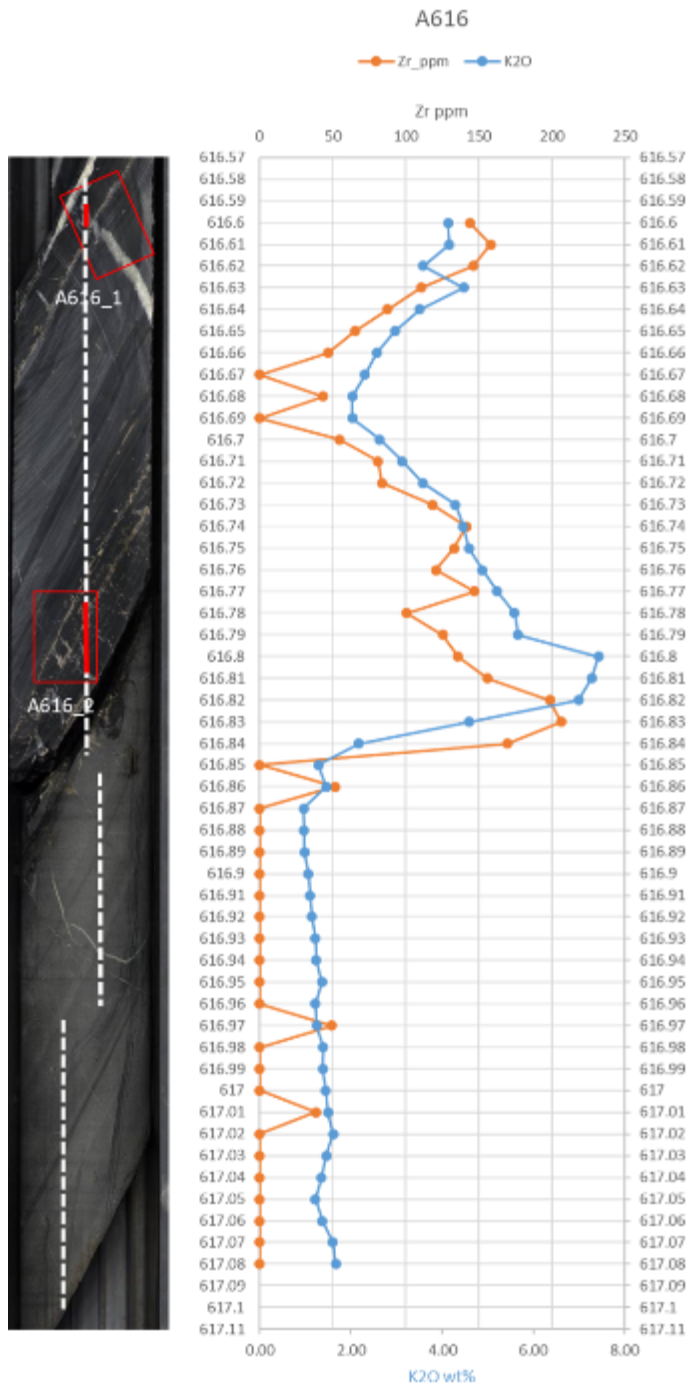
	DDH_name	From_m	To_m	Al2O3%	SiO2%	S_ppm	K2O%	CaO%	TiO2%	V_ppm	Cr_ppm	MnO%	Fe2O3%	Ni_ppm	Cu_ppm	Zn_ppm	Ga_ppm	As_ppm	Rb_ppm	Sr_ppm	Y_ppm	Zr_ppm	Nb_ppm	Ba_ppm	Pb_ppm
GFM-0.29	14CH73002	0.29	0.3	6.50	19.26	4397	3.84	42.46	0.12	ND	BDL	0.68	2.52	21	254	684	ND	BDL	57	98	BDL	106	BDL	ND	563
	14CH73002	0.3	0.31	BDL	10.83	3663	2.15	50.26	0.07	ND	BDL	0.83	1.88	24	405	1027	ND	82	32	130	BDL	82	BDL	ND	437
	14CH73002	0.31	0.32	6.28	12.49	4998	2.40	50.53	0.08	ND	BDL	0.76	1.93	18	371	885	ND	BDL	28	113	39	77	BDL	ND	480
	14CH73002	0.32	0.33	BDL	9.34	165402	1.89	32.14	0.30	ND	BDL	0.35	32.38	15	559	6731	BDL	533	BDL	54	ND	BDL	BDL	ND	1674
	14CH73002	0.33	0.34	3.86	39.51	26682	8.94	15.45	0.52	BDL	BDL	0.12	5.57	19	341	5590	BDL	ND	194	36	ND	429	BDL	535	3640
GFM-13	14CH73002	13.37	13.38	5.10	19.80	132415	2.33	9.58	0.12	ND	213	0.29	23.76	16	319	7599	31	803	BDL	26	ND	38	BDL	ND	529
	14CH73002	13.38	13.39	BDL	25.39	165722	2.78	10.61	0.10	ND	147	0.32	28.99	22	408	11364	50	941	BDL	BDL	ND	BDL	BDL	ND	837
	14CH73002	13.39	13.4	BDL	24.56	111180	3.90	12.42	0.22	BDL	BDL	0.42	23.68	21	216	2314	18	741	56	36	BDL	144	BDL	BDL	653
	14CH73002	13.4	13.41	6.72	34.81	37710	4.45	14.06	0.31	39	BDL	0.48	10.61	19	207	326	BDL	381	80	30	BDL	213	BDL	BDL	345
	14CH73002	13.41	13.42	BDL	28.62	17568	4.48	15.48	0.31	36	ND	0.56	8.28	23	184	237	BDL	335	120	46	BDL	219	BDL	BDL	343
	14CH73002	13.42	13.43	ND	21.48	18360	4.47	15.90	0.28	34	BDL	0.61	9.48	17	212	606	BDL	412	110	49	BDL	239	BDL	BDL	484
	14CH73002	13.43	13.44	7.66	33.43	20546	4.91	15.36	0.28	25	BDL	0.53	7.75	17	240	316	BDL	248	101	40	BDL	192	BDL	ND	380
	14CH73002	13.44	13.45	BDL	31.14	26431	5.19	13.70	0.33	42	BDL	0.49	9.06	18	302	338	BDL	457	111	39	BDL	261	BDL	BDL	366
	14CH73002	13.45	13.46	6.58	35.17	17800	5.99	13.11	0.31	33	ND	0.44	7.03	15	182	217	BDL	274	110	40	BDL	239	BDL	BDL	373
	14CH73002	13.46	13.47	6.92	31.54	20023	5.05	15.19	0.29	40	ND	0.52	8.23	22	179	246	BDL	355	102	53	BDL	175	BDL	BDL	250
	14CH73002	13.47	13.48	3.49	33.00	22915	5.15	14.30	0.33	34	ND	0.49	8.62	19	175	257	BDL	374	106	38	BDL	215	BDL	BDL	279
	14CH73002	13.48	13.49	6.49	34.11	30544	5.43	13.16	0.33	40	ND	0.45	9.28	20	233	352	10	397	107	34	BDL	20	BDL	BDL	282
	14CH73002	13.49	13.5	BDL	27.51	64306	4.99	12.15	0.41	43	BDL	0.44	15.24	23	281	423	BDL	471	103	29	BDL	292	BDL	ND	425
	14CH73002	13.5	13.51	9.30	34.97	40490	6.19	11.47	0.36	49	BDL	0.42	11.31	16	226	1152	13	262	118	34	BDL	249	BDL	ND	486
	14CH73002	13.51	13.52	10.06	42.79	58646	7.93	7.35	0.42	47	ND	0.25	18.56	13	473	3379	20	576	149	30	ND	293	BDL	550	1455
	14CH73002	13.52	13.53	6.29	49.65	8472	9.58	9.18	0.50	134	ND	0.19	4.20	18	434	321	13	98	213	30	BDL	341	BDL	11028	471
	14CH73002	13.53	13.54	BDL	24.91	65781	3.88	16.05	0.43	324	ND	0.28	19.02	9	500	7615	ND	117	163	117	ND	401	BDL	45847	8939
GFM-29	14CH73002	29.1	29.11	10.22	20.73	284825	0.32	8.85	0.07	ND	286	0.26	45.98	BDL	476	1714	BDL	807	BDL	BDL	ND	BDL	BDL	ND	1648
	14CH73002	29.11	29.12	BDL	9.47	335449	0.16	7.82	0.04	ND	92	0.20	58.61	14	458	2873	ND	987	BDL	BDL	ND	BDL	BDL	ND	3771
	14CH73002	29.12	29.13	BDL	5.79	287526	0.13	18.37	0.03	ND	BDL	0.23	59.11	12	408	4986	ND	637	BDL	BDL	ND	BDL	BDL	ND	4066
	14CH73002	29.13	29.14	BDL	7.84	299792	0.08	17.90	0.02	ND	47	0.21	56.34	16	401	12049	16	513	BDL	BDL	ND	BDL	BDL	ND	4605
	14CH73002	29.14	29.15	BDL	7.08	308951	0.19	14.36	0.02	ND	53	0.37	54.38	15	287	1458	ND	705	BDL	BDL	ND	BDL	BDL	ND	8109
	14CH73002	29.15	29.16	BDL	3.92	251583	0.24	16.58	0.02	ND	BDL	0.56	51.71	BDL	300	464	ND	916	BDL	BDL	ND	BDL	BDL	ND	6689
	14CH73002	29.16	29.17	BDL	7.20	38265	0.41	30.44	0.02	ND	BDL	1.43	23.73	26	488	849	ND	BDL	BDL	27	ND	BDL	BDL	ND	4192
	14CH73002	29.17	29.18	5.49	4.24	278264	0.40	17.26	0.04	ND	44	0.59	48.75	BDL	353	1358	ND	1035	BDL	BDL	ND	BDL	BDL	ND	4656
	14CH73002	29.18	29.19	7.11	2.20	400566	0.16	5.79	0.03	ND	48	0.18	60.52	BDL	379	2611	ND	1741	BDL	BDL	ND	BDL	BDL	ND	6168
	14CH73002	29.19	29.2	7.13	13.08	291387	0.14	15.17	0.02	ND	42	0.32	48.96	23	387	11250	BDL	892	BDL	BDL	ND	BDL	BDL	ND	5709
	14CH73002	29.2	29.21	BDL	ND	344236	0.07	10.59	0.03	ND	55	0.18	64.69	16	421	15318	ND	535	ND	BDL	ND	BDL	BDL	ND	19055
	14CH73002	29.21	29.22	5.83	1.99	239144	0.13	25.56	0.03	ND	BDL	0.47	51.10	17	356	3436	ND	BDL	BDL	28	ND	BDL	BDL	ND	16140
	14CH73002	29.22	29.23	BDL	3.80	199065	0.22	22.78	0.02	ND	55	0.51	51.52	15	331	6298	ND	350	BDL	BDL	ND	BDL	BDL	ND	5257
	14CH73002	29.23	29.24	BDL	1.99	289670	0.15	15.29	0.01	ND	43	0.30	59.91	BDL	311	8639	ND	789	BDL	BDL	ND	BDL	BDL	ND	4925
	14CH73002	29.24	29.25	BDL	4.29	247036	0.08	25.87	0.01	ND	BDL	0.22	48.45	36	429	60827	145	187	BDL	31	ND	BDL	BDL	ND	5450
	14CH73002	29.25	29.26	BDL	5.00	143162	0.12	40.47	0.00	ND	BDL	0.38	28.99	35	324	73897	172	BDL	BDL	48	ND	BDL	BDL	ND	3826
	14CH73002	29.26	29.27	BDL	3.67	256573	0.43	15.96	0.03	ND	46	0.50	51.69	17	269	6334	BDL	1086	BDL	BDL	ND	BDL	BDL	ND	3620
	14CH73002	29.27	29.28	BDL	5.44	297909	1.34	10.06	0.07	ND	43	0.30	53.69	BDL	270	1444	ND	1070	BDL	BDL	ND	109	BDL	ND	3606
	14CH73002	29.28	29.29	11.96	47.02	16406	10.31	8.08	0.27	BDL	ND	0.20	5.68	16	77	1011	ND	ND	147	17	ND	366	BDL	BDL	4720
	14CH73002	29.29	29.3	8.32	23.50	223810	5.13	6.44	0.16	ND	BDL	0.16	34.28	14	164	1505	ND	442	54	BDL	ND	174	BDL	ND	7976
	14CH73002	29.3	29.31	BDL	7.68	320827	1.02	6.24	0.08	ND	BDL	0.22	52.88	15	248	2942	ND	922	ND	BDL	ND	BDL	BDL	ND	6376
	14CH73002	29.31	29.32	BDL	8.82	266895	0.57	12.92	0.06	ND	47	0.42	48.14	21	257	2588	ND	535	BDL	29	ND	BDL	BDL	ND	19492
	14CH73002	29.32	29.33	BDL	6.57	306470	0.84	9.65	0.05	ND	BDL	0.35	51.42	BDL	327	799	ND	626	BDL	BDL	ND	BDL	BDL	ND	3477
	14CH73002	29.33	29.34	BDL	5.15	318326	0.87	8.12	0.03	ND	69	0.28	53.72	15	312	676	ND	465	BDL	BDL	ND	BDL	BDL	ND	11097
	14CH73002	29.34	29.35	BDL	4.54	273969	0.39	13.78	0.03	ND	BDL	0.48	50.11	12	159	1108	ND	604	BDL	BDL	ND	BDL	BDL	ND	7354
	14CH73002	29.35	29.36	5.52	6.48	136004	0.23	25.09	0.03	ND	BDL	1.00	35.62	20	216	655	ND	182	BDL	27	ND	BDL	BDL	ND	5174

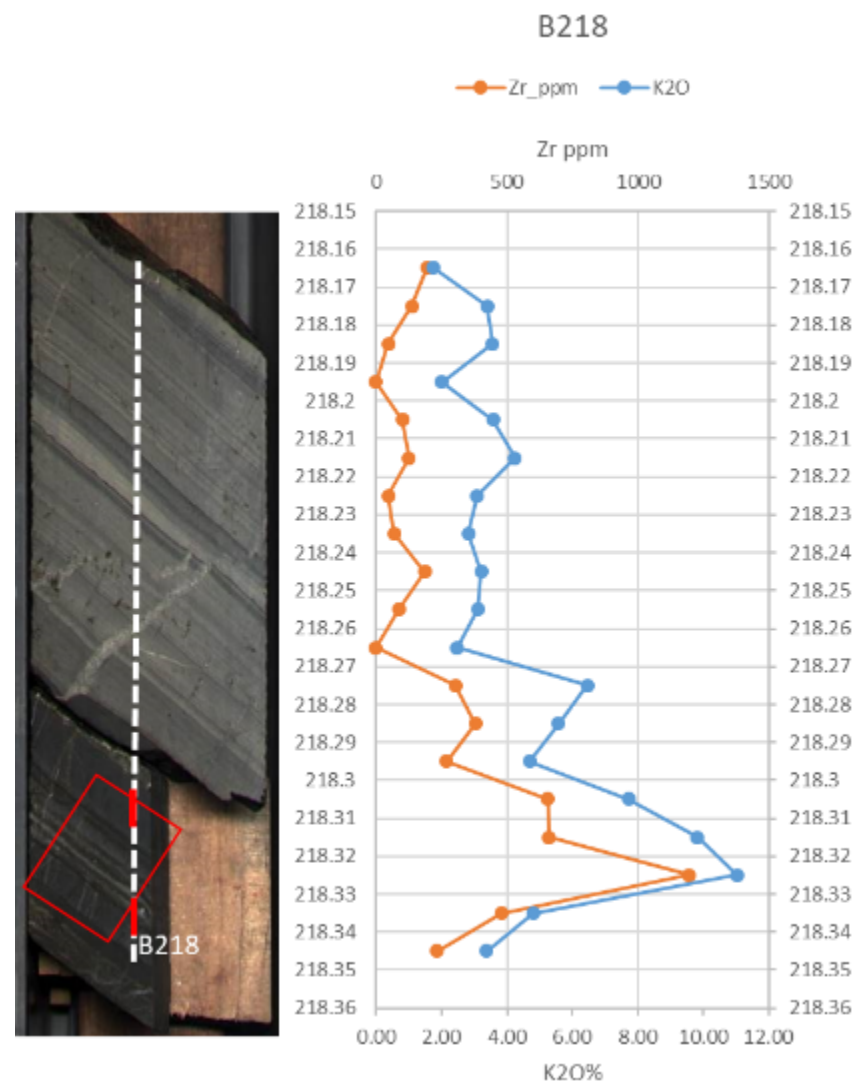
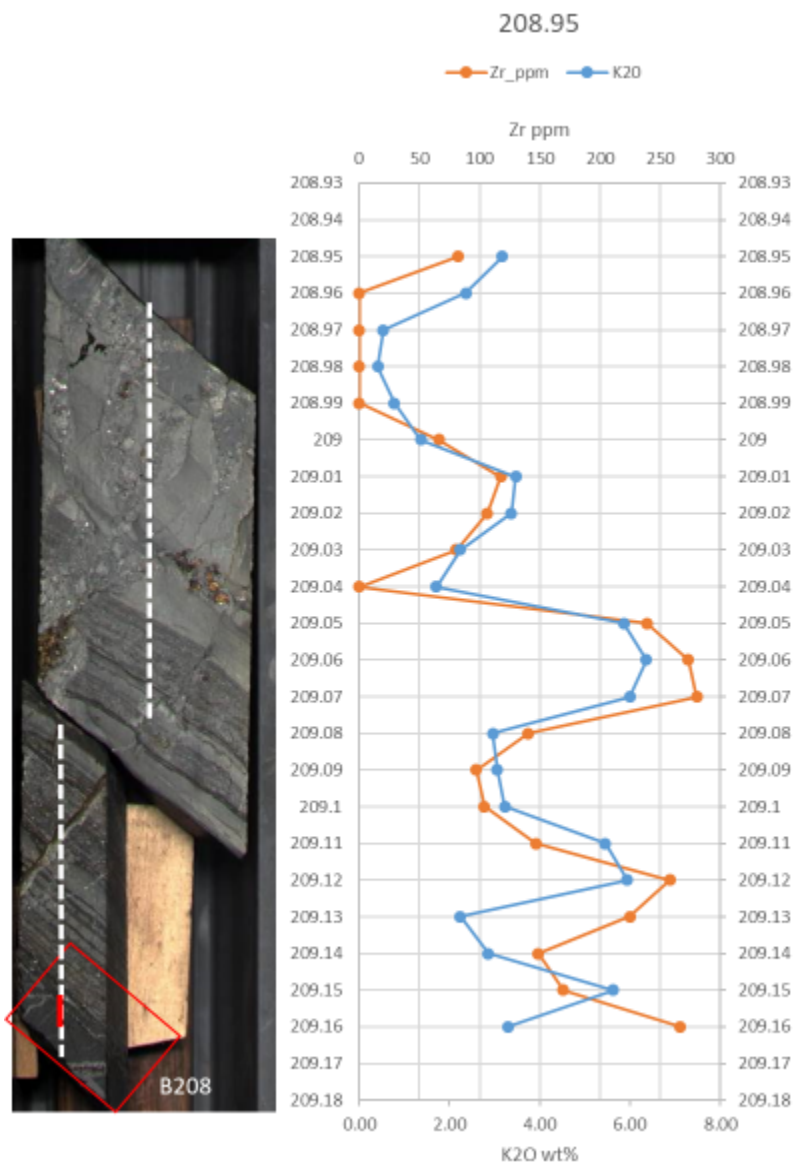
Gabrielle Redden

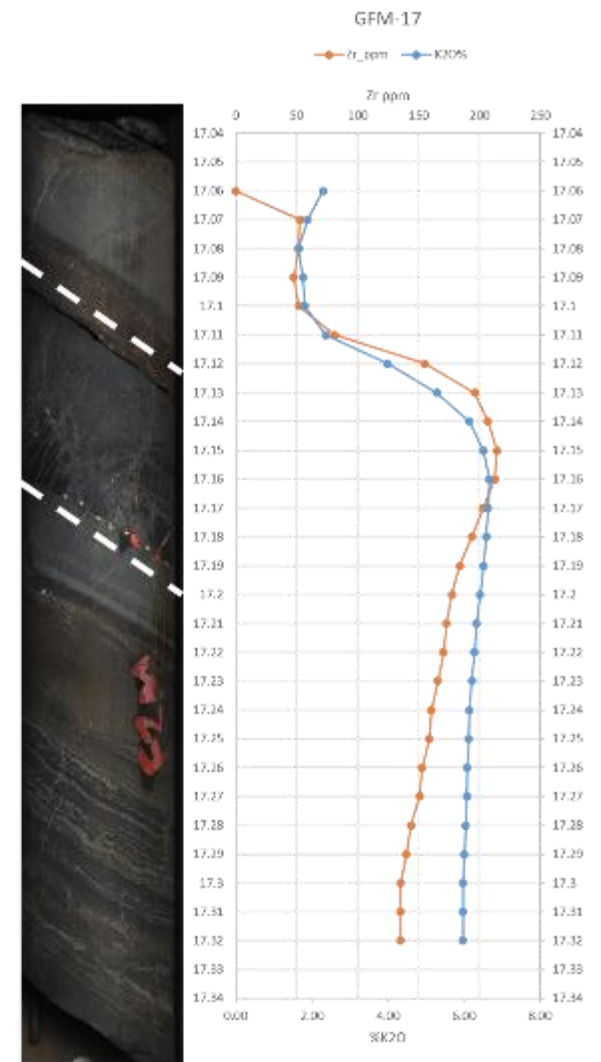
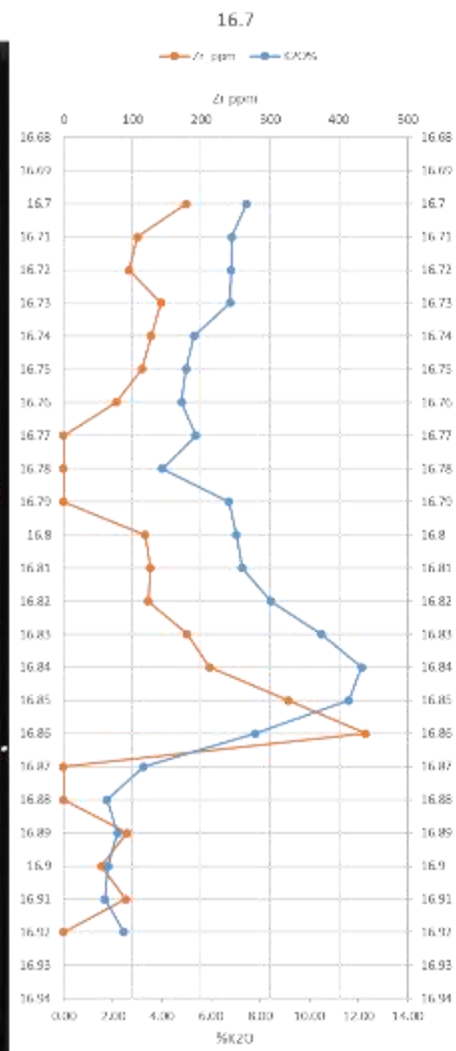
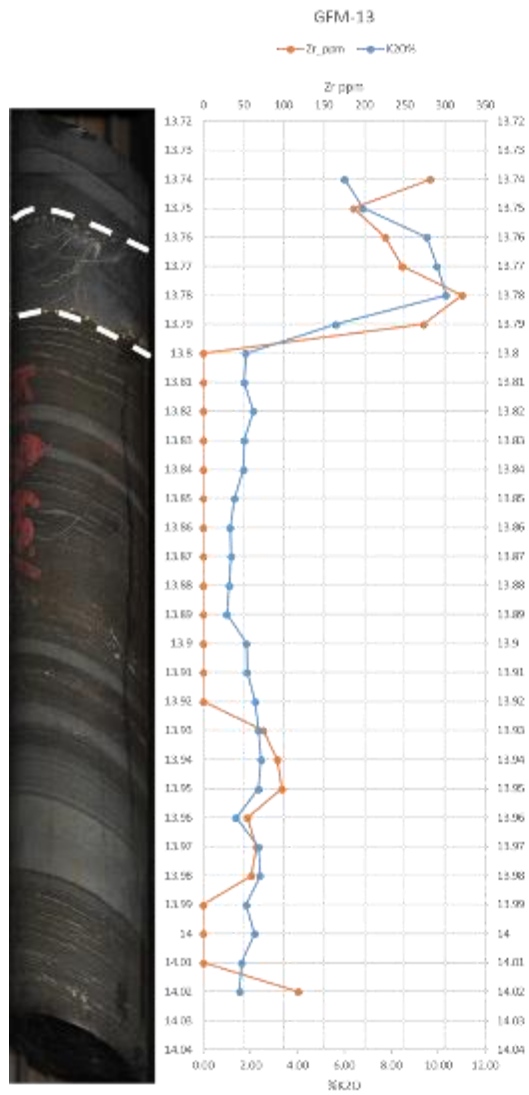
DDH_name	From_m	To_m	AI2O3%	SiO2%	S_ppm	K2O%	CaO%	TI02%	V_ppm	Cr_ppm	MnO%	Fe2O3%	Ni_ppm	Cu_ppm	Zn_ppm	Ga_ppm	As_ppm	Rb_ppm	Ti	Al	X_PPM	Zr	Y	Other		
2012113002	616.6	616.61	7.17	46.89	5340	4.13	30.25	0.3388	38.84	ND	0.2188	3.2523	29.13	32.91	24.6	10.62	ND	90.09	43.08	BDL	143.7	BDL	675.42	BDL		
2012113002	616.61	616.62	BDL	46.35	25808	4.15	40.76	0.3144	46.51	ND	0.3586	9.6007	35.88	46.44	34.57	BDL	BDL	99	63.75	BDL	158.26	BDL	378.36	BDL		
2012113002	616.62	616.63	BDL	45.19	29736	3.58	43.98	0.2695	BDL	ND	0.4	10.3824	38.79	42.45	34.68	BDL	BDL	89.77	70.87	BDL	146.24	BDL	BDL	BDL		
2012113002	616.63	616.64	BDL	53.01	49521	4.47	30.67	0.2074	BDL	BDL	0.385	13.789	41.01	30.2	28.38	BDL	BDL	81.29	52.63	BDL	110.45	BDL	BDL	BDL		
2012113002	616.64	616.65	7.37	46.88	23036	3.51	41.50	0.1551	BDL	BDL	0.4696	9.6219	33.92	76.22	33.27	BDL	BDL	54.66	85.38	BDL	87.61	BDL	BDL	BDL		
2012113002	616.65	616.66	BDL	40.89	4405	2.96	49.47	0.1411	BDL	BDL	0.5605	4.5192	34.68	BDL	35.02	BDL	BDL	44.56	113.43	BDL	65.31	BDL	BDL	BDL		
2012113002	616.66	616.67	5.65	38.65	1844	2.56	53.56	0.1056	BDL	BDL	0.5488	3.3418	27.76	BDL	26.86	ND	BDL	36.19	116.64	BDL	46.88	BDL	BDL	97.55		
2012113002	616.67	616.68	6.20	34.50	10805	2.31	55.66	0.091	BDL	BDL	0.5606	5.3985	30.93	BDL	29.95	ND	BDL	28.24	112.56	40.43	0	BDL	BDL	76.57		
2012113002	616.68	616.69	3.37	31.83	BDL	2.03	57.32	0.078	BDL	BDL	0.6125	3.6122	35.2	BDL	37.83	ND	BDL	27.27	139.92	BDL	43.4	BDL	BDL	102.09		
2012113002	616.69	616.7	BDL	30.74	2105	2.03	57.57	0.0769	BDL	BDL	0.6541	4.0818	35.3	BDL	35.64	ND	BDL	38.33	130.8	BDL	0	BDL	BDL	77.56		
2012113002	616.7	616.71	5.91	38.40	1567	2.63	52.56	0.1175	BDL	BDL	0.6202	5.0013	30.58	BDL	33.33	ND	BDL	45.21	99.53	BDL	54.49	BDL	BDL	BDL		
2012113002	616.71	616.72	6.09	39.35	9405	3.13	49.52	0.1767	BDL	BDL	0.5951	6.8145	34.77	BDL	32.15	BDL	BDL	55.09	105.87	BDL	80.93	BDL	BDL	BDL		
2012113002	616.72	616.73	BDL	40.69	4430	3.57	44.13	0.1961	BDL	BDL	0.5955	6.3032	28.28	BDL	22.86	ND	BDL	68.51	103.96	BDL	83.74	BDL	BDL	BDL		
2012113002	616.73	616.74	ND	40.31	7719	4.29	34.92	0.2177	32.45	ND	0.5894	7.9138	35.88	BDL	24.77	ND	BDL	91.81	89.72	BDL	118.33	BDL	BDL	431.26	BDL	
2012113002	616.74	616.75	BDL	50.23	8821	4.46	33.17	0.2483	30.69	ND	0.5148	7.3251	37.93	BDL	26.18	BDL	BDL	73.88	62.45	BDL	141.56	BDL	BDL	71.04		
2012113002	616.75	616.76	6.39	50.71	9452	4.58	33.78	0.2542	BDL	BDL	0.4551	7.1552	27.59	52.79	15.93	BDL	BDL	75.92	67.22	BDL	133.02	BDL	BDL	BDL		
2012113002	616.76	616.77	BDL	52.82	33322	4.88	30.14	0.2778	41.88	BDL	0.4381	9.5301	32.21	56.27	31.3	BDL	BDL	97.5	65.57	BDL	120.6	BDL	BDL	BDL		
2012113002	616.77	616.78	6.45	55.44	60065	5.20	24.55	0.251	37.72	BDL	0.3499	14.1499	28.11	36.61	19.2	BDL	BDL	92.24	48.12	BDL	147.17	BDL	BDL	BDL		
2012113002	616.78	616.79	BDL	51.91	93326	5.58	18.78	0.2396	31.97	BDL	0.2774	19.9264	34.34	42.45	17.73	BDL	BDL	124.2	77.42	35.44	100.7	BDL	BDL	BDL		
2012113002	616.79	616.8	9.08	55.97	136964	5.66	15.88	0.2087	BDL	BDL	0.2001	25.4682	34	87.19	14.92	BDL	BDL	79.47	58.09	28.84	125.27	BDL	BDL	280.15	BDL	
2012113002	616.8	616.81	10.02	68.94	83730	7.42	8.85	0.2846	39.8	BDL	0.1434	16.2423	33.4	44.16	19.25	BDL	BDL	86.44	21.54	ND	135.82	BDL	BDL	639.42	203.46	
2012113002	616.81	616.82	10.30	67.50	75450	7.27	12.53	0.3429	33.89	BDL	0.1549	14.9136	35.11	48.72	14.75	BDL	BDL	102.33	22.58	ND	155.99	BDL	BDL	525.74	189.57	
2012113002	616.82	616.83	4.04	60.75	83774	6.99	6.63	0.3283	40.12	BDL	0.1184	15.277	33.57	637.24	18.92	10.24	BDL	101.04	16.33	ND	198.59	BDL	BDL	488.21	146.75	
2012113002	616.83	616.84	BDL	39.30	90043	4.58	5.28	0.2627	32.45	BDL	0.0922	16.3093	27.17	93.88	14.13	BDL	BDL	94.49	15.2	BDL	206.47	BDL	BDL	246.35	59.83	
2012113002	616.84	616.85	BDL	20.42	165742	2.17	11.96	0.3818	ND	BDL	0.1085	37.3829	29.82	112.4	BDL	BDL	BDL	BDL	BDL	BDL	169.48	ND	ND	ND	ND	
2012113002	616.85	616.86	BDL	14.52	41625	1.29	32.84	0.169	ND	BDL	0.3893	15.9305	29.05	204.86	58.33	ND	BDL	42.31	88.68	BDL	0	BDL	BDL	ND	BDL	
2012113002	616.86	616.87	5.09	20.81	11234	1.46	47.91	0.0612	BDL	BDL	0.586	7.6398	35.71	31.77	84.79	BDL	BDL	42.95	115.77	39.59	51.55	BDL	BDL	BDL	BDL	
2012113002	616.87	616.88	BDL	20.68	3933	0.96	50.59	0.0304	ND	BDL	0.628	5.5083	26.83	BDL	81.07	ND	BDL	BDL	BDL	BDL	82.88	52.23	0	BDL	BDL	BDL
2012113002	616.88	616.89	5.89	27.39	3324	0.98	47.69	0.0455	ND	BDL	0.6514	5.3184	33.4	27.21	77.64	BDL	BDL	BDL	113.6	BDL	0	BDL	BDL	BDL	BDL	BDL
2012113002	616.89	616.9	4.52	27.44	BDL	0.98	43.66	0.0327	BDL	BDL	0.719	6.3867	27.08	32.2	70.09	ND	BDL	BDL	113.6	BDL	0	BDL	BDL	BDL	BDL	BDL
2012113002	616.9	616.91	4.62	31.49	BDL	1.07	39.39	0.0395	ND	BDL	0.7611	7.0074	29.82	BDL	59.62	BDL	BDL	BDL	94.84	BDL	0	BDL	BDL	BDL	BDL	BDL
2012113002	616.91	616.92	4.28	28.64	BDL	1.11	37.19	0.0431	ND	BDL	0.8045	7.6394	31.01	BDL	61.25	ND	BDL	BDL	91.02	BDL	0	BDL	BDL	BDL	BDL	BDL
2012113002	616.92	616.93	BDL	23.93	BDL	1.15	36.46	0.0468	BDL	BDL	0.8626	8.3248	35.28	BDL	63.06	ND	BDL	BDL	94.67	BDL	0	BDL	BDL	BDL	BDL	BDL
2012113002	616.93	616.94	BDL	26.84	BDL	1.22	36.69	0.0554	BDL	BDL	0.85	8.3396	28.88	BDL	57.26	ND	BDL	BDL	96.93	BDL	0	BDL	BDL	BDL	BDL	BDL
2012113002	616.94	616.95	BDL	23.91	1624	1.24	38.45	0.0589	BDL	BDL	0.8527	8.7184	38.79	BDL	71.56	BDL	BDL	BDL	97.77	BDL	0	BDL	BDL	BDL	BDL	BDL
2012113002	616.95	616.96	BDL	23.48	8683	1.36	36.56	0.0768	ND	BDL	0.8479	9.8219	29.99	33.05	76.62	BDL	BDL	23.95	98.23	BDL	0	BDL	BDL	BDL	BDL	BDL
2012113002	616.96	616.97	BDL	23.94	BDL	1.22	34.51	0.0547	ND	BDL	0.7793	7.5601	33.83	25.07	79.1	BDL	BDL	24.91	85.98	BDL	0	BDL	BDL	BDL	BDL	BDL
2012113002	616.97	616.98	BDL	18.80	1755	1.25	33.99	0.063	ND	BDL	0.8152	8.2005	36.73	37.75	81.3	BDL	BDL	23.73	101.27	BDL	49.55	BDL	BDL	BDL	BDL	BDL
2012113002	616.98	616.99	BDL	23.91	BDL	1.39	33.47	0.0604	BDL	BDL	0.8027	7.99	35.8	BDL	75.84	BDL	BDL	31.78	77.91	BDL	0	BDL	BDL	BDL	BDL	BDL
2012113002	616.99	617	5.14	25.93	1375	1.39	34.29	0.0519	ND	BDL	0.7427	7.4745	28.7	BDL	73.75	BDL	BDL	19.65	82.77	BDL	0	BDL	BDL	BDL	BDL	BDL
2012113002	617	617.01	BDL	24.86	5784	1.45	32.81	0.0664	BDL	BDL	0.7846	8.6327	27.34	27.5	73.08	BDL	BDL	30.28	84.59	BDL	0	BDL	BDL	BDL	BDL	BDL
2012113002	617.01	617.02	BDL	27.18	BDL	1.50	30.69	0.0675	BDL	BDL	0.7719	8.2825	29.82	BDL	71.33	BDL	BDL	43.92	82.42	BDL	38.33	BDL	BDL	BDL	BDL	BDL
2012113002	617.02	617.03	4.50	28.76	6049	1.61	29.84	0.0814	BDL	BDL	0.7329	8.5426	31.52	53.85	73.98	BDL	BDL	28.99	68.35	BDL	0	BDL	BDL	BDL	BDL	BDL
2012113002	617.03	617.04	BDL	29.50	BDL	1.46	31.06	0.0731	ND	BDL	0.7535	7.9606	28.62	BDL	59.68	BDL	BDL	34.15	79.21	BDL	0	BDL	BDL	BDL	BDL	BDL
2012113002	617.04	617.05	5.73	29.07	6221	1.36	32.64	0.0549	ND	BDL	0.7107	8.0267	24.95	BDL	74.77	BDL	BDL	30.39	76.26	BDL	0	BDL	BDL	BDL	BDL	BDL
2012113002	617.05	617.06	ND	23.96	3659	1.22	33.16	0.0524	BDL	BDL	0.7621	7.9964	26.31	27.78	86.81	BDL	BDL	BDL	82.6	BDL	0	BDL	BDL	BDL	BDL	BDL
2012113002	617.06	617.07	BDL	24.72	8499	1.37	33.89	0.0592	BDL	BDL	0.7287	8.386	27.85	45.45	101	ND	BDL	31.78	88.42	BDL	0	BDL	BDL	BDL	92.59	BDL
2012113002	617.07	617.08	BDL	25.41	1416	1.60	34.11	0.063	BDL	BDL	0.7277	7.1132	29.73	51	103.65	BDL	BDL	30.6	77.56	BDL	0	BDL	BDL	BDL	BDL	BDL
2012113002	617.08	617.09	3.71	21.77	1590	1.66	35.30	0.0572	BDL	BDL	0.7031	6.874	27.25	59.55	120.93	BDL	BDL	32.54	91.8							

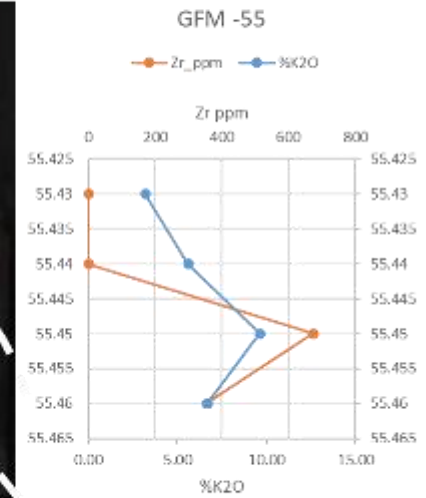
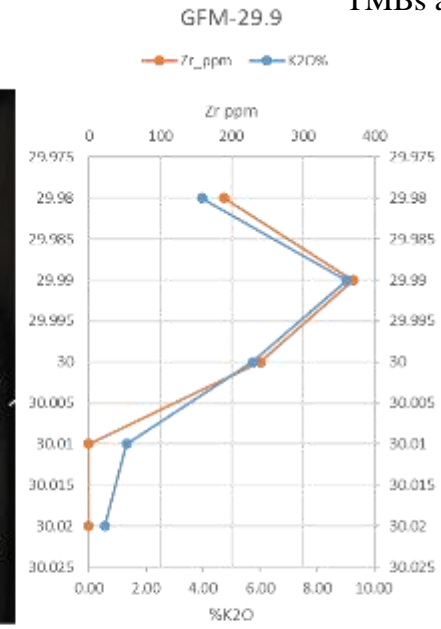
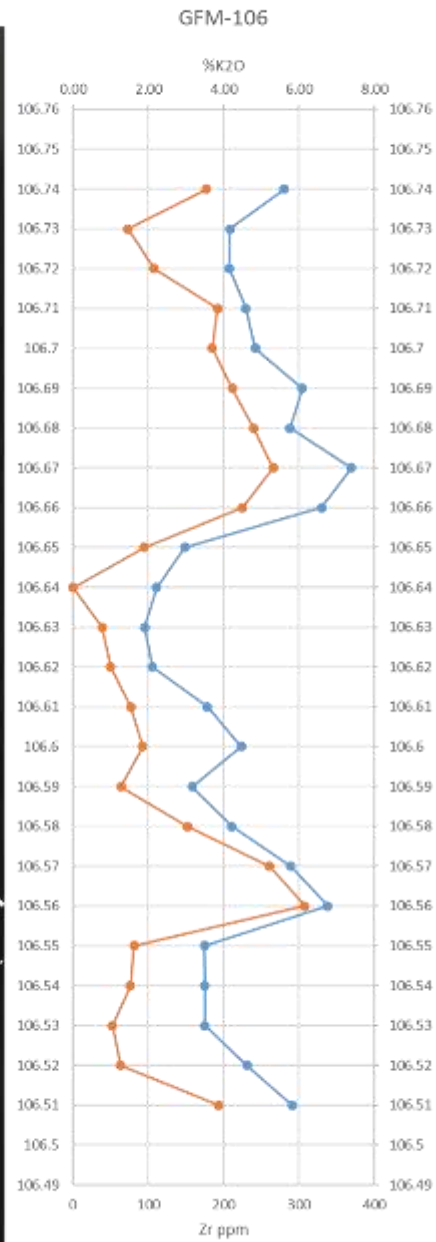
Gabrielle Redden
TMBs at MICO & GFM

Additional GFM Samples		Al2O3%	SiO2%	S_ppm	K2O%	CaO%	TiO2%	V_ppm	Cr_ppm	MnO%	Fe2O3%	Ni_ppm	Cu_ppm	Zn_ppm	Ga_ppm	As_ppm	Rb_ppm	Sr_ppm	Y_ppm	Zr_ppm	Nb_ppm	Ba_ppm	Pb_ppm	
140H73001	13.74	13.75	BDL	30.98	45958	6.01	11.37	0.44	48	ND	0.40	11.11	21	73	378	12	313	125	24	BDL	282	BDL	ND	520
140H73001	13.75	13.76	9.09	32.39	99539	6.80	7.34	0.33	BDL	BDL	0.24	16.99	14	63	834	12	467	88	BDL	BDL	186	BDL	BDL	591
140H73001	13.76	13.77	11.21	44.18	54286	9.53	5.98	0.62	BDL	ND	0.13	8.42	19	83	1967	BDL	189	141	21	BDL	226	BDL	223	990
140H73001	13.77	13.78	12.55	50.30	9882	9.95	8.39	0.46	BDL	BDL	0.14	3.26	14	48	199	ND	ND	135	30	ND	247	BDL	341	1702
140H73001	13.78	13.79	12.42	50.37	8241	10.33	8.80	0.50	27	ND	0.13	2.50	16	81	2356	ND	ND	144	28	BDL	321	BDL	548	3371
140H73001	13.79	13.8	BDL	24.38	164790	5.66	6.90	0.66	BDL	BDL	0.20	23.74	21	98	13105	35	361	103	BDL	ND	274	BDL	ND	1922
140H73001	13.8	13.81	8.27	14.59	254673	1.81	8.14	0.10	ND	37	0.24	36.92	15	94	9754	34	984	BDL	BDL	ND	0	BDL	ND	1056
140H73001	13.81	13.82	5.89	13.65	273809	1.74	7.84	0.14	ND	BDL	0.23	37.68	22	157	28674	87	1019	BDL	BDL	ND	0	BDL	ND	833
140H73001	13.82	13.83	BDL	23.53	192299	2.13	11.43	0.22	ND	BDL	0.38	25.77	30	142	28073	86	562	BDL	BDL	ND	0	BDL	ND	852
140H73001	13.83	13.84	BDL	21.88	221306	1.74	8.97	0.47	ND	BDL	0.28	30.25	21	134	27241	55	369	BDL	BDL	ND	0	BDL	ND	4827
140H73001	13.84	13.85	BDL	22.74	188152	1.71	11.15	0.20	ND	BDL	0.36	28.21	26	124	20693	24	ND	BDL	BDL	ND	0	BDL	ND	9133
140H73001	13.85	13.86	7.63	22.67	211973	1.32	11.58	0.16	ND	BDL	0.33	29.01	25	123	22720	38	BDL	ND	BDL	ND	0	BDL	ND	8573
140H73001	13.86	13.87	7.73	29.41	220526	1.15	9.62	0.13	ND	BDL	0.22	26.54	29	131	30331	81	332	ND	BDL	ND	0	BDL	ND	4506
140H73001	13.87	13.88	BDL	17.76	281615	1.18	6.31	0.15	ND	BDL	0.19	36.39	28	171	44563	135	738	BDL	BDL	ND	0	BDL	ND	3011
140H73001	13.88	13.89	BDL	14.49	304271	1.10	6.90	0.10	ND	BDL	0.20	34.63	30	209	75877	218	336	ND	BDL	ND	0	BDL	ND	9686
140H73001	13.89	13.9	BDL	18.18	281926	1.00	10.88	0.05	ND	76	0.26	31.82	43	312	111364	319	387	BDL	BDL	ND	0	BDL	ND	9460
140H73001	13.9	13.91	7.41	31.43	169808	1.84	12.18	0.10	ND	BDL	0.35	22.30	30	159	35439	107	280	BDL	BDL	ND	0	BDL	ND	3842
140H73001	13.91	13.92	6.27	30.50	174929	1.87	11.04	0.09	ND	BDL	0.33	25.15	28	167	24520	22	ND	BDL	BDL	31	ND	ND	ND	14980
140H73001	13.92	13.93	BDL	26.92	157979	2.21	11.92	0.12	ND	43	0.38	27.16	31	150	17113	BDL	BDL	BDL	BDL	ND	0	ND	ND	11860
140H73001	13.93	13.94	BDL	24.08	132577	2.36	14.56	0.15	ND	BDL	0.51	25.50	23	123	6669	BDL	349	BDL	29	ND	75	ND	ND	5701
140H73001	13.94	13.95	BDL	30.06	101882	2.46	14.31	0.15	ND	BDL	0.50	20.91	24	111	2110	BDL	530	28	32	ND	92	BDL	ND	2087
140H73001	13.95	13.96	5.00	35.94	32520	2.36	17.09	0.14	BDL	BDL	0.61	10.63	22	77	3655	14	145	42	35	ND	98	BDL	ND	1127
140H73001	13.96	13.97	BDL	18.32	3828	1.40	25.37	0.06	ND	BDL	1.14	9.92	24	88	2954	BDL	ND	45	63	ND	55	BDL	ND	2759
140H73001	13.97	13.98	BDL	28.04	4447	2.35	19.37	0.18	BDL	BDL	0.83	7.04	27	91	1970	15	109	63	52	ND	66	BDL	ND	612
140H73001	13.98	13.99	BDL	25.02	108625	2.42	14.89	0.13	BDL	BDL	0.54	22.46	26	85	2979	13	530	BDL	21	ND	60	BDL	ND	1043
140H73001	13.99	14	BDL	22.41	209081	1.83	10.21	0.08	ND	51	0.32	33.17	24	157	25321	89	892	BDL	BDL	ND	0	BDL	ND	1379
140H73001	14	14.01	BDL	20.22	186702	2.19	11.70	0.09	ND	BDL	0.38	32.71	27	164	17982	73	800	BDL	BDL	ND	0	BDL	ND	1233
140H73001	14.01	14.02	BDL	24.50	163006	1.63	15.21	0.08	ND	BDL	0.39	26.39	34	174	29324	88	402	BDL	BDL	ND	0	BDL	ND	3873
140H73001	14.02	14.03	7.00	18.81	218807	1.55	8.68	0.19	BDL	BDL	0.25	33.58	32	194	32558	64	ND	BDL	BDL	ND	118	ND	ND	8394
140H73001	14.06	17.07	BDL	41.92	68833	2.29	11.54	0.12	BDL	BDL	0.35	7.23	31	307	50439	152	ND	BDL	32	ND	0	BDL	ND	6061
140H73001	17.07	17.08	BDL	40.42	39032	1.89	13.24	0.10	BDL	BDL	0.43	5.38	27	246	29805	97	ND	34	42	ND	53	BDL	BDL	2867
140H73001	17.08	17.09	BDL	38.24	26969	1.66	15.27	0.09	BDL	BDL	0.51	5.11	27	265	20899	70	ND	34	46	ND	51	BDL	BDL	2267
140H73001	17.09	17.1	BDL	37.98	32427	1.76	14.79	0.11	BDL	BDL	0.49	5.32	26	295	24438	79	ND	41	47	ND	48	BDL	BDL	3179
140H73001	17.1	17.11	3.75	39.66	62272	1.82	14.19	0.11	12	25	0.44	6.37	29	353	45202	144	ND	44	51	ND	52	BDL	BDL	4964
140H73001	17.11	17.12	7.79	39.06	85648	2.37	12.43	0.16	13	24	0.37	8.12	30	362	48551	155	ND	58	45	ND	81	BDL	BDL	4969
140H73001	17.12	17.13	8.72	40.62	74184	4.00	10.74	0.18	14	BDL	0.30	7.09	28	318	39455	125	ND	118	38	ND	155	BDL	BDL	4906
140H73001	17.13	17.14	5.78	40.20	63631	5.28	9.62	0.19	13	BDL	0.27	6.32	27	309	33992	98	ND	161	36	27	196	BDL	95	6697
140H73001	17.14	17.15	6.92	41.80	56311	6.14	8.61	0.20	11	BDL	0.23	5.57	26	293	28886	76	ND	178	33	43	207	BDL	121	8013
140H73001	17.15	17.16	6.00	42.45	50535	6.51	7.98	0.19	11	BDL	0.21	5.22	26	296	26592	41	ND	185	33	26	215	BDL	193	14646
140H73001	17.16	17.17	5.66	43.97	47386	6.67	7.37	0.20	11	ND	0.19	4.88	26	282	24690	22	ND	187	33	17	213	BDL	242	17840
140H73001	17.17	17.18	5.99	44.70	44834	6.64	7.25	0.22	11	ND	0.19	4.72	25	268	22543	13	ND	181	33	ND	203	BDL	241	17985
140H73001	17.18	17.19	6.49	45.17	41250	6.58	7.22	0.21	10	ND	0.20	4.46	25	254	20375	9	ND	174	32	19	194	BDL	258	16710
140H73001	17.19	17.2	6.59	45.00	40185	6.52	7.26	0.20	9	ND	0.20	4.48	25	251	20199	13	ND	169	31	16	184	BDL	263	15743
140H73001	17.2	17.21	6.74	45.34	43128	6.43	6.98	0.20	8	ND	0.19	4.71	25	252	22559	24	ND	165	30	ND	177	BDL	253	15212
140H73001	17.21	17.22	7.03	45.74	47673	6.33	6.64	0.19	8	BDL	0.18	5.07	25	258	25720	37	ND	162	30	ND	173	BDL	243	14914
140H73001	17.22	17.23	7.27	46.14	52173	6.27	6.36	0.19	8	BDL	0.17	5.27	25	265	29596	52	ND	159	30	ND	171	BDL	231	14762
140H73001	17.23	17.24	7.27	45.46	57018	6.21	6.31	0.18	8	BDL	0.17	5.76	25	270	31798	61	ND	157	30	ND	166	BDL	223	14452
140H73001	17.24	17.25	7.31	44.37	59995	6.14	6.57	0.18	7	BDL	0.18	6.26	25	270	32433	65	ND	154	31	ND	161	BDL	214	13943
140H73001	17.25	17.26	6.57	42.88	62073	6.12	6.81	0.18	7	BDL	0.19	6.89	25	268	31599	63	ND	153	32	ND	159	BDL	204	13444
140H73001	17.26	17.27	7.30	42.33	62963	6.08	7.06	0.18	8	BDL	0.20	7.21	24	259	30561	62	ND	149	32	ND	153	BDL	196	12685
140H73001	17.27	17.28	7.05	41.35	63538	6.07	7.22	0.18	8	BDL	0.20	7.62	24	257	29697	61	ND	148	32	ND	151	BDL	202	12144
140H73001	17.28	17.29	8.61	41.50	65157	6.05	7.19	0.17	7	BDL	0.20	7.83	23	248	28907	61	ND	142	31	ND	144	BDL	197	11373
140H73001	17.29	17.3	8.61	41.22	66238	6.01	7.23	0.17	7	BDL	0.20	7.94	23	246	29712	65	ND	140	31	ND	140	BDL	198	11022
140H73001	17.3	17.31	9.53	41.17	67764	5.98	7.24	0.17	8	7	0.20	8.12	23	243	29731	67	ND	136	31	ND	135	BDL	189	10522
140H73001	17.31	17.32	9.53	41.17	67764	5.98	7.24	0.17	8	7	0.20	8.12	23	243	29731	67	ND	136	31	ND	135	BDL	189	10522
140H73001	17.32	17.33	9.53	41.17	67764	5.98	7.24	0.17	8	7	0.20	8.12	23	243	29731	67	ND	136	31	ND	135	BDL	189	










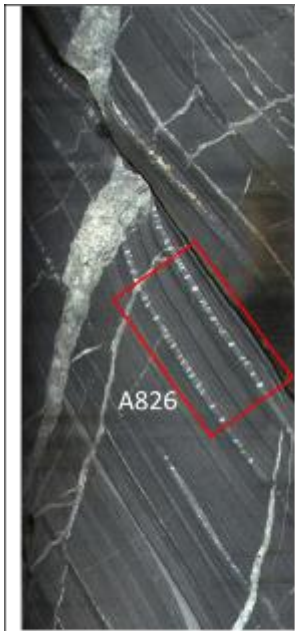


APPENDIX D: HAND SAMPLE PETROLOGY

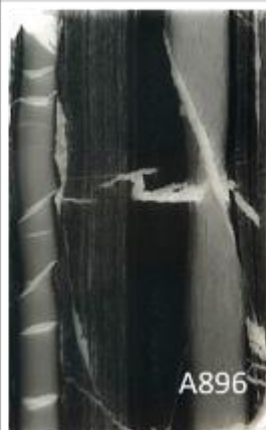
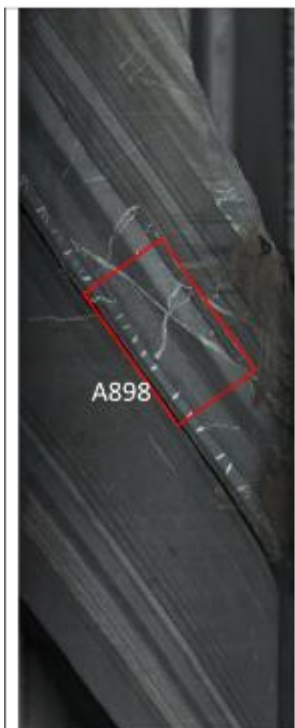
A- SAMPLES

PHOTO	THIN SECTION	COMMENT
 <p>A616_1</p>	 <p>A616_1</p>  <p>A616_2</p>	<p>Sample A616_1 There is a white calcite dominated vein with fine calcite matrix and larger calcite crystals (Figure 1), which stems from the upper boundary of the 'tmb' and cross-cuts the entire bed and 5cm below unlike the cross fracture beds that terminate at the base of the bed. There is a strong presence of pyrrhotite at the lower boundary within a light grey bed, also composed of calcite and patches of fine grained groundmass (Figure 2). This light grey bed has characteristic vein textures, but appears to be a bed that has been altered due to the presence/ inclusion of relatively similar groundmass that is found throughout the rest of the sample (Figure 2 and 3). Pyrrhotite mineralisation also occurs as infill within cross-fractures of the weakly defined upper boundary. Cross-fractures are composed predominantly of calcite, in this sample they lack continuity through the entire bed (Figure 4 and 5), and in the hand sample cross-fractures appear to continue through the entire tmb. They are up to 3mm thick at upper boundary and thin out towards lower boundary. The ground mass is very fine, hard to determine in optical microscopy (Figure 6).</p> <p>Sample A616_2 captures two potential TMBs. Mineralisation of pyrrhotite is pervasive throughout the sample, appearing to occur laterally along bedding planes (Figure 7, 8 and 9). It also laterally transects calcite cross-fractures, and overprints some veins to a large degree. This supports the notion introduced from Sample A616_1, that some mineralisation post-dates the cross-fracture beds, which in turn, postdate deposition of the fine grained groundmass. Pyrrhotite also flares upwards in needle-like pattern (figure 7, 8 and 9). Coarse grained pyrite also appears to occur along bedding planes, some grains are rimmed with calcite on opposite sides of the mineral (figure 10) and some appear to be associated with pyrrhotite mineralisation (Figure 8). The groundmass within the 'tmb' is very fine grained, with calcite grains incorporated/overprinting the groundmass texture. There is defined differentiation between light and dark layers within the groundmass, and in some places it looks like a deformed/slightly folded schistose fabric (figure 12). The same groundmass is also identified outside of the 'tmb' with interlayering of light and dark (figure 11).</p>



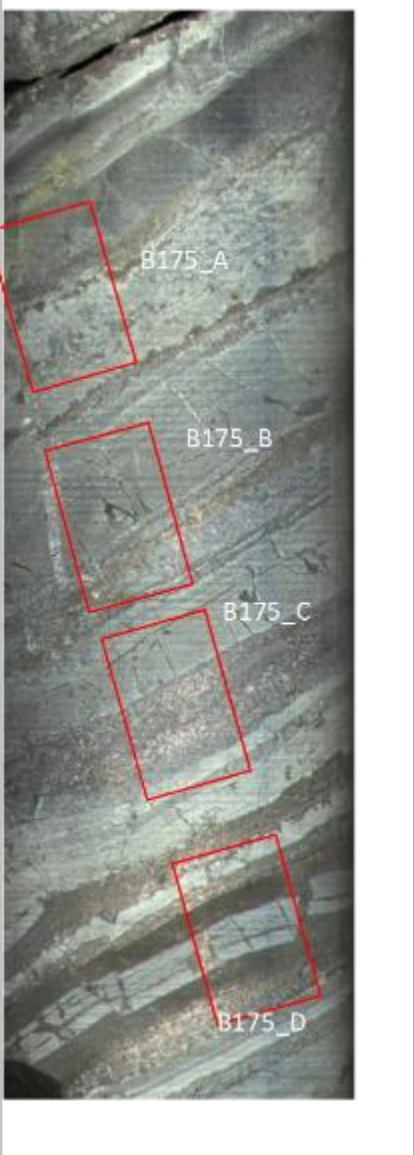



Sample A_826 Several layers of fine grained pyrite exist in this sample (Figure 67 and 68), interbedded with fine grained groundmass of relatively light coloured composition (Figure 71). This is the same fine grained light coloured groundmass is found within the 'tmb' that has cross-fractures running through the layer and stopping abruptly at the boundaries. The cross-fractures are distinctive in hand sample and in thin section. Infill of calcite is predominant and appears to buldge within the bed with a distinctive vein though the middle and other calcite growing laterally (Figure 72). These terminate at the lower and upper boundaries, which are somewhat marked by pyrite mineralised bands (Figure 73). Both beds with cross-fractures appear relatively similar, no noticeable difference in grain size, however, the left-hand side cross-fractures are more distinctive/consistent throughout the bed (Figure 76). Larger calcite veins exist, one offsets the tmb on the left (Figure 74) but not the right, where the vein appears to transect the tmb and continue either side (Figure 75).



This whole sample is K enriched, however there is only one potential TMB observed.

Sample A_898. The groundmass in this sample appears to be a fabric separating the light and dark grains (Figure 78). Dark layering is not pyrite rich, as the heavier dark layers are non-reflective (Figure 79). Some lateral calcite layers are present, but aren't mistaken for light coloured groundmass due to the coarse grain size (Figure 77). The left hand side tmb appears to grade in colour from dark at the boundaries to lighter in the middle (Figure 80). This does not appear to be a change in grain size but a change in composition potentially. The main difference between the two tmb's is the cross-fractures, the left, has distinctive fractures/vein infill of calcite at high angle that terminate sharply at the boundaries, whereas the right has one vein that cross-cuts at a very low angle. The groundmass in both tmb's appears to be relatively similar (Figure 81). Coarse grained pyrite has grown in horizontal veins and other buldging calcite veins (Figure 82), however, no other mineralisation was observed.

CORE SAMPLE	THIN SECTION SAMPLE	COMMENT
		<p>Sample B175-A The base of the sample appears to coarsen upwards in hand sample, and is only very slightly noticeable in thin section, although it is so fine grained it is hard to determine whether it is coarsening or just increasing in darker grains that give the appearance. Figure 1 appears to decrease in darker grains to a lighter (colour) fine groundmass pictured in figure 2. The lower pyrrhotite rich band appears to be alteration of existing groundmass, as there are several pockets of very fine groundmass being overprinted by pyrrhotite and also what was interpreted to be biotite, within a quartz/calcite matrix (Figure 7). There are several calcic veins that cross cut this layer and the lower part of the thin section and in areas of mineralisation there are some inclusions within the vein (Figure 8 and 9). The middle layer also appears to fine upwards, and in thin section there is a noticeable difference in grain size from the base of the layer, to the middle (Figure 10 and 11). Towards the top of the layer there are horizontal veins that have biotite rims infilled with quartz and some specks of pyrrhotite (Figure 3 and 4). The heavy pyrrhotite rich band towards the top of the thin section, is encased by calcite and some quartz (figure 21). There is no presence of groundmass in this layer, unlike the lower layer. A calcite vein cross-cuts the layer on the left-hand side of the section. Within this, Spinel was observed to overprint pyrrhotite (Figure 4 and 5). High relief, brown/reddish in ppl, and isotropic in xpl. The upper part of the thin section transitions from calcite rich to fine light coloured groundmass, with minimal inclusion of darker grains, apart from a somewhat random distribution of overprinting pyrrhotite.</p> <p>Sample B175-B The groundmass at the base of the sample is fine grained and dominantly lighter coloured grains with minor darker grains (Figure 87). There doesn't appear to be a change in grain size throughout the bed, before it reaches the contact with calcite and heavily mineralized zone. This zone has pyrrhotite disseminated throughout along with a scattering of fine galena (grey-ish colour in reflected light) (Figure 84, 86). There are several areas where pyrrhotite extends below into the fine groundmass, indicating it is not deposition/ bedding and has come after. There is a wide dominantly calcite vein that cross-cuts the whole sample, which appears to off-set the lower mineralised zone. This vein could have been a source of fluid and minerals for precipitating along this plane. There is little mineralisation throughout the rest of the vein, only minor pyrrhotite and galena, which supports that this vein could have supplied these minerals to the area (Figure 100, 101). At the top of the sample there is another heavily mineralised zone, the calcite vein may have been the source of this too, as there is no clear sign to indicate the vein post-dates mineralisation (Figure 102, 103). There are several very thin veins that stem from the upper mineralised layer and thin downwards, infilled with calcite, and some are heavily galena and/or pyrrhotite rich (Figure 104, 105, 106). The groundmass directly above the lower mineralised zone transitions back to the fine grained groundmass found at the base of the</p>



Sample B175-A The base of the sample appears to coarsen upwards in hand sample, and is only very slightly noticeable in thin section, although it is so fine grained it is hard to determine whether it is coarsening or just increasing in darker grains that give the appearance. Figure 1 appears to decrease in darker grains to a lighter (colour) fine groundmass pictured in figure 2. The lower pyrrhotite rich band appears to be alteration of existing groundmass, as there are several pockets of very fine groundmass being overprinted by pyrrhotite and also what was interpreted to be biotite, within a quartz/calcite matrix (Figure 7). There are several calcic veins that cross cut this layer and the lower part of the thin section and in areas of mineralisation there are some inclusions within the vein (Figure 8 and 9). The middle layer also appears to fine upwards, and in thin section there is a noticeable difference in grain size from the base of the layer, to the middle (Figure 10 and 11). Towards the top of the layer there are horizontal veins that have biotite rims infilled with quartz and some specks of pyrrhotite (Figure 3 and 4). The heavy pyrrhotite rich band towards the top of the thin section, is encased by calcite and some quartz (figure 21). There is no presence of groundmass in this layer, unlike the lower layer. A calcite vein cross-cuts the layer on the left-hand side of the section. Within this, Spinel was observed to overprint pyrrhotite (Figure 4 and 5). High relief, brown/reddish in ppl, and isotropic in xpl. The upper part of the thin section transitions from calcite rich to fine light coloured groundmass, with minimal inclusion of darker grains, apart from a somewhat random distribution of overprinting pyrrhotite.



Sample B175-B

The groundmass at the base of the sample is fine grained and dominantly lighter coloured grains with minor darker grains (Figure 87). There doesn't appear to be a change in grain size throughout the bed, before it reaches the contact with calcite and heavily mineralized zone. This zone has pyrrhotite disseminated throughout along with a scattering of fine galena (grey-ish colour in reflected light) (Figure 84, 86). There are several areas where pyrrhotite extends below into the fine groundmass, indicating it is not deposition/ bedding and has come after. There is a wide dominantly calcite vein that cross-cuts the whole sample, which appears to off-set the lower mineralised zone. This vein could have been a source of fluid and minerals for precipitating along this plane. There is little mineralisation throughout the rest of the vein, only minor pyrrhotite and galena, which supports that this vein could have supplied these minerals to the area (Figure 100, 101). At the top of the sample there is another heavily mineralised zone, the calcite vein may have been the source of this too, as there is no clear sign to indicate the vein post-dates mineralisation (Figure 102, 103). There are several very thin veins that stem from the upper mineralised layer and thin downwards, infilled with calcite, and some are heavily galena and/or pyrrhotite rich (Figure 104, 105, 106). The groundmass directly above the lower mineralised zone transitions back to the fine grained groundmass found at the base of the sample (Figure 95). Above, there is a rather abrupt transition to finer grained darker groundmass (Figure 96), that gradually grades upwards to a lighter coloured groundmass. There is a series of these grading sequences, however, much more subtle than the first (Figure 97). Hard to tell if grain size changes or just a compositional change. Towards the middle/second half of the sample, the groundmass is more homogenous, very fine with even distribution of light and dark grains. (Figure 107). Biotite is randomly distributed in this sample, some is found scattered within the upper mineralised zone and some coarse grains are found within the fine groundmass of the homogenous layer (outside of the large vein (Figure 99).

Sample B175 – C the base of the thin section is composed of coarser K-feldspar, with chlorite forming along planes and lots of mineralisation including pyrrhotite and galena fine grained pyrite and rutile (within k-feldspar grains) (Figure 151, 153). At the top of this complex layer, chlorite is present with pyrrhotite and k-feldspar along the contact with a very fine grained



Sample B208 This dark grey bed has sharply defined boundaries with white-light grey cross fractures that mostly terminate sharply at the lower boundary, but some extend above the bed- indicating they are veins opposed to cross fractures, it's hard to distinguish which fractures are inherent feature of the bed in this sample. The left edge of the thin section is a very fine groundmass composed of majoritively dark grains, however there is a stark contrast with the edge layer and the thicker black bed on the left-hand side of the thin section (figure 27). This layer is coarser grained and darker in grain composition, however this appearance may be attributed to the grain size. There are several calcic veins within the lighter edge layer, which are offset at the boundary with the darker layer (figure 27). These veins through the dark layer give the appearance of 'cross fractures' but may not be as they do not terminate at the boundary of the 'tmb'. Through the dark layer on the left/top of the thin section, the veins have chalcopyrite mineralisation. The 'vein-like' layer through the middle of the thin section is mainly composed of calcite and K-feldspar with pyrrhotite (figure 36 and 37). Some existing fine grained dark groundmass is found within this layer, suggesting this is an alteration texture (figure 39 and 40). The following dark layers within the right-hand side of the thin section are composed of similar fine grained dark groundmass (figure 39, 41, 43 and 44) and are separated by interbeds/alteration/or veins of calcite. Veins also cross-cut across the layers (figure 41, 42 and 44). Pyrrhotite has a random distribution, included within calcic veins as well as cross-cutting/overprinting darker layers.



Sample B218 The base is very fine grained groundmass with relatively even ratio of dark and light grains (too fine to see what they are) (Figure 46). There is no appearance/noticeable change in grain size throughout the bottom layer (if so only slight change in light and dark mineral composition-but not significant. Several calcite veins start/finish at the base of the thin section (figure 46). Very thin veins with some pyrite mineralisation (Figure 48 and 49). Opaque and non-reflective mineral is observed within this sample which is thought to be ilmenite (non-magnetic in hand sample). It can be seen to infill veins (Figure 50, 51 and 52). One calcite vein stemming from the bottom of the thin section, transitions to opaque mineral infill and back to calcite several times throughout the sample (Figure 53, 54, 55) This occurs in other veins that appear to terminate at the boundaries of layers (giving the appearance of cross-fractures) but actually continue throughout the entire/part of the sample. There are several bands of fine grained pyrite (Figure 56) along bedding that are interlayered with light, fine grained groundmass (Figure 57). The groundmass at the top of the thin section is much the same as the rest of the sample (Figure 58) although, possibly slightly coarser than the basal layer (Figure 46).

APPENDIX E: THIN SECTION PETROLOGY

A616 – 1

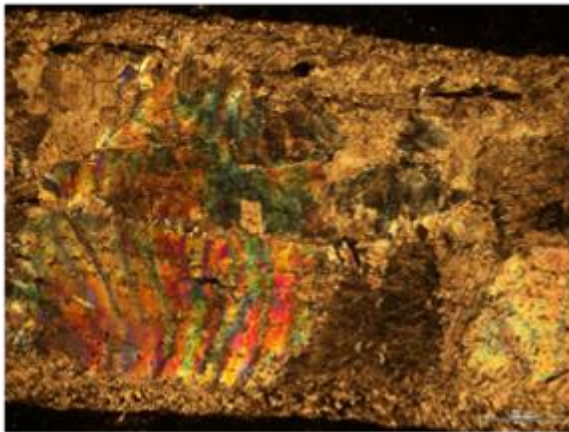


Figure 1. Calcite vein, some larger calcite crystals within fine grained mass. This vein is a large cross-cutting vein through the entire sample, with minimal mineralisation.

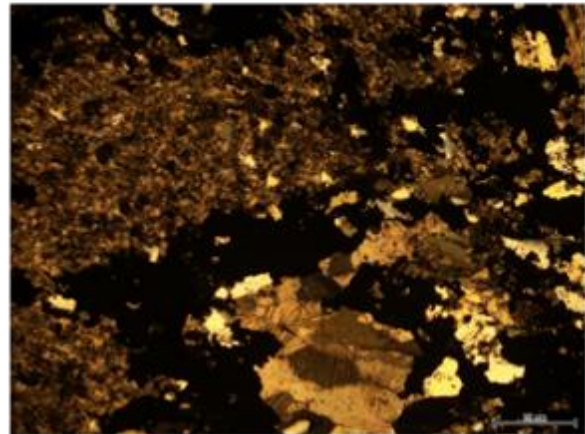


Figure 2. Strong presence of pyrrhotite at the lower boundary within a light grey bed, also composed of calcite and patches of fine grained groundmass.

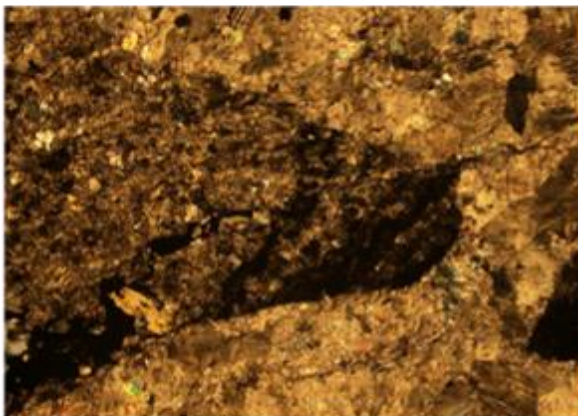


Figure 3. Vein of interlocking calcite that has overprinted the darker groundmass but this triangular piece of groundmass remains as an inclusion within the vein/ resisted alteration/ fluid passing through.

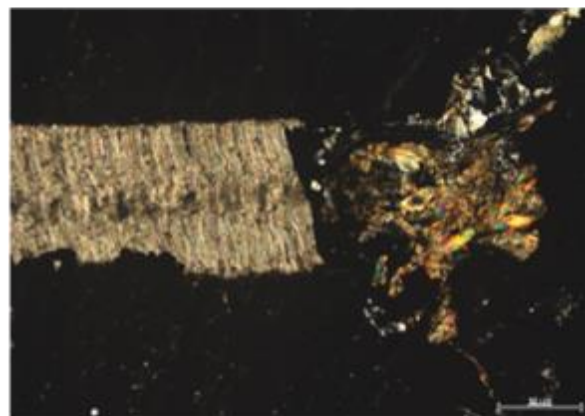


Figure 4. Calcite veining that starts (as you can see here) and terminates sharply, but appears to have adjoining relationship with other veins below (not pictured). Very fine dark groundmass- too fine to see.

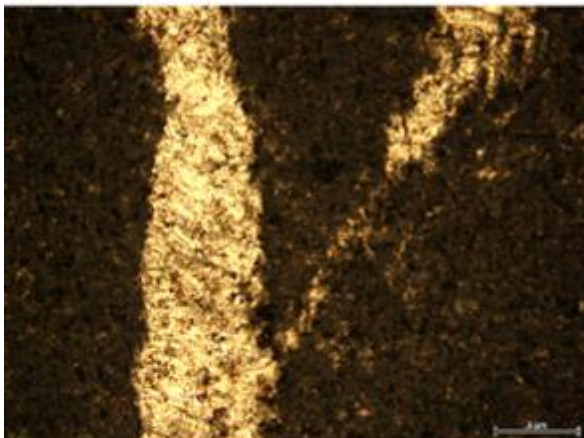


Figure 5. Very dark, fine groundmass, with cross-cutting calcite veins, the right-hand side vein appears to branch off the thicker vein to the left.

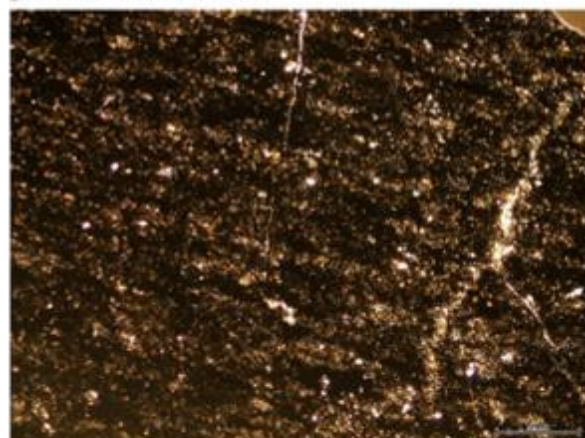


Figure 6. Very fine, dark groundmass too difficult to identify minerals. Thin calcite veins occur with potentially some alteration along what appears to be bedding planes within the groundmass.

A616 – 2

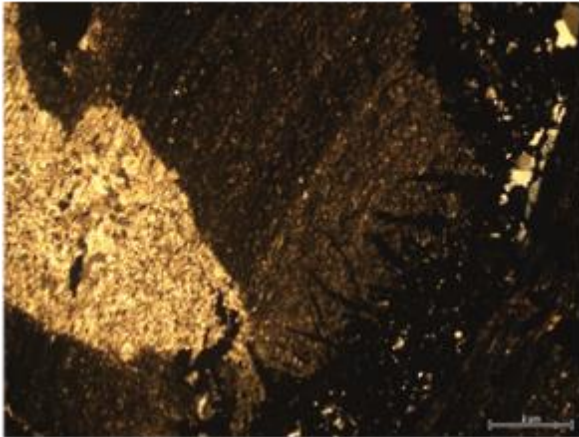


Figure 7. Very fine grained groundmass, with a coarser grained mineral light coloured (unidentified). Pyrrhotite occurs in needle-like shapes along the bedding plane, expanding upwards. Pyrite also appears to be associated with the pyrrhotite mineralisation, however, it is difficult to determine. Some pyrrhotite has overprinted the larger crystal, suggesting mineralisation came later.

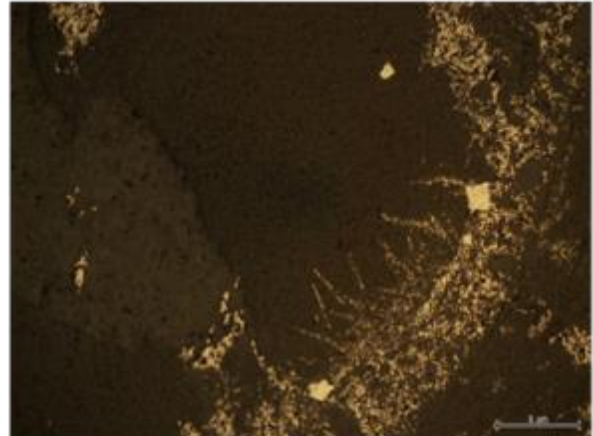


Figure 8. Reflected light image of Figure 7, showing pyrrhotite appearing as needles and coarse grained pyrite along bedding planes.

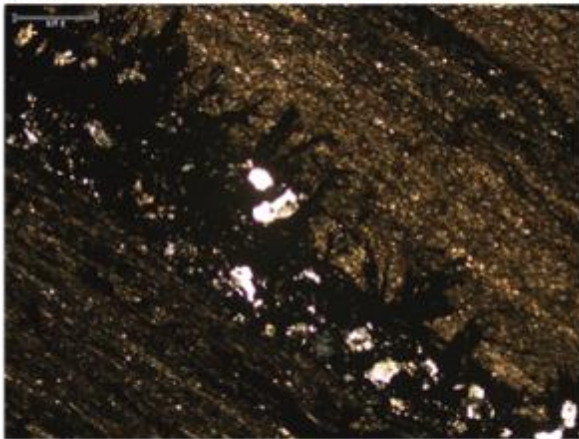


Figure 9. Similar texture along same boundary/bedding plane as figure 14/15. Calcite is present, but hard to define relationship with pyrrhotite and calcite, which came first. Very fine grained groundmass, with some darker layers separated by lighter layers.

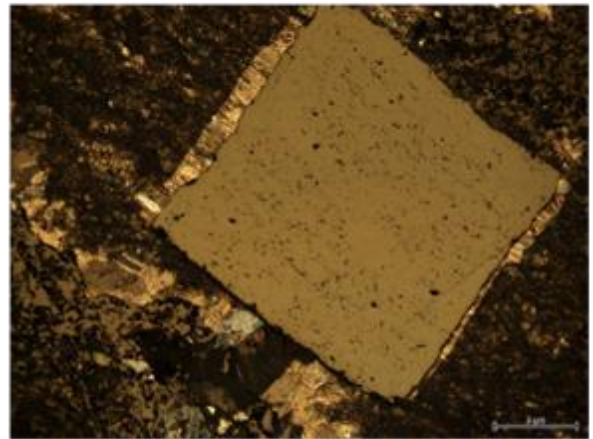


Figure 10. Coarse pyrite grain rimmed on two sides by calcite, within a fine grained groundmass. A layer of coarser calcite below the pyrite with disseminated pyrrhotite throughout.

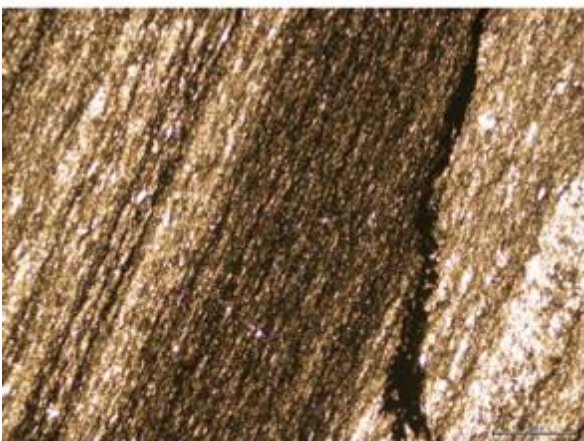


Figure 11. Similar interlayering texture of the groundmass within the 'tmb' exists outside, with alternative light and dark layers. Gives the appearance of a fabric.

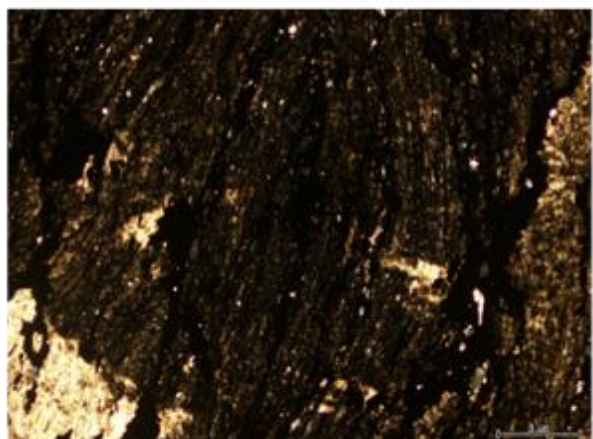


Figure 12. Very fine grained groundmass, which appears to have a foliation, with layers of light and dark defined. It also appears to be slightly deformed/folded or have a schistose fabric (?). Calcite also appears to overprint the groundmass and is in turn overprinted by pyrrhotite.

A649 – 1



Figure 20. Similar groundmass composition exists in this sample, as has been seen in A616, however, it does not appear as a fabric of interlayered light and dark minerals- rather a random mass. Very fine grained, SEM detected as dolomite.

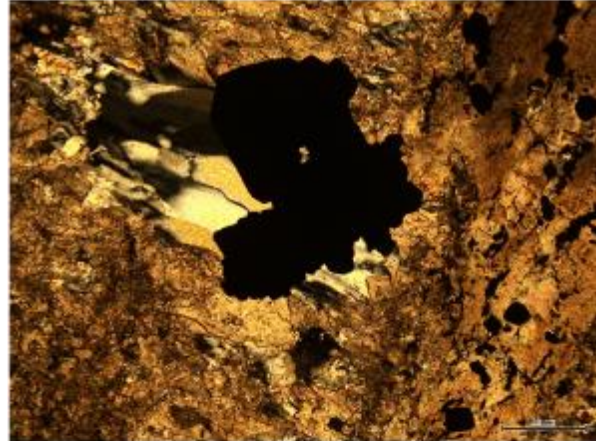


Figure 23. High relief pyrite that appears to overprint coarse grained calcite and the finer calcite (?) mass infill within a cross-fracture. Mineralisation appears to have occurred after initial infill of cross-fracture.

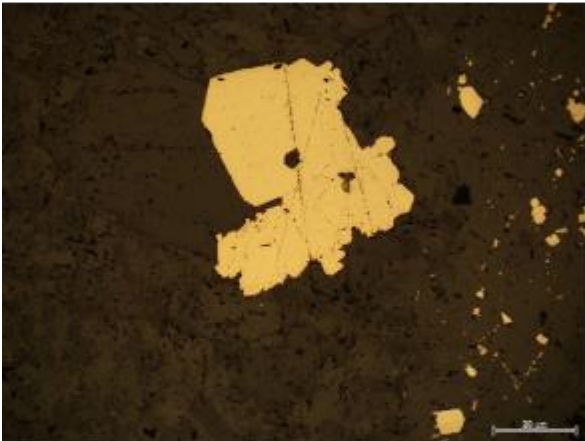


Figure 34. Reflected light image of figure 23 showing pyrite.

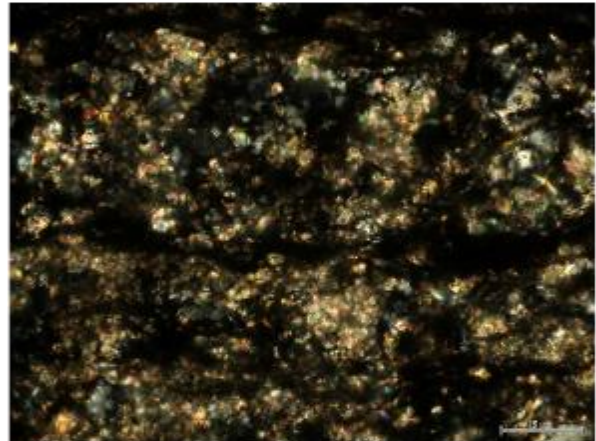


Figure 26. Groundmass outside of 'tmb' is composed of much darker, minerals, still in a random arrangement. Too fine to

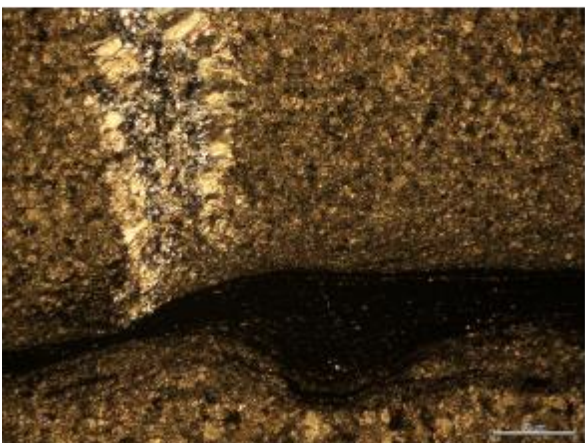


Figure 27. The two 'tmb's are separated by this dark layer forming the boundary between them. Very fine grained, only minor presence of sulphides (figure 28) and appears to have been deformed, with bulges upwards and downwards of the bedding plane. The cross-fracture vein on the left hand side of the upper tmb, appears to separate into two branches towards the base. It is hard to differentiate if it does separate and there is groundmass in between or if it is still vein infill.



Figure 28. Reflected light image of figure 27.

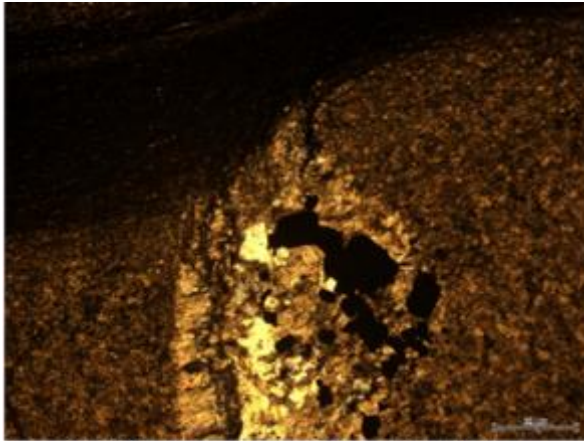


Figure 29. High relief pyrite overprinting calcite infill of cross-fracture within the fine grained groundmass of the tmb. The cross-fracture is terminated/starts sharply at the well-defined boundary with the fine grained dark layer outside of the tmb.29

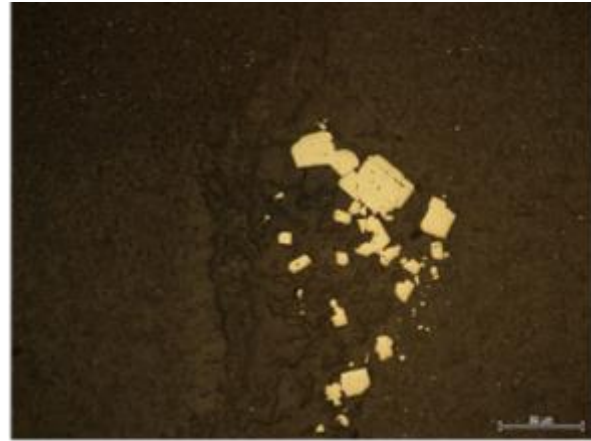


Figure 30. Reflected light image of figure 29 showing high relief, coarse grained pyrite.



Figure 31 Very fine grained groundmass with few inclusions of calcite and a quartz grain. Dominantly dark minerals with some lighter minerals at the top and flecks throughout.

A826

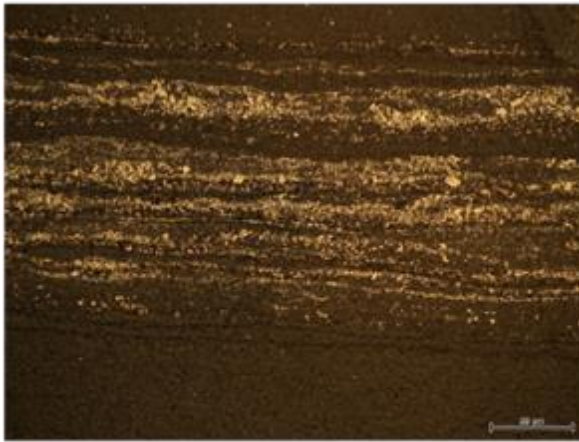


Figure 67. Bands of fine grained pyrite are throughout the sample, look consolidated layers at this magnification but figure 68 shows they are individual grains.

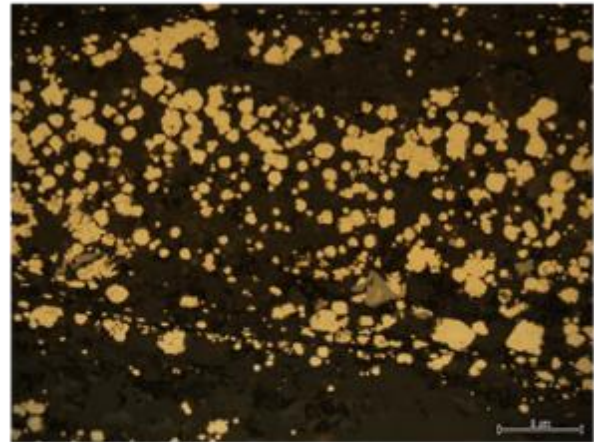


Figure 68. Fine grained pyrite individual grains, figure 67 at higher magnification.

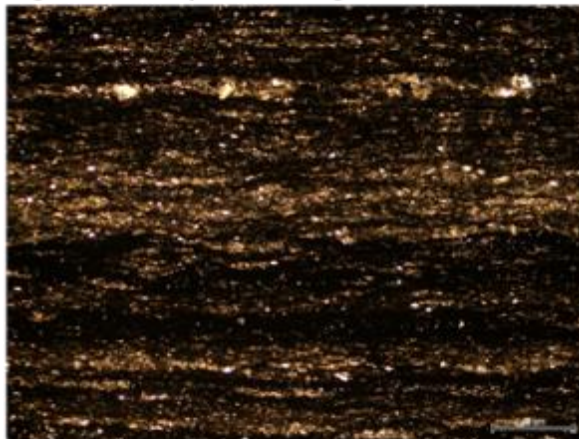


Figure 71. Fine grained pyrite (black) interbedded with lighter fine grained groundmass.



Figure 69. The same fine grained light coloured groundmass is found within the 'tmb' that has cross-fractures running through the layer and stopping abruptly at the boundaries.



Figure 72. Infill of calcite is predominant and appears to bulge within the bed with a distinctive vein through the middle and other calcite growing laterally

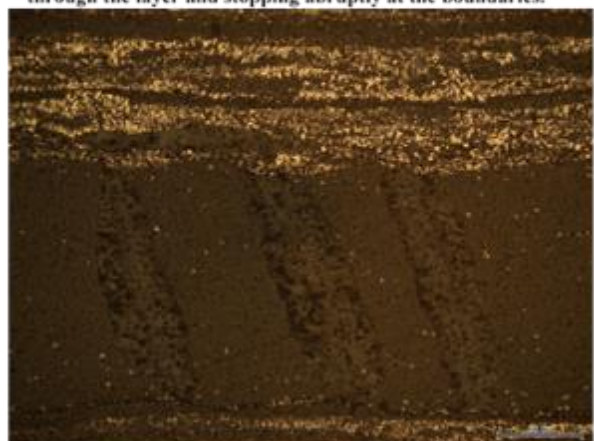


Figure 73. The crossfractures terminate at the lower and upper boundaries, which are somewhat marked by pyrite mineralised bands.

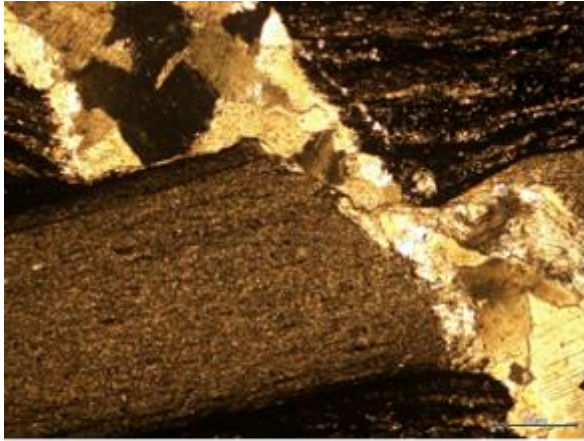


Figure 74. Larger calcite veins exist, one offsets the tmb on the left of the thin section.

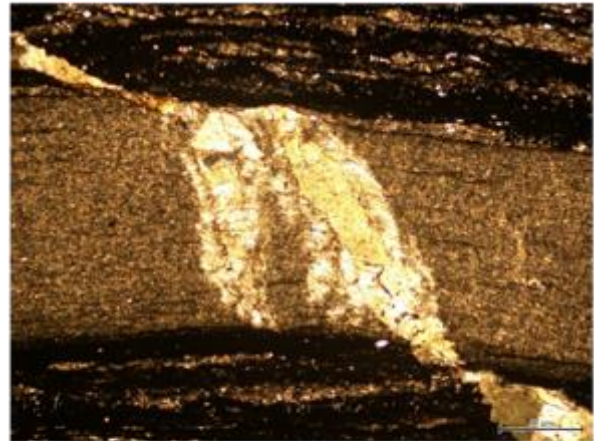


Figure 75. The tmb on the right is not offset by the vein in figure 74, the same vein cross-cuts the bed and continues either side.

A898

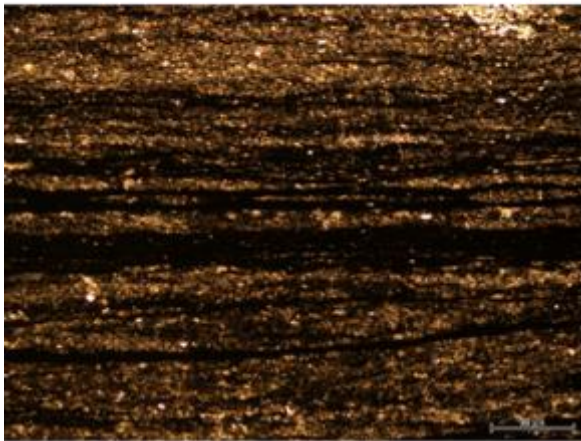


Figure 78. Light coloured groundmass and dark groundmass separated, appears to be a fabric separating the light and dark grains. Dark layering is not pyrite rich, as the heavier dark layers are non-reflective (Figure 84).



Figure 79. Reflected light image of figure 78, showing only small amounts of pyrite, meaning the dark layers are non-reflective groundmass.

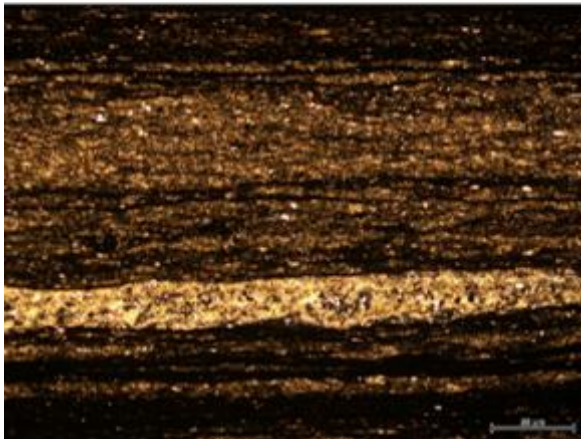


Figure 77. Lateral calcite layers are present, but aren't mistaken for light coloured groundmass due to comparatively coarse grain size.



Figure 80. The left hand side tmb appears to grade in colour from dark at the boundaries to lighter in the middle. This does not appear to be a change in grain size but a change in composition potentially.

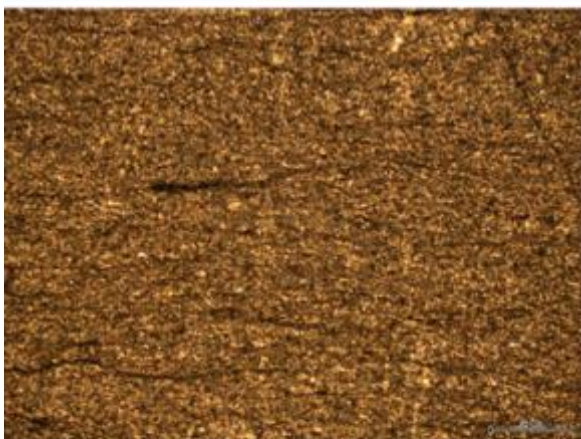


Figure 81. The groundmass in both tmb's appears to be relatively similar, pictured is the right-hand side tmb.

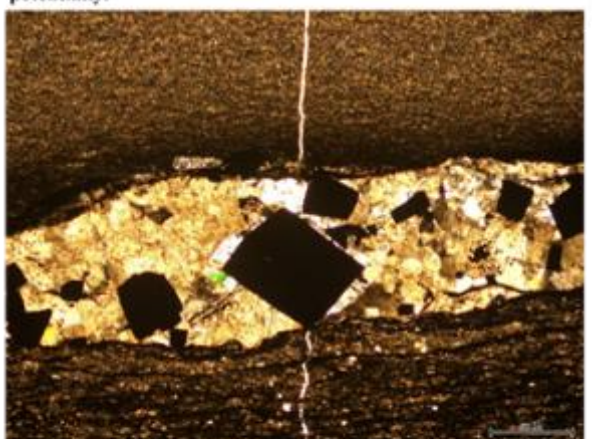


Figure 82. Coarse grained pyrite has grown in horizontal veins and other bulging calcite veins, however, no other mineralisation was observed.

B175 – A



Figure 1. The very bottom of the sample appears to coarsen upwards in hand sample, and is only very slightly noticeable in thin section, although it is so fine grained it is hard to determine whether it is coarsening or just increasing in darker grains that give the

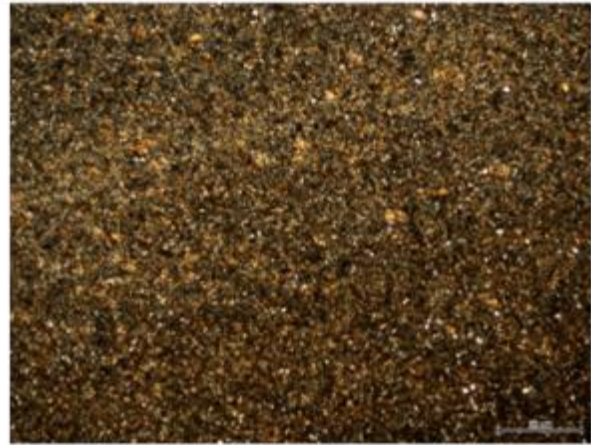


Figure 2. Above figure 5 in hand sample appears to fine upwards, however again, in thin section it appears to just be the decrease in darker grains.

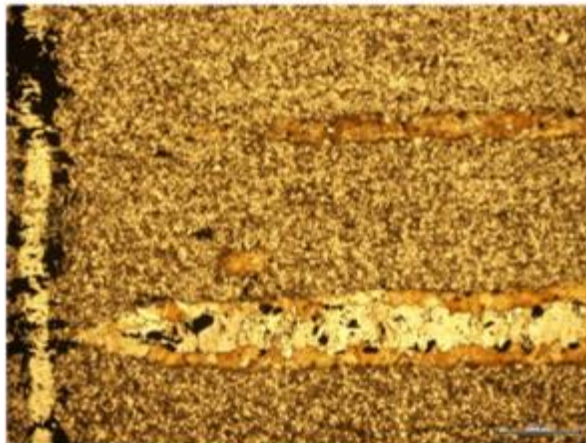


Figure 3. Horizontal vein with K-feldspar showing simple twinning, rimmed with biotite and with inclusions of pyrrhotite. Vertical calcite vein with pyrrhotite mineralisation also, but no presence of biotite. Fine grained groundmass.

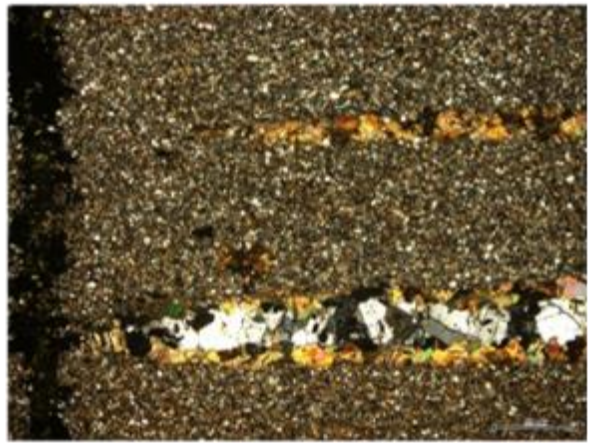


Figure 4. Figure 3 in XPL.

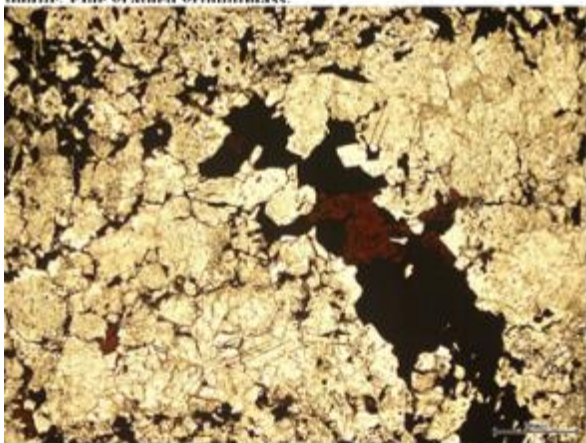


Figure 5. Interpreted to be rutile within/overprinting pyrrhotite. High relief, brown/reddish in ppl, and isotropic in xpl. Formed within wider cross-cutting vein of calcite and a layer enriched in pyrrhotite mineralisation.

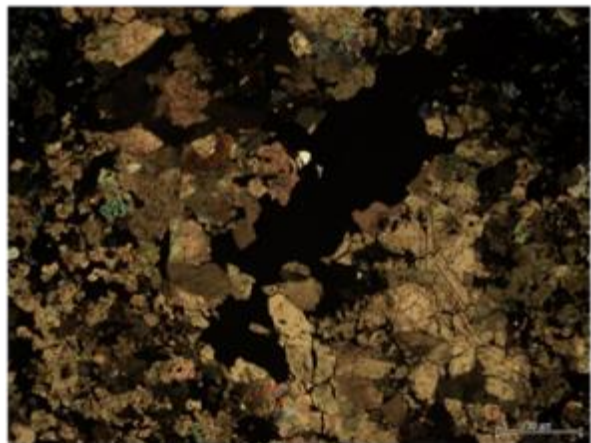


Figure 6. Same sample as 01 in XPL. Brown mineral is isotropic, interpreted to be rutile.

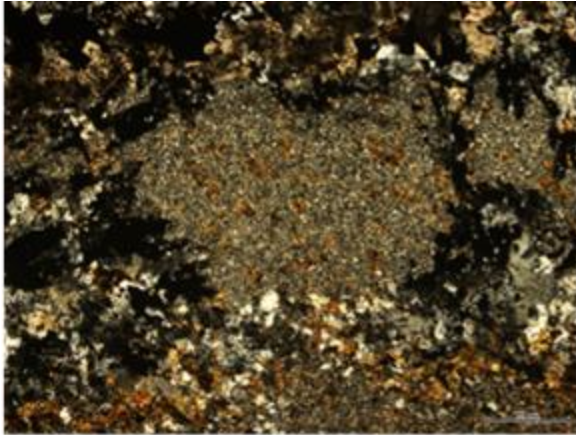


Figure 7. Pocket of very fine groundmass being overprinted by pyrrhotite and also what was interpreted to be biotite, within a quartz/calcite matrix.XPL.

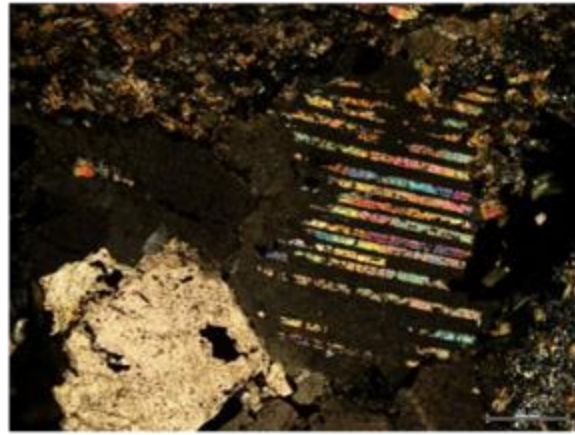


Figure 8. Coarse calcite at the base of a vein at the bottom of the thin section. High birefringence colour (?) at certain angle.

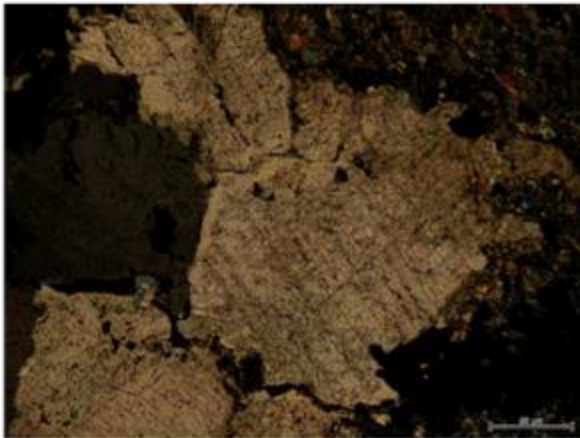


Figure 9. Same as figure 8, rotated 90 degrees in XPL.

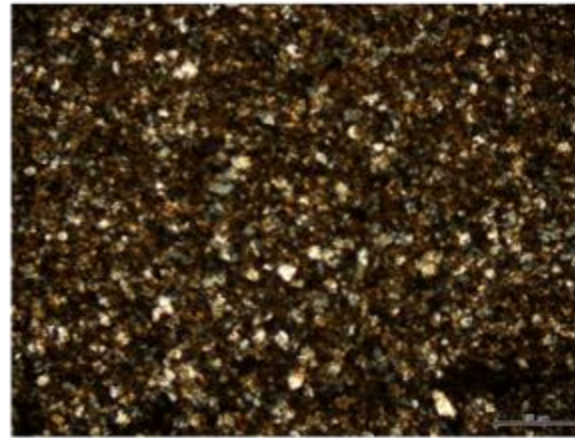


Figure 10. Coarse grained at the base of the middle layer. Noticeable decrease in grain size from figure 13 to 14.

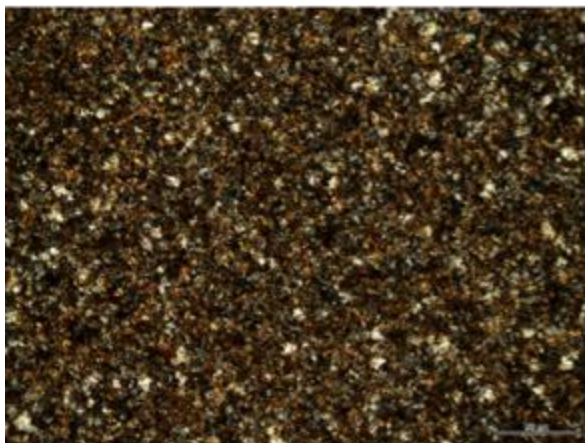


Figure 11. Decrease in grain size from figure 13, appearing to fine upwards within the middle layer of the thin section.

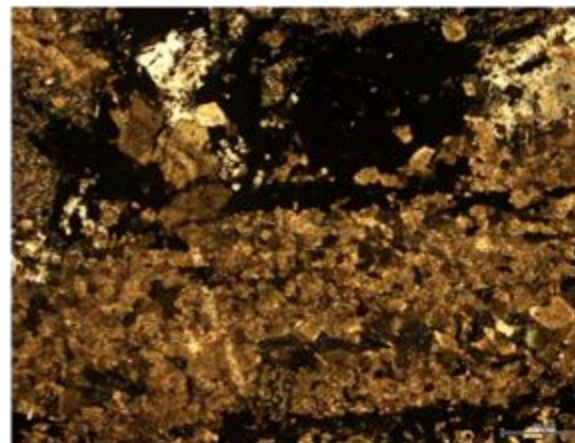


Figure 12. Towards the top of the thin section is pyrrhotite rich band with calcite. No presence of fine grained groundmass as in the lower layer in figure 7.



Figure 13. Reflected light image of figure 12, showing pyrrhotite.

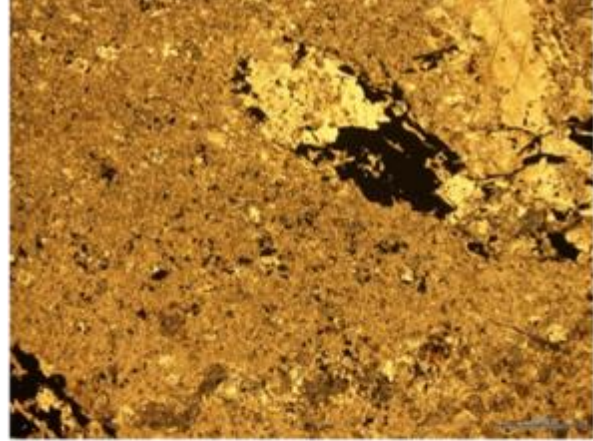


Figure 14. The very top of the thin section, very fine grained groundmass, with hardly any darker grains, apart from pyrrhotite. Calcite grains have been overprinted by pyrrhotite.

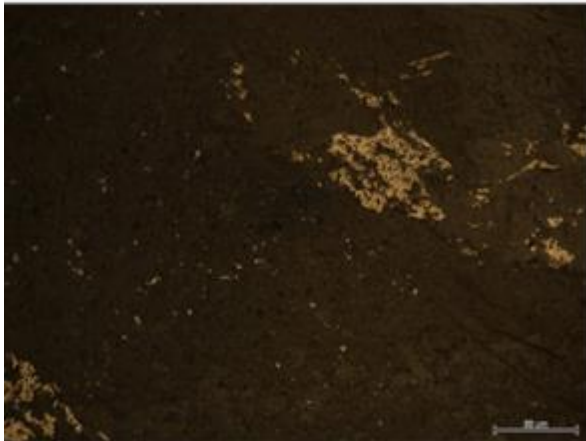


Figure 15. Reflected light image of figure 14 showing pyrrhotite.

B175 – B

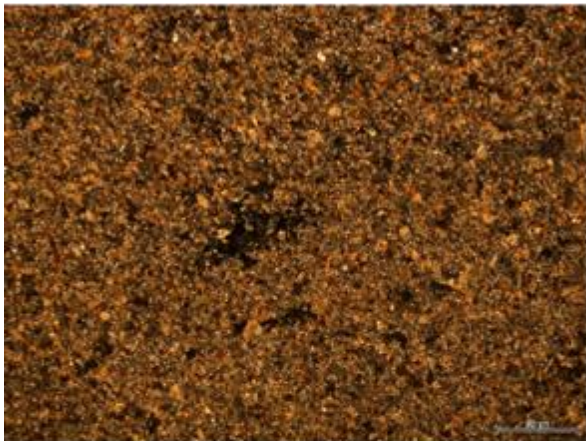


Figure 87. Fine grained groundmass at the base of the sample, dominated by lighter grains, with a small random distribution of darker grains.

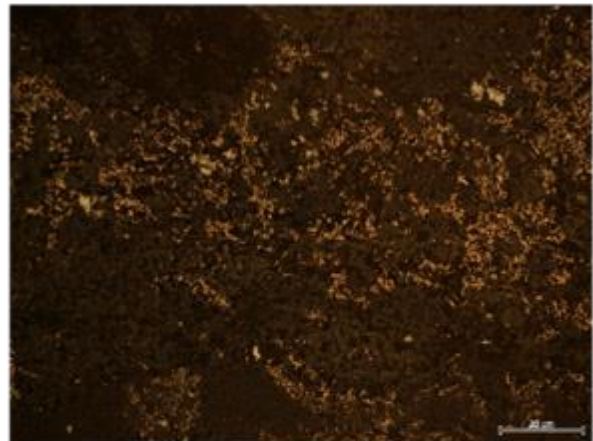


Figure 84. Disseminated distribution of pyrrhotite, does not look bedded. Can see slight change in colour/ grey specks throughout, which are galena as shown in Figure 86.

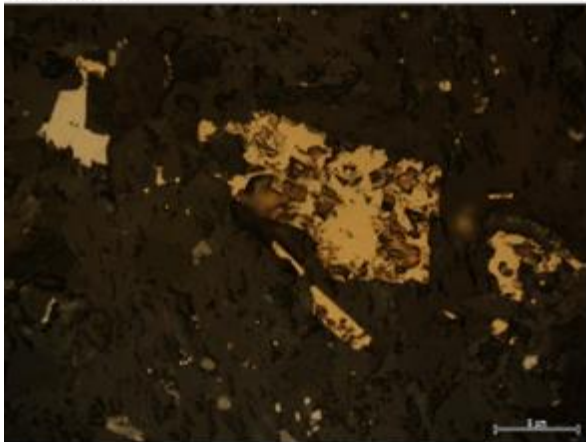


Figure 86. Pyrrhotite yellow-gold colour in reflected light and small grains of galena (top left corner) – grey colour, speckled throughout the lower mineralised zone of the thin section.

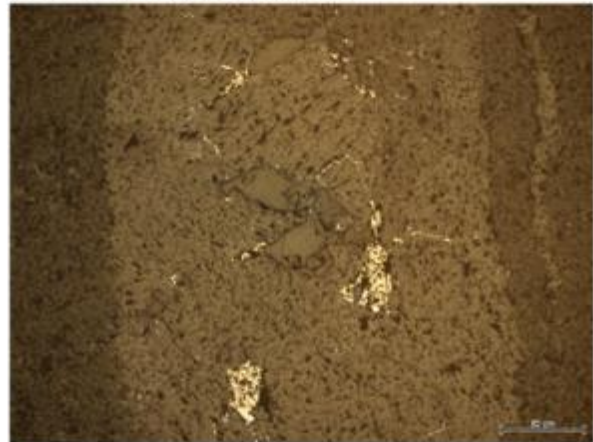


Figure 100. Calcite vein cross-cutting the entire thin section and off-setting the lower mineralised zone. The vein itself has minor mineralisation of pyrrhotite and galena, but may have been the source of these minerals to the lower zone. Reflected light.

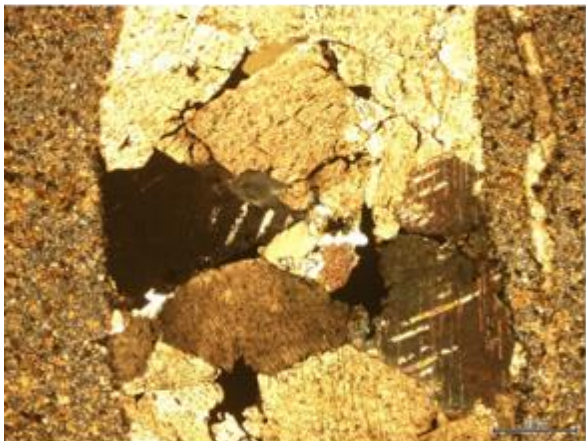


Figure 101. XPL image of figure 100, showing dominantly calcite vein. With minor sulphide mineralisation.

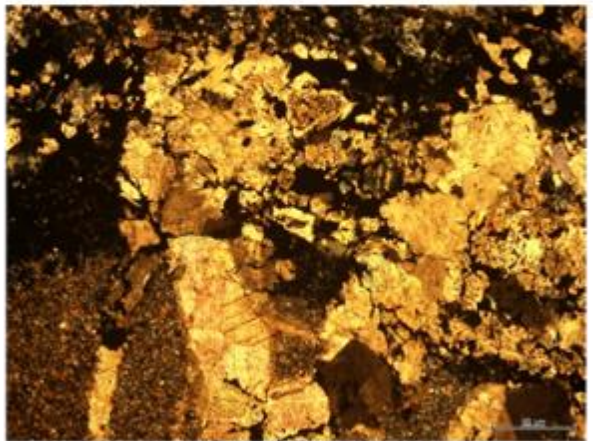


Figure 103. Intersection of large calcite vein with the upper mineralised zone. There appears to be a slight relationship between the more consolidated calcite vein dispersing into more distributed grains throughout the zone. The vein doesn't just overprint the entire zone. XPL.

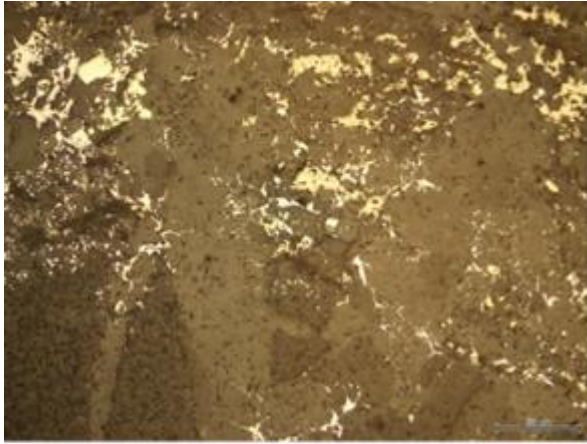


Figure 102. Reflected light image of Figure 103, showing pyrrhotite and galena mineralisation.

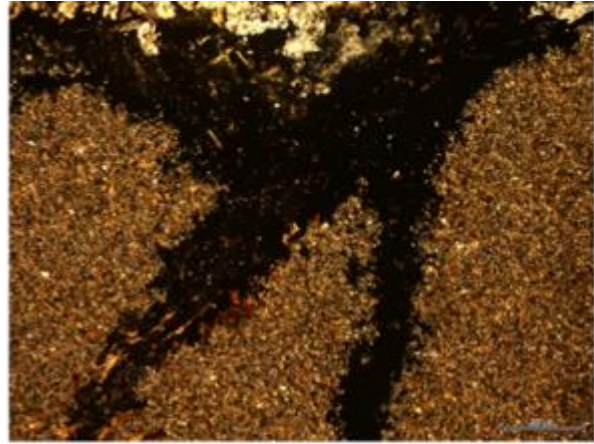


Figure 104. Veins stemming off the upper mineralised zone, dominated by galena and some pyrrhotite. XPL.

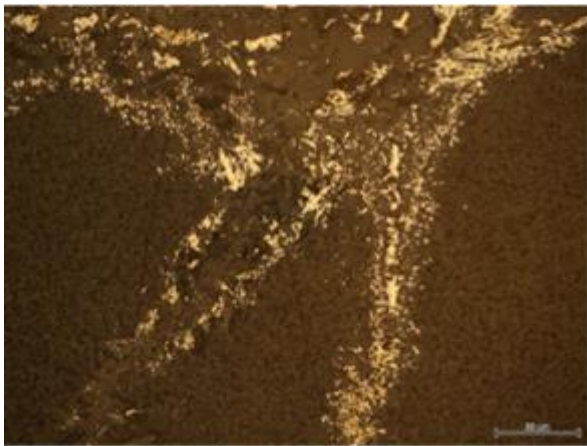


Figure 105. Reflected light image of Figure 104 showing galena and pyrrhotite infilling the veins.

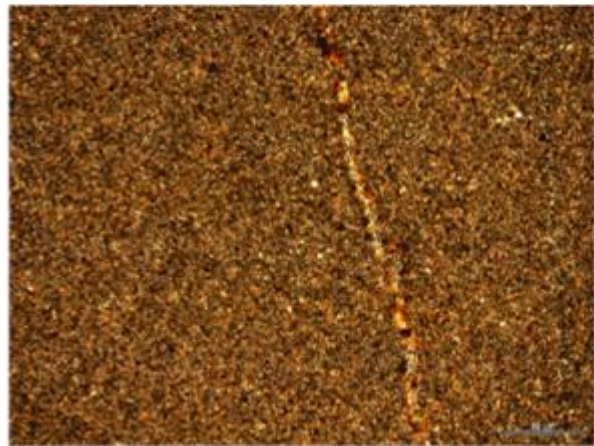


Figure 106. A very fine vein stemming from the mineralised zone, but dominantly calcite (? Too fine to see) possibly feldspar, but unlikely.

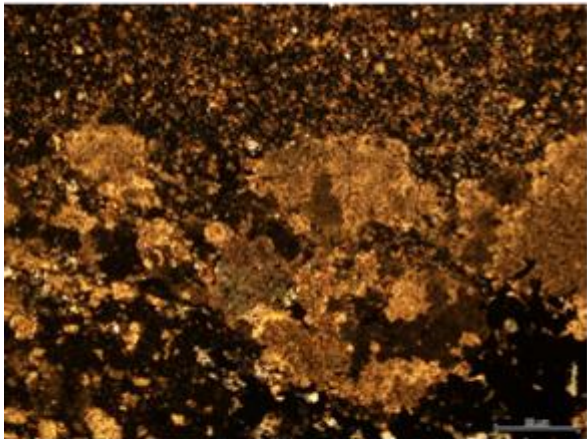


Figure 95. The lower mineralised zone with calcite, transitions to fine grained groundmass with significantly more darker grains than the base of the sample. There is no sharp boundary between the two. XPL.

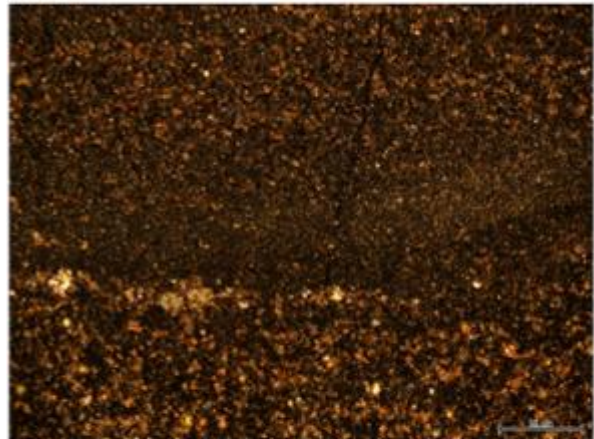


Figure 96. Above figure 95, there is a rather abrupt transition to finer grained darker groundmass (pictured) that gradually grades upwards to a lighter coloured groundmass.

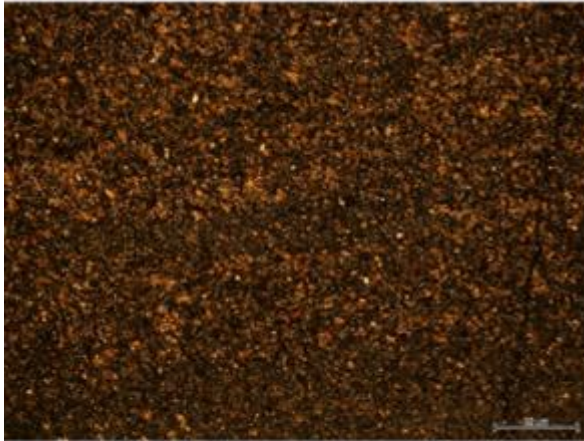


Figure 97. Above figure 96 There is a series of grading sequences from dark to light, however, much more subtle than figure 96.



Figure 107. Towards the middle/second half of the sample, the groundmass is more homogenous, very fine with even distribution of light and dark grains.

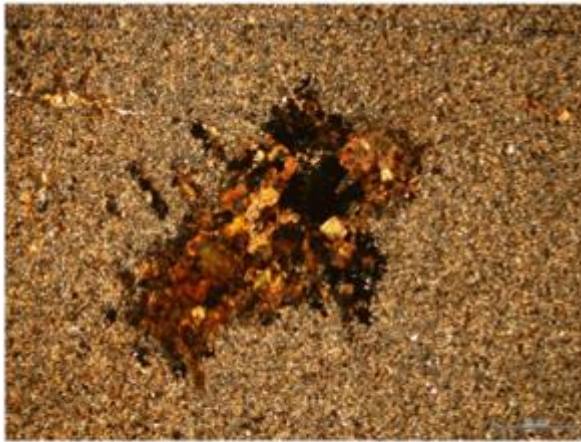


Figure 99. Biotite is randomly distributed in this sample, some is found scattered within the upper mineralised zone and some coarse grains are found within the fine groundmass of the homogenous

B208



Figure 26. Very fine grained and dark groundmass in the thick dark layer on the left-hand side of the thin section.

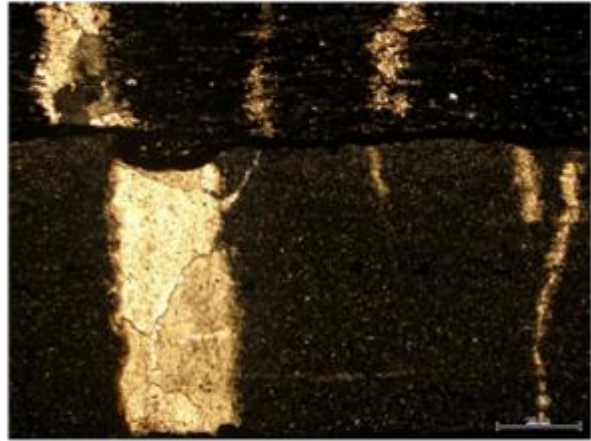


Figure 27. The contrast between the lighter edge layer of the thin section with the dark thick layer on the left-hand side. Despite the difference in colour in hand sample, in thin section both are very dark grained, however, the thicker layer is coarser, perhaps giving it the darker appearance in hand sample. (?) Calcite veins are also offset at this distinctive boundary. Hard to tell if they are offset or if they terminate.

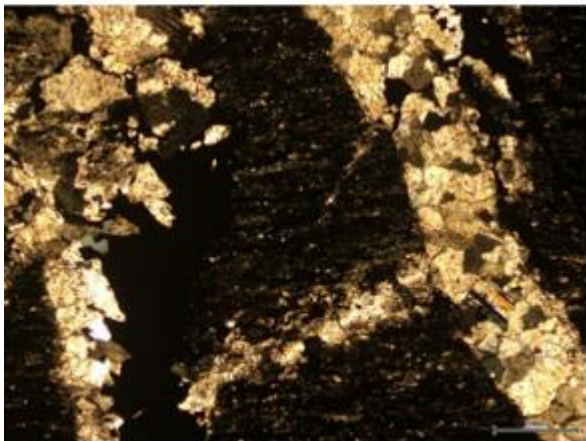


Figure 28. Calcite veins through the thick dark layer host chalcopyrite mineralisation (figure 29).

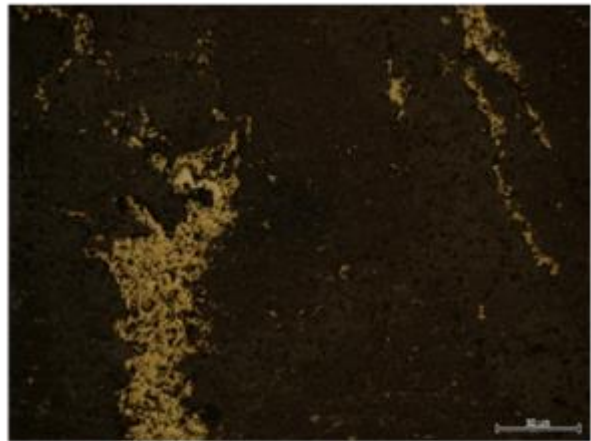


Figure 29. Chalcopyrite mineralisation in calcite vein (figure 28) in reflected light.

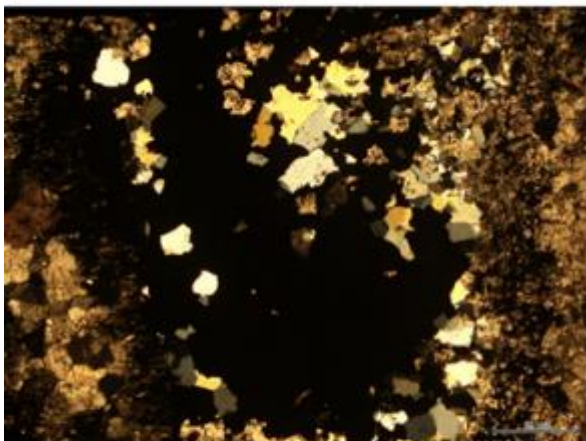


Figure 30. More chalcopyrite in masses within the calcite veins of the dark layer. These veins do not appear to continue into the next layer, however the layer above is gives the appearance it is a vein itself, or an alteration of an existing bed. These two are interpreted to be separate due to the difference in mineralisation (Pyrrhotite in the layer above opposed to chalcopyrite).

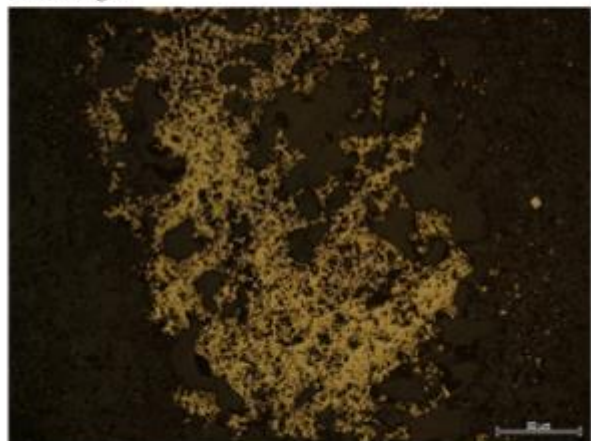


Figure 31. Reflected light image of figure 30 showing pyrrhotite.



Figure 33. The contact of the thick dark fine grained groundmass with the calcic layer with pyrrhotite mineralisation. Small, not well defined calcic veins also visible.



Figure 34. Figure 33 in reflected light. (Unsure what the blocky graded layer is (sulphide?))

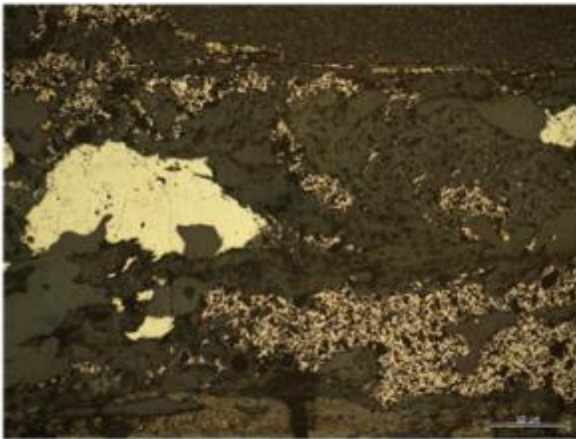


Figure 36. Within the calcic rich layer in the middle of the thin section is pyrrhotite rich, however, other sulphide minerals may exist (or slight variation in reflectance under microscope).

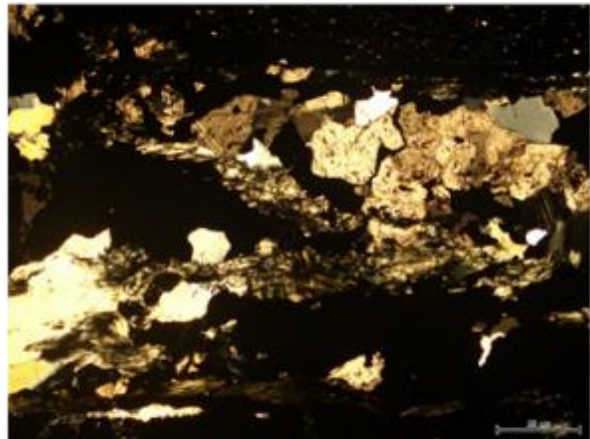


Figure 37. XPL image of figure 36.

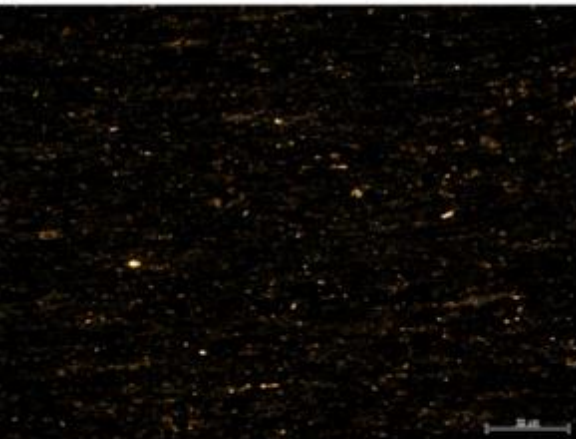


Figure 38. Middle of the thick dark layer, fine grained very dark groundmass.

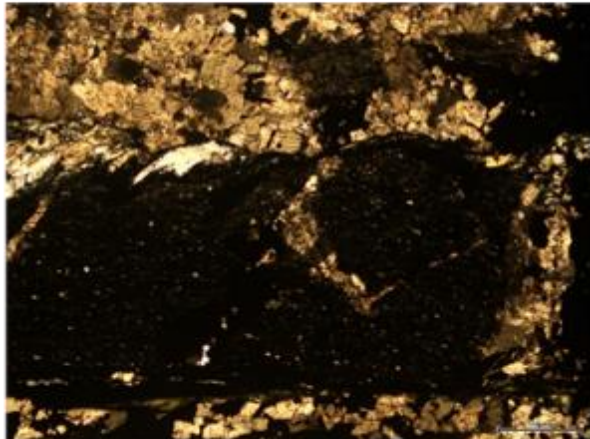


Figure 39. Ground mass of other dark layers within the thin section have similar composition to the thicker layer, suggesting this whole thin section was one, that has been preferentially altered along planes (?)

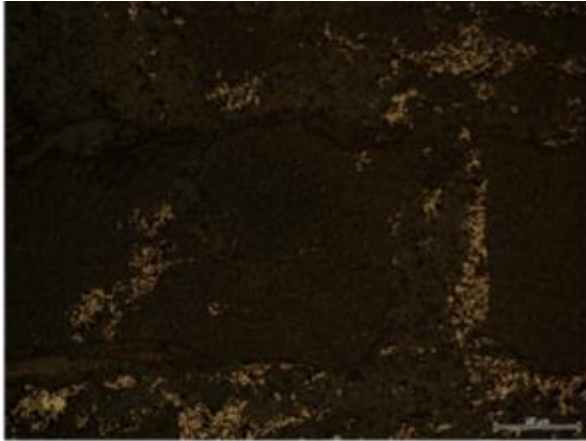


Figure 40. Reflected light image of figure 30, showing pyrrhotite.

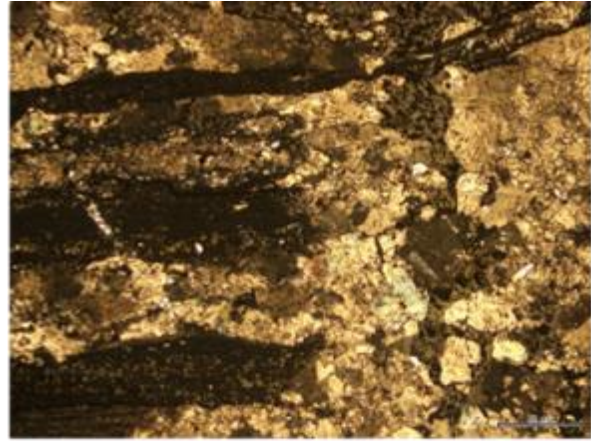


Figure 41. Similar dark groundmass layers disrupted by a calcite vein (vertical) and appears to be interbedded with calcite beds too. In hand sample these look like different genesis however, in thin section, look like they could be a part of the same stage.

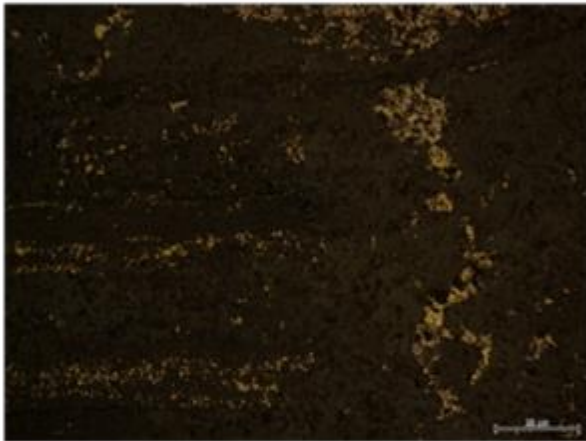


Figure 42. Figure 41 in reflected light, showing some pyrrhotite mineralisation in both vertical and horizontal calcite rich beds/veins.

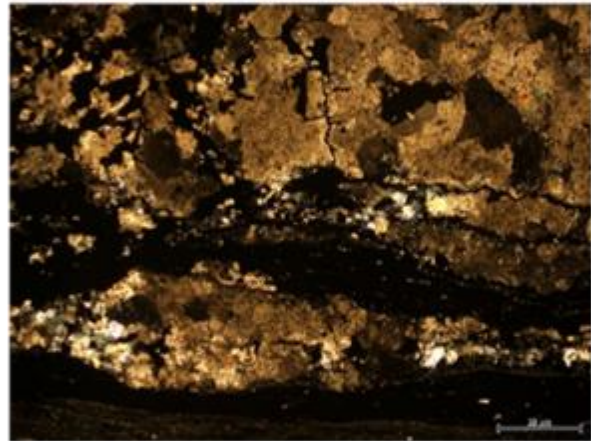


Figure 43. Showing the similar groundmass interbedded with calcite layers which looks to have been boudinaged.

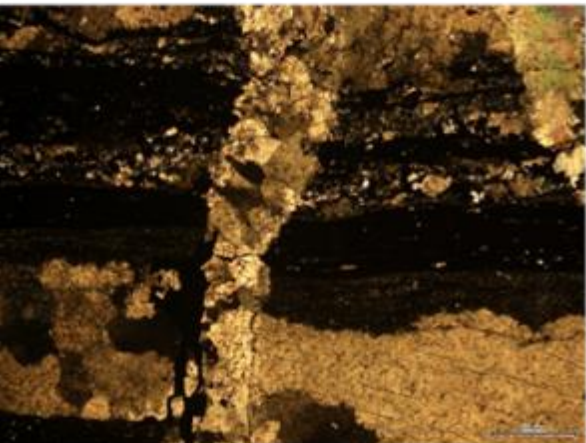


Figure 44. Fine grained dark groundmass between calcite horizontal layers and cross-cut by vertical calcite veins.

B218

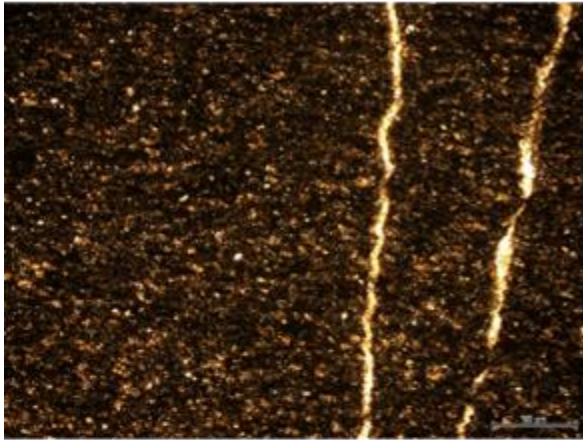


Figure 46. Fine grained groundmass at base of thin section, with relatively even distribution of light and dark minerals. Two calcite veins overprinting groundmass.

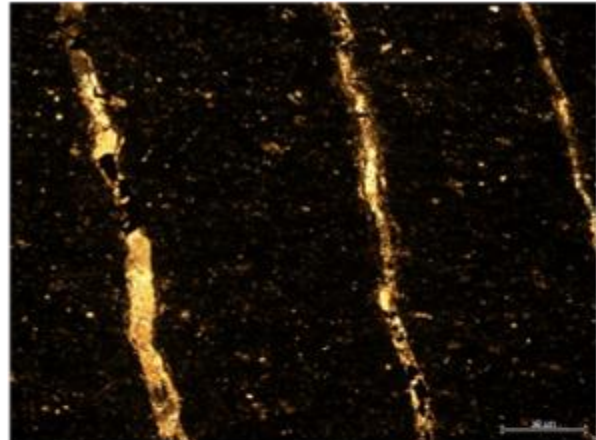


Figure 48. Calcite veins with pyrite inclusions.

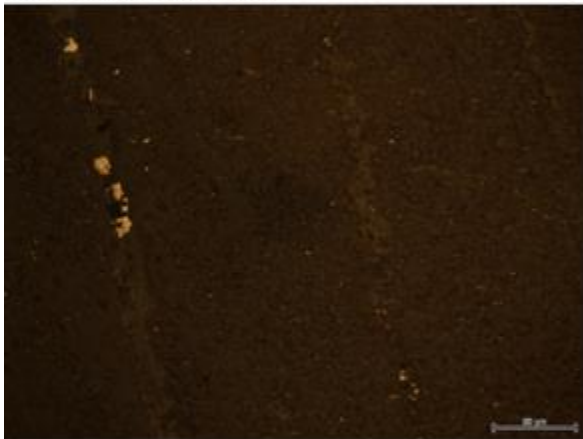


Figure 49. Pyrite within calcite vein, figure 47 in reflected light.

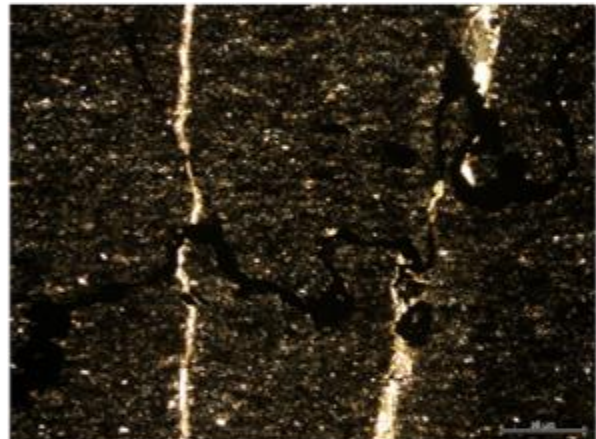


Figure 50. Opaque and non-reflective mineral over printing other calcite veins and infilling a vein (scale of vein not pictured). XPL.

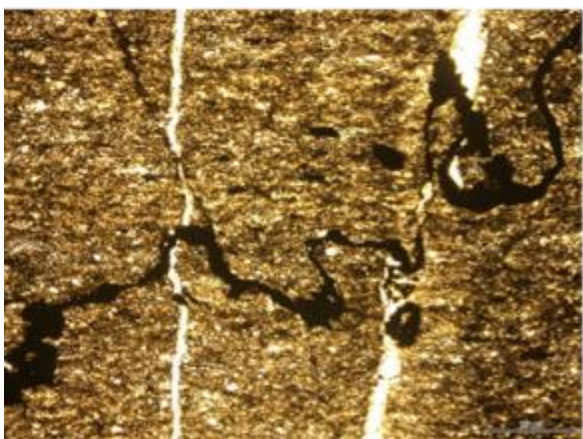


Figure 51. PPL image of figure 50.



Figure 52. Reflected light image of Figure 50 and 51, showing the black mineral is opaque and non-reflective, therefore not a sulphide.



Figure 53. Calcite vein, transitioned to opaque mineral vein infill (very thin vein). This is more obvious throughout the thin section, lower and higher of this image.

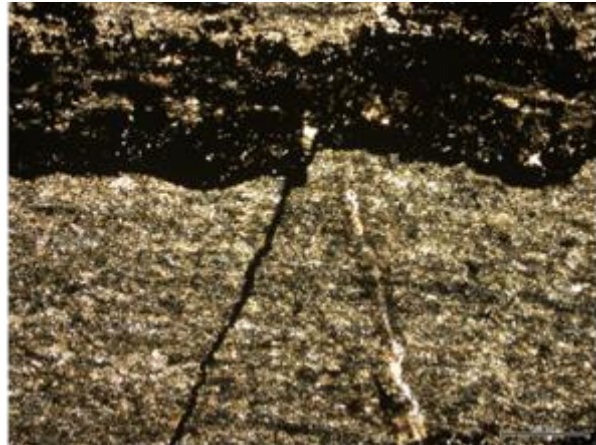


Figure 54. The same opaque vein in figure 53, further up the bed. The other dark layers is fine grained pyrite (not opaque) as seen in figure --

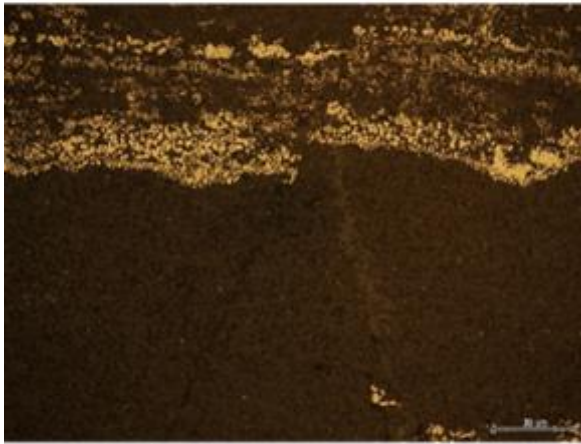


Figure 55. Reflective light image of fine grained pyrite as seen in figure 54. Can see the faint trace of the opaque vein and a calcite vein to the right.

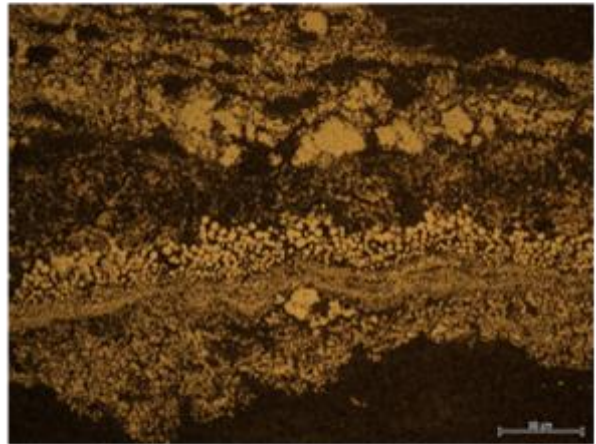


Figure 56. Pyrite in reflected light, appears throughout sample as bands that look more consolidated than what they do at higher magnification.

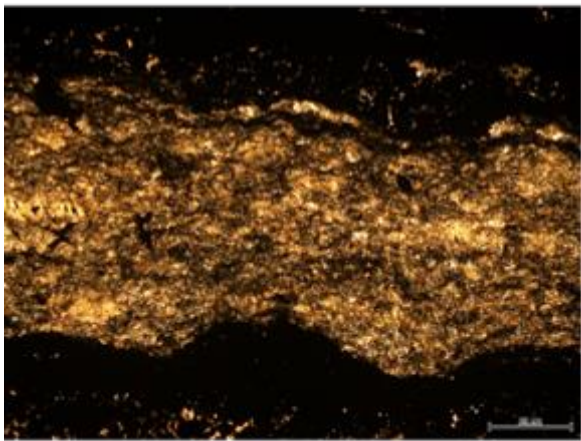


Figure 57. Bands of pyrite (black) separated by fine grained light ground mass with some inclusions of calcite.

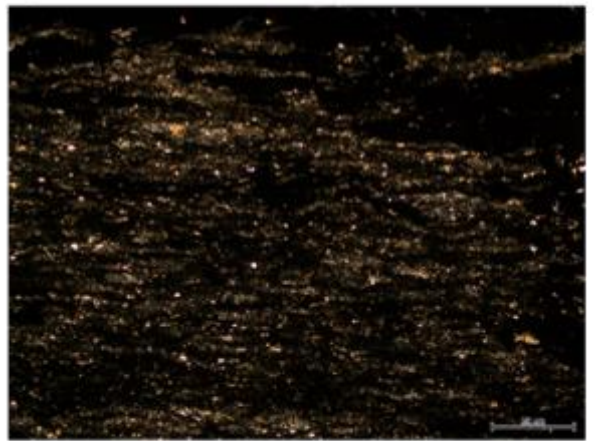


Figure 58. Groundmass at the top of the sample is much the same as the groundmass throughout the whole thin section, however, slightly coarser than the base of the sample (figure 46).